Rodrigo Galvão dos Santos

Rare-earth-doped yttria nanoparticles as temperature sensors for whispering-gallery-mode resonators

Recife

2022

Rodrigo Galvão dos Santos

Rare-earth-doped yttria nanoparticles as temperature sensors for whispering-gallery-mode resonators

Tese apresentada ao Programa de Pós-Graduação em Física da Universidade Federal de Pernambuco, como requisito parcial para a obtenção do título de Doutor em Física. Área de Concentração: Óptica.

Orientador: Leonardo de Souza Menezes

Recife

2022

Catalogação na fonte
Bibliotecária Luiza de Oliveira, CRB4-1316

S237r Santos, Rodrigo Galvão dos
Rare-eart-doped ytria nanoparticlesas temperatures sensors for whispering-gallery-mode resonators /Rodrigo Galvão dos Santos. – 2022.
98 f.: il., tab.

Orientador: Leonardo de Souza Menezes.
Tese (Doutorado) – Universidade Federal de Pernambuco. CCEN, Física, Recife, 2022.

Inclui referências. Inclui apêndice.

1. óxido de ítrio. 2. Íons terras-raras. 3. Nanotermometria. 4. modos de galeria de sussurro. I. Menezes, Leonardo de Souza (orientador). II. Título.

535.2 CDD (23. ed.) UFPE - CCEN 2022-142

RODRIGO GALVÃO DOS SANTOS

RARE-EARTH-DOPED YTTRIA NANOPARTICLES AS TEMPERATURE SENSORS FOR WHISPERING-GALLERY-MODE RESONATORS

Tese apresentada ao Programa de Pós-Graduação em Física da Universidade Federal de Pernambuco, como requisito parcial para a obtenção do título de Doutor em Física.

Aprovada em: 30/06/2022.

BANCA EXAMINADORA

_____
Prof. Leonardo de Souza Menezes
Orientador
Universidade Federal de Pernambuco

_____
Prof. Anderson Monteiro Amaral
Examinador Interno
Universidade Federal de Pernambuco

_____
Prof. Eduardo Padrón Hernández
Examinador Interno
Universidade Federal de Pernambuco

_____
Prof. Carlos Jacinto da Silva
Examinador Externo
Universidade Federal de Alagoas

_____
Prof. Renato Evangelista de Araújo
Examinador Externo
Universidade Federal de Pernambuco

ABSTRACT

In this thesis, Y_2O_3 (yttria) nanoparticles (NPs) doped with rare-earth ions, namely Nd^{3+} and Er^{3+},Yb^{3+} are investigated as temperature sensors for whispering-gallery-mode (WGM) resonators. The ions were chosen to match the available pump lasers for WGM coupling in a silica microsphere, so that multiple sensing parameters can be achieved with a single excitation wavelength. The silica microspheres and the NPs used for this thesis have diameters of about 100 µm and 150 nm respectively. The much smaller size of the NPs with respect to the microspheres ensures that the thermal equilibrium remains undisturbed in the medium of interest (*i. e.*, the microsphere) during the temperature measurements. In order to understand the effects of the lattice vibrations of host materials like yttria on the spectroscopic properties of the active ions, the concept of phonon by quantization of lattice vibration is introduced and the widths and positions of spectral lines of Nd^{3+} in Y_2O_3 are discussed as an example of the ion-phonon interactions following a Debye model. Moreover, the theoretical basis of WGMs coupling is derived from the modal equation for a microsphere and some simulations are performed for the system of interest. This system is then considered for temperature sensing applications and the effects of a near-field probe such as a nanoparticle close to the microsphere's surface are calculated using Rayleigh scattering. Some control experiments were also performed in order to optimize the experimental setup for WGM coupling using the microsphere-prism coupling geometry. A nanothermometer based on single Nd^{3+}:Y_2O_3 NPs which relies on the ratio of the intensities of the light emitted due to transitions coming from thermally coupled energy levels is presented, followed by another yttria based system, Er^{3+},Yb^{3+}:Y_2O_3. Both systems were characterized by exciting single nanoparticles with low power, continuous-wave lasers and the results were described by a rate equation model considering multiphonon interactions. The system presented a relative sensitivity up to 1.36% at 300 K and accuracy of 0.1 K, thus being suited for temperature sensing applications. Finally, some future experiments are proposed for the Nd^{3+}:Y_2O_3 system, which showed promising results for temperature sensing for microresonators, taking into consideration the theoretical and experimental aspects for both the WGM and luminescence spectroscopy.

Keywords: yttrium oxide, rare-earth ions, nanothermometry, whispering-gallery-modes.

RESUMO

Nesta tese, nanopartículas (NPs) de Y_2O_3 (ítria) dopadas com íons terra-rara, mais especificamente Nd^{3+} e Er^{3+},Yb^{3+} são analisadas como sensores de temperatura para ressonadores de modos de galeria de sussurro (MGS). Os íons foram escolhidos de maneira a coincidir com os comprimentos de onda disponíveis para acoplamento de MGS em uma microesfera de sílica, de modo que múltiplos parâmetros de sensibilidade pudessem ser obtidos com um mesmo comprimento de onda de excitação. As microesferas de sílica e as NPs usadas nesta tese têm diâmetros de cerca de 100 µm e 150 nm respectivamente. A dimensão muito menor das NPs quando comparadas às microesferas garante que o equilíbrio térmico não seja perturbado no meio de interesse (*i. e.*, as microesferas) durante as medidas de temperatura. Para entender os efeitos das vibrações na rede de materiais como a ítria nas propriedades espectroscópicas dos íons ativos, o conceito de fônon é introduzido por meio da quantização das vibrações da rede e as larguras e posições das linhas espectrais do Nd^{3+} em Y_2O_3 são discutidas como um exemplo das interações íon-fônon seguindo o modelo de Debye. Além disso, as bases teóricas do acoplamento de MGS são derivadas a partir da equação modal para uma microesfera e algumas simulações são realizadas para o sistema de interesse. Esse sistema é então considerado para aplicações de sensor de temperatura e os efeitos de uma ponteira de campo próximo como uma nanopartícula próxima à superfície da microesfera são calculados usando o espalhamento Rayleigh. Alguns experimentos de controle foram realizados para otimizar o aparato experimental para acoplamento de MGS usando a configuração de acoplamento microesfera-prisma. Um nanotermômetro baseado em NPs individuais de Nd^{3+}:Y_2O_3 fundamentado na razão de intensidades da luz emitida devido às transições que surgem de níveis de energia termicamente acoplados é apresentado, seguido por outro sistema baseado em ítria, Er^{3+},Yb^{3+}:Y_2O_3. Ambos os sistemas são caracterizados pela excitação de nanopartículas individuais com baixa potência e laser contínuo e os resultados foram descritos por um modelo de equações de taxa que considera as interações multifônon. O sistema apresentou uma sensitividade relativa máxima de 1.36% em 300 K e precisão de 0.1 K, sendo portanto adequado para aplicações como sensor de temperatura. Por fim, experimentos futuros são propostos para o sistema de Nd^{3+}:Y_2O_3, que apresentou resultados promissores como sensor de temperatura para micro ressonadores, considerando os aspectos teóricos e experimentais dos MGS e espectroscopia de luminescência.

Palavras-chave: óxido de ítrio, íons terras-raras, nanotermometria, modos de galeria de sussurro.

CONTENTS

1 INTRODUCTION

Saint Paul's Cathedral in London is a famous example of the so called whispering-gallery phenomenon. The gallery gained its name due to a feature in the architecture so that one can whisper on one side of the dome and be heard by someone on the opposite side. Moreover, if one speaks facing one direction along the wall, the sound will return from behind. According to Lord Rayleigh, the sonorous vibrations have a tendency to cling to a concave surface, thus being trapped along the circular path. A small obstacle, however, held close to the surface is enough to intercept most of the effect [1].

Analogously to the acoustical whispering-gallery phenomenon, light can also be confined in spherical and cylindrical geometries and propagate in the form of a Whispering-Gallery-Mode (WGM). The possibility of WGM microresonators to confine light in a small volume for a considerably long period of time, which is given by the quality factor of the resonances supported by such microresonators, significantly enhances light-matter interactions and thus allows for a greater power density within the mode volume of the WGM [2, 3]. During the last few years, numerous applications for WGMs have been reported, such as label-free detection of single virus and nanoparticles [4–6], 3D strain measurements [7] in vivo sensing with microlasers [8–11] and optical vacuum sensors [12].

WGMs microresonators can also be utilized for temperature sensing applications, due to its sensitive response to the surrounding media's temperature. In a WGM-based temperature sensor, the resonance frequency is affected by the refraction index and the cavity's size, which vary with the temperature due to the thermo-optical and expansion effects, respectively [13]. Thermal sensing has been demonstrated, for instance, using silica- and silicon-based devices [14–16]. On the other hand, materials with larger thermal expansion coefficients, such as silk, can outperform the silica devices in terms of sensitivity [17].

A common issue with WGM-based temperature sensor is the difficulty of generating an absolute temperature reading. In other words, the most common sensing mechanisms are based on relative temperature increments [18]. For that reason, the WGM can be paired with another mechanism for temperature sensing, such as the luminescence of nanoparticles (NPs). WGMs microresonators are often combined with trivalent rare-earth ions due to their numerous fluorescence emission bands from the ultraviolet to the mid infrared range of the spectrum [19], so that the luminescence properties of the active ions can also play a role in the temperature sensing techniques.

In this thesis, Y_2O_3 (yttria) NPs doped with rare-earth ions, namely Nd^{3+} and Er^{3+},Yb^{3+} are investigated as temperature sensors. The ions were chosen to match the available pump lasers for WGM coupling in a silica microsphere, so that multiple sensing parameters can be achieved

with a single excitation wavelength. To the best of our knowledge, this approach has not net been explored for single NPs.

Silica was used as the cavity material since it enables the manufacture of microspheres using the carbon dioxide laser melting technique, where a CO_2 laser is focused at on one end of a silica fiber tip which absorbs the energy and heats up to the melting point [20]. Under the the surface tension, the heated end of the fiber is melted into a microsphere resonator [21, 22]. By carefully controlling the laser power and fiber position, microspheres with different diameters can be produced. The silica microspheres and the NPs used for this thesis have diameters of about 100 µm and 150 nm respectively. The much smaller size of the NPs with respect to the microspheres ensures that the thermal equilibrium remains undisturbed in the medium of interest (*i. e.*,, the microsphere) during the temperature measurements [23]. However, it adds an additional complication for defining a local temperature at length scales smaller than one wavelength. It's thus important to address the question about whether the temperature can be meaningfully defined on nanometric length scales [24].

Local physical properties may have different behaviors depending on whether or not the local state is thermalized. Therefore, there may be a limit for the spatial resolution on which a temperature profile can be determined [25]. In a spherical particle, increasing its diameter, the volume grows faster than its surface and effective interactions between the interior and exterior regions, provided that they are short ranged, are less relevant [26, 27]. This scaling behavior ensures that the thermodynamic limit is valid, since the correlations between a given region and its surroundings becomes negligible in the large region size limit [28].

The scaling of interactions between the parts of a system compared to the local energy thus gives a minimal length scale above which the correlations are still small enough to generate a local temperature, which exists if the considered part of the system is in a canonical state. This minimum length scale is fundamental for applications such as intracellular nanothermometry, as demonstrated by the so-called "10^5 gap issue", which is still an open problem [29]. This issue arises from discrepancies between measured temperature increments and their corresponding theoretical calculations from experimental parameters. The calculated values can be orders of magnitude smaller than the values obtained from direct measurements. Reliable temperature variations over 1 K among cellular compartments were demonstrated in unstimulated cells using different luminescence thermometry techniques [30–36]. Moreover, temperature increments in the same order of magnitude were also detected using non-luminescent thermal probes [37–39]. The issue triggered a discussion among researchers in the field about the possibility of single cell raise its temperature by endogenous thermogenesis [40–44].

The "10^5 gap issue" suggests that the size limits for the existence of a local temperature should be carefully determined, otherwise any temperature increment detected at the nanoscale could be attributed to some artifact which arose from the non-equilibrium state. It was demonstrated that in most cases, the concept of temperature is valid even on a scale of 10 nm [29].

Additionally, the microscopic limit for local temperature was also calculated for yttria crystals considering an one dimensional harmonic chain model, which gave a theoretical value of 1.5 µm for minimum length required for the existence of local temperature. The details for this calculation can be found in the Appendix A.

From the nanothermometry measurements performed in this thesis, it was shown that the thermal equilibrium was reached for NPs with diameter of 110 nm. Therefore, the actual limit for local temperature should be in the range of 10 nm to 100 nm, and the 1.5 µm value can be understood as an overestimation given the limits of the simple harmonic chain model. That being said, the yttria NPs are thus potential candidates for noncontact thermal sensing for microresonators, since other methods such as thermocouples and thermistors are inappropriate at such scales, granted that the required thermal connection with the sample disturbs the measurements [45].

The core of this thesis is structured in five chapters, which are summarized as follows:

Chapter 2 presents some of the effects of the lattice vibrations of host materials on the spectroscopic properties of the active ions. The concept of phonon by quantization of lattice vibration is introduced and the widths and positions of spectral lines of Nd^{3+} in Y_2O_3 are discussed as an example of the ion-phonon interactions following a Debye model.

Chapter 3 gives the theoretical basis of WGMs coupling. The modal equation for a spherical microsphere is derived and some simulations are performed for our system of interest. This system is then considered for temperature sensing applications and the effects of bringing a near-field probe close to the microsphere's surface are calculated using Rayleigh scattering.

Chapter 4 describes the experimental setup for WGM spectroscopy. Several control experiments were performed in order to optimize the setup as well as to calibrate the instruments. The microsphere-prism coupling geometry was taken into consideration in order to position the focusing lens while the scanning frequency was monitored using a Fabry-Perot interferometer.

Chapter 5 shows a nanothermometer based on single Nd^{3+}:Y_2O_3 NPs. The nanothermometer relies on the ratio of thermally coupled Nd^{3+} emission lines accessible by either continuous-wave upconversion under 880 nm or downconversion under 532 nm excitation wavelengths. Both processes are modeled through rate equation systems based on multiphonon interactions between excited luminescent states.

Chapter 6 considers another yttria based nanothermometer, Er^{3+}, Yb^{3+}:Y_2O_3 NPs. The nanothermometer characterization was performed by exciting the single nanoparticles with a low power, continuous-wave laser emitting at 980 nm. The results were described by a rate equation analysis using a dual effective phonon model.

Chapter 7 brings conclusions and perspectives about the best suited candidate for temperature sensing for microresonators, taking into consideration the theoretical and experimental aspects for both the WGM and luminescence spectroscopy. To conclude this thesis, some future experiments are proposed for the Nd^{3+}:Y_2O_3 system.

2 PHONON EFFECTS IN RARE-EARTH DOPED CRYSTALS

This chapter presents some of the effects of the lattice vibrations of host materials on the spectroscopic properties of the active ions. Using the concept of phonon as a quantization of lattice vibrations, the widths and positions of spectral lines of Nd^{3+} in Y_2O_3 are discussed as an example of the ion-phonon interactions following a Debye model [46–49].

The starting point for studying lattice vibrations is to solve the Schrödinger's equation. For the hydrogen atom, the electron is about 1/1840th as heavy as the the nucleus. Therefore, from a classical point of view, the ionic movement is much slower than the electronic's. For that reason, the so-called *adiabatic approximation* can be applied, which consists on solving the problem of the lattice vibrations for an average electronic field [50]. It can be shown that the quantum mechanical treatment of vibrations in a crystal lattice yields quanta of elementary excitation called *phonons*, which can be treated as Bosons. Moreover, the Hamiltonian of such system is analogous to the one of a system of Harmonic Oscillators. The total energy in a certain state is thus given by:

$$E\left(n_1, n_2, n_3, \ldots n_{3Nr}\right) = \sum_{i=1}^{3Nr} \left(n_i + \frac{1}{2}\right) \hbar\omega_i, \tag{2.1}$$

where N is the number of unit cells, r the number of atoms in each cell, which account for $3Nr$ normal vibration modes and $\hbar$ is the reduced Planck constant.The harmonic oscillator is labeled by the index i with frequency ω_i and the summation is over all the $3Nr$ harmonic oscillators.

When there are two kinds of ions in each cell ($r = 2$), the lattice system has three acoustic and three optical modes [51]. In general, there are three acoustic modes and $3r$–3 optical modes. For the acoustic modes, the two kinds of ions vibrate in the same direction, while for the optical mode, the vibrations of the two ions with opposite charge are opposite. The optical modes are of particular interest since they will produce a net electric dipole moment and so can interact with electromagnetic fields.

The probability of finding the system in a state with energy E is proportional to the Boltzmann's factor in the thermal equilibrium. Therefore, The average phonon number of certain mode can be written as:

$$\bar{n}_i = \frac{\sum_{n_i} n_i \exp\left(-E_i/k_BT\right)}{\sum_{n_i} \exp\left(-E_i/k_BT\right)} = \frac{\sum_{n_i} n_i \exp\left(-n_i\hbar\omega_i/k_BT\right)}{\sum_{n_i} \exp\left(-\hbar\omega_i/k_BT\right)}, \tag{2.2}$$

where k_B is the Boltzmann constant. Since $E_i = \left(n_i + \frac{1}{2}\right)\hbar\omega_i$, the $\left[\exp\left(-\hbar\omega_i/2k_BT\right)\right]$ factor cancels out. The summation thus runs over the phonon number of a certain mode. Since:

$$\sum_{n_i} \exp\left(-n_i \hbar\omega_i / k_B T\right) = \frac{1}{\left[1 - \exp\left(-\hbar\omega_i / k_B T\right)\right]}, \tag{2.3}$$

and:

$$\begin{aligned}\sum_{n} n_i \exp\left(-\hbar\omega_i n_i / k_B T\right) &= \exp\left(-\hbar\omega_i / k_B T\right) \frac{d \sum_{n_i} \exp\left(-\hbar\omega_i n_i / k_B T\right)}{d\left[\exp\left(-\hbar\omega_i / k_B T\right)\right]} \\ &= \exp\left(-\hbar\omega_i / kT\right) \frac{d\left\{\frac{1}{\left[1-\exp(-\hbar\omega_i / k_B T)\right]}\right\}}{d\left[\exp\left(-\hbar\omega_i / k_B T\right)\right]} \\ &= \frac{\exp\left(-\hbar\omega_i / k_B T\right)}{\left[1 - \exp\left(-\hbar\omega_i / k_B T\right)\right]^2},\end{aligned} \tag{2.4}$$

one gets:

$$\bar{n}_i = \frac{1}{\exp\left(\hbar\omega_i / k_B T\right) - 1}, \tag{2.5}$$

which is often used to discuss the spectroscopic problem related to lattice vibrations, particularly for multiphonon processes.

Some phonon effects on the fluorescence lines of Nd^{3+} ions in yttria can then be considered [52, 53]. For the sake of simplicity, only the spectral lines corresponding to the transitions from R_1 of the $^4F_{3/2}$ energy level to Z_3 of $^4I_{9/2}$ will be treated, as shown in Figure 1. That transition translates to a peak around 915 nm. Yttria was chosen as an example since it's the host matrix for the doped nanoparticles (NPs) which were used in the experiments for this thesis. The $R_1 \rightarrow Z_3$ was chosen among the available transitions because it is a well resolved peak of the $^4F_{3/2} \rightarrow {}^4I_{9/2}$ transition for the yttria matrix as will be seen in Chapter 5.

The total broadening of fluorescence lines can be written as [52]:

$$\Delta E_i = \Delta E_i^{\text{strain}} + \Delta E_i^{\text{M}} + \Delta E_i^{\text{D}} + \Delta E_i^{\text{R}}, \tag{2.6}$$

where $\Delta E_i^{\text{strain}}$ is the broadening introduced by the crystal strain inhomogeneity, ΔE_i^{M} is due to multiphonon emission processes, ΔE_i^{D} is due to direct one-phonon processes between the ith energy level and other levels nearby. Finally, ΔE_i^{R} is the broadening introduced by phonon Raman scattering. The one-phonon emission and absorption processes can be written explicitly in ΔE_i^{D} as:

$$\Delta E_i^{\text{D}} = \sum_{j<i} \bar{\beta}_{ij} \left(\frac{1}{e^{\Delta E_{ij/k} T} - 1} + 1 \right) + \sum_{j>i} \bar{\beta}_{ij} \frac{1}{e^{\Delta E_{ji}/kT} - 1} \tag{2.7}$$

and for ΔE_i^{R}:

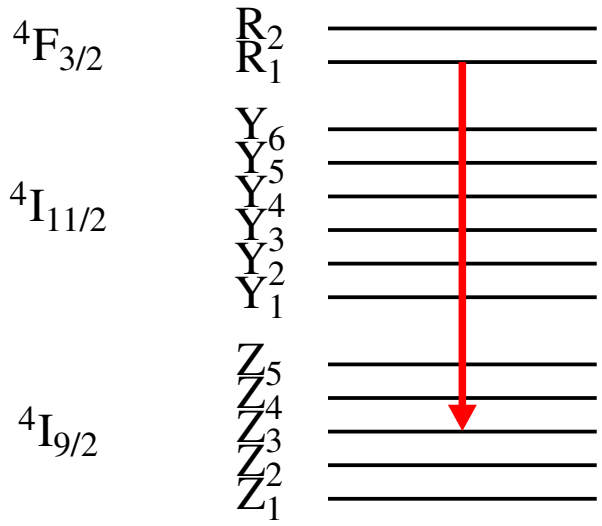

Figure 1 – Energy levels of Nd^{3+} in Y_2O_3: Nd^{3+}. R_i, Y_i and Z_i are Stark sublevels of the $^4F_{3/2}$, $^4I_{11/2}$ and $^4I_{9/2}$ transitions respectively [53]. The red arrow indicates the $R_1 \rightarrow Z_3$ transition which generates an emission peak around around 915 nm.

$$\Delta E_i^{\mathrm{R}} = \overline{\alpha_i} \left(\frac{T}{T_{\mathrm{D}}} \right)^7 \int_0^{T_{\mathrm{D}}/T} \frac{x^6 \mathrm{e}^x}{(\mathrm{e}^x - 1)^2} \, \mathrm{d}x, \tag{2.8}$$

where $\overline{\alpha_i}$ and $\bar{\beta}_{ij}$ are the coupling coefficients for the ion-phonon interaction. T_D is the effective Debye temperature of the phonon distribution . While $\Delta E_i^{\mathrm{strain}}$ gives rise to an inhomogeneous broadening and thus produces a Gaussian line shape, the broadenings due to ΔE_i^{M}, ΔE_i^{D} and ΔE_i^{R} are homogeneous and give Lorentzian line shapes.

A shape composed of a homogeneous part and inhomogeneous contributions can be represented by a Voigt profile so that the width can be resolved into each contributions using Posener tables [54]. It's useful to rewrite ΔE_i^{D} as a sum of a temperature independent and a temperature dependent term as:

$$\Delta E_i^{\mathrm{D}} = \sum_{j<i} \bar{\beta}_{ij} + \Delta E_i^{\mathrm{DT}}, \tag{2.9}$$

where:

$$\Delta E_i^{\mathrm{DT}} \equiv \sum_{j<i} \bar{\beta}_{ij} \frac{1}{\mathrm{e}^{\Delta E_{ij}/kT} - 1} + \sum_{j>i} \bar{\beta}_{ij} \frac{1}{\mathrm{e}^{\Delta E_{ji}/kT} - 1}. \tag{2.10}$$

For rare earth ions, the energy separation among Stark levels can reach up to 100 cm^{-1}, thus $\sum_{j<i} \bar{\beta}_{ij}$ can produce an observable broadening even at low temperatures [47]. Equation 2.6 can thus be written as:

$$\Delta E_i = \Delta E_i^{\mathrm{strain}} + \Delta E_i^{\mathrm{M}} + \sum_{j<i} \bar{\beta}_{ij} + \Delta E_i^{\mathrm{DT}} + \Delta E_i^{\mathrm{R}} \tag{2.11}$$

When T=0 K, one gets:

$$\Delta E_i = \Delta E_i^{\text{strain}} + \Delta E_i^{\text{M}} + \sum_{j<i} \bar{\beta}_{ij} \equiv \Delta E_{i0}, \tag{2.12}$$

where ΔE_{i0} is called the *residual width* of the *i*th level. For yttria, the Raman scattering dominates the temperature dependent processes [53]. Therefore, for the $R_1 \rightarrow Z_3$ emission line, the spectral line thermal broadening can be expressed as [53]:

$$\Delta E = \Delta E_0 + \bar{\alpha} \left(\frac{T}{T_{\text{D}}} \right)^7 \int_0^{T_{\text{D}}/T} \frac{x^6 \text{e}^x}{(\text{e}^x - 1)^2} \, \text{d}x. \tag{2.13}$$

Apart from the spectral line broadening the electron–phonon interaction also plays an important role as a major mechanism for the thermal shifting of the spectral lines. Using perturbation theory, the shift can be written as [52]:

$$\delta E_i = \delta E_i^{\text{R}} + \delta E_i^{\text{D}} \tag{2.14}$$

where:

$$\begin{aligned} \delta E_i^{\text{R}} &= \alpha_i \left(\frac{T}{T_{\text{D}}} \right)^4 \int_0^{T_{\text{D}}/\text{T}} \frac{x^3}{\text{e}^x - 1} \, \text{d}x \\ \delta E_i^{\text{D}} &= \sum_{j \neq i} T_{ij} \beta_{ij} \left(\frac{T}{T_{ij}} \right)^2 \mathbf{P} \int_0^{T_{\mathbf{D}}/T} \frac{x^3}{\text{e}^x - 1} \frac{\text{d}x}{\left(T_{ij}/T^2 \right) - x^2} \end{aligned} \tag{2.15}$$

and α_i and β_{ij} are the coupling coefficients, $T_{ij} = \left(E_i - E_j \right) / k$ is in the range of $\pm \hbar \omega_{\mathbf{D}}$ and $\mathbf{P}$ is the principal value of the integral [49]. It's worth noticing that δE_i^{R} has the same expression as the energy of a phonon gas, which can be derived from Equation 2.5:

$$E(T) = 9NkT \left(\frac{T}{T_D} \right)^3 \int_0^{T_D/T} \frac{x^3}{e^x - 1} dx \tag{2.16}$$

The δE_i^{D} term was found to be negligible when compared to the δE_i^{R} for determining the spectral shift [55–57]. Therefore, the thermal shift of the line position is given by:

$$\delta E \approx \delta E^{\text{R}} = \alpha \left(\frac{T}{T_{\text{D}}} \right)^4 \int_0^{T_{\text{D}}/T} \frac{x^3}{\text{e}^x - 1} \, \text{d}x \tag{2.17}$$

where α and T_{D} are adjustable parameters, which are shown in Table 1 for the $R_1 \rightarrow Z_3$ emission line for bulk yttria. The magnitude of the shift becomes greater the smaller is the particle's dimension, which could be attributed to the increasingly role played by the surface ions [53].

Figure 2 shows the theoretical curves for Equations 2.13 and 2.17, considering the parameters of Table 1. The line positions are thus red shifted with increasing temperature. This technique allows for an indirect measurement of Debye's temperature, which for the yttria crystal

Parameter	Value
α	22 cm^{-1}
$\bar{\alpha}$	95 cm^{-1}
T_D	440 K for Equation 2.13 and 429 K for Equation 2.17
ΔE_0	2.46 cm^{-1}

Table 1 – Fitting parameters for the linewidth (Equation 2.13) and lineshift (Equation 2.17) for the $R_1 \rightarrow Z_3$ emission line [53].

is expected to be around 435 K and should be close to the value obtained by heat capacity measurements. Figure 2 also shows that δE around 300 K presents a nearly linear behavior with the temperature, which by itself could be used as thermometric parameter [58]. It's worth commenting that for a range of 150 K to 700 K, a lineshift of only 8 cm^{-1} is found. That can limit the applicability of this technique for sensing temperature increments of tens of Kelvin above room temperature, which would be barely detectable by most spectrometers.

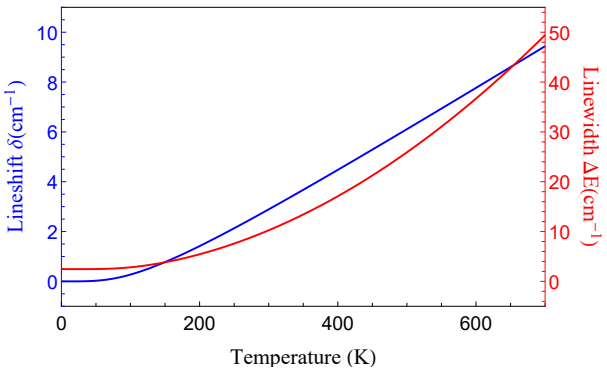

Figure 2 – Theoretical results of thermal broadening and shifting of emission spectral lines for the $R_1 \rightarrow Z_3$ emission line.

The thermal line broadening and shifting have the same orders of magnitude for the same rare earth ion in different host matrices or for different rare earth ions in the same material [55–57]. On the other hand, different values for T_D can be found for the broadening and shifting due to the contribution of single phonon absorption and emission not being taken into account, as was the case for yttria. Moreover, the broadenings and shiftings are different for different pairs of Stark sublevels in the same ion [59, 60].

In conclusion, the lattice vibrations are capable of introducing thermal effects in the observable emission spectrum. On the other hand, as will be shown in the following chapters, phonons can also generate thermal effects which are more sensitive to smaller temperature increments if, for instance, they have enough energy to allow for phonon-assisted luminescence processes. Moving forward with the theoretical background for this thesis, Chapter 3 presents the fundamentals of Whispering-Gallery-Modes in silica microspheres, which also possess promising thermal sensing capabilities.

3 WGMs IN SPHERICAL OPTICAL MICRORESONATORS

In this chapter, the theoretical basis of WGMs and the coupling of light to them are presented following the method developed by Balac [61]. The modal equation for a perfect microsphere is derived and some simulations are performed for our system of interest. This system is then considered for temperature sensing applications and the effects of bringing a near-field probe close to the microsphere's surface are calculated using Rayleigh scattering theory.

3.1 Expression of WGM in a spherical microresonator

The harmonic solutions for Maxwell's equations for a spherical dielectric cavity can be written as:

$$\mathbf{E}(\mathbf{r},t) = \mathrm{Re}[\underline{\mathbf{E}}(\mathbf{r})\exp(\mathrm{i}\omega t)], \quad \mathbf{B}(\mathbf{r},t) = \mathrm{Re}[\underline{\mathbf{B}}(\mathbf{r})\exp(\mathrm{i}\omega t)] \tag{3.1}$$

where $\mathbf{E}$ and $\mathbf{B}$ are respectively the electric field and magnetic induction of the mode and ω is the resonance frequency. The underlying bars in $\underline{\mathbf{E}}(\mathbf{r})$ and $\underline{\mathbf{B}}(\mathbf{r})$ represent the complex valued amplitudes. Following Hansen's method [62], it is found that there are two kinds of electromagnetic fields with different polarizations: TE (transverse electric) and TM (transverse magnetic) defined in spherical coordinates. For TE modes the electric field is parallel to the microsphere's surface while for TM modes, the magnetic induction is parallel to the microsphere's surface. For TE modes, the mode field is given by:

$$\underline{\mathbf{E}}(r,\theta,\varphi) = \begin{cases} \dfrac{\psi_\ell(kr)}{kr}\mathbf{X}_{\ell m}(\theta,\varphi) & \text{if } r \le R \\ \dfrac{k_0}{k}\dfrac{\psi_\ell(kR)}{\zeta_\ell(k_0R)}\dfrac{\zeta_\ell(k_0r)}{k_0r}\mathbf{X}_{\ell m}(\theta,\varphi) & \text{if } r > R \end{cases} \tag{3.2}$$

and:

$$\underline{\mathbf{B}}(r,\theta,\varphi) = \begin{cases} \dfrac{\mathrm{i}k}{\omega}\left(\ell(\ell+1)\dfrac{\psi_\ell(kr)}{k^2r^2}\mathbf{Z}_{\ell m}(\theta,\varphi) + \dfrac{\psi'_\ell(kr)}{kr}\mathbf{Y}_{\ell m}(\theta,\varphi)\right) & \text{if } r \le R \\ \dfrac{\mathrm{i}k_0^2}{k\omega}\dfrac{\psi_\ell(kR)}{\zeta_\ell(k_0R)}\left(\ell(\ell+1)\dfrac{\zeta_\ell(k_0r)}{k_0^2r^2}\mathbf{Z}_{\ell m}(\theta,\varphi) + \dfrac{\zeta'_\ell(k_0r)}{k_0r}\mathbf{Y}_{\ell m}(\theta,\varphi)\right) & \text{if } r > R \end{cases} \tag{3.3}$$

where $k_0 = \omega/c$ and $k = k_0N$. N the optical index of the dielectric cavity and R its radius. Moreover, ℓ,m are integers such that $-\ell \le m \le \ell, \ell \in \mathbb{N}$, $\mathbf{X}_{\ell m}$, $\mathbf{Y}_{\ell m}$ and $\mathbf{Z}_{\ell m}$ are the Vector Spherical Harmonics defined from the Scalar Spherical Harmonics Y_ℓ^m as:

$$\mathbf{Z}_{\ell m} = Y_\ell^m\mathbf{e}_\mathbf{r}, \quad \mathbf{Y}_{\ell m} = r\nabla Y_\ell^m, \quad \mathbf{X}_{\ell m} = \nabla Y_\ell^m \wedge \mathbf{r} \tag{3.4}$$

where $\mathbf{e_r}$ is the radial unit vector and ψ_ℓ and ζ_ℓ are respectively the Riccati-Bessel functions of first and third kinds. They are related to the Bessel and Hankel function as [63, 64]:

$$\psi_\ell(x) = \sqrt{\frac{\pi x}{2}} J_{\ell+\frac{1}{2}}(x), \quad \zeta_\ell(x) = \sqrt{\frac{\pi x}{2}} H^{(2)}_{\ell+\frac{1}{2}}(x) \tag{3.5}$$

The Spherical Surface Harmonics of degree ℓ and order m are defined as [65]:

$$Y^m_\ell(\theta, \varphi) = C_{\ell m} P^m_\ell(\cos(\theta)) \mathrm{e}^{\mathrm{i}m\varphi} \tag{3.6}$$

and the normalization constant $C_{\ell m}$ is given by:

$$C_{\ell m} = \sqrt{\frac{(2\ell+1)}{4\pi} \frac{(\ell-m)!}{(\ell+m)!}} \tag{3.7}$$

For TM modes, one gets:

$$\underline{\mathbf{E}}(r, \theta, \varphi) = \begin{cases} \ell(\ell+1) \frac{\psi_\ell(kr)}{k^2 r^2} \mathbf{Z}_{\ell m}(\theta, \varphi) + \frac{\psi'_\ell(kr)}{kr} \mathbf{Y}_{\ell m}(\theta, \varphi) & \text{if } r < R \\ \frac{\psi_\ell(kR)}{\zeta_\ell(k_0 R)} \left(\ell(\ell+1) \frac{\zeta_\ell(k_0 r)}{k_0^2 r^2} \mathbf{Z}_{\ell m}(\theta, \varphi) \right. & \\ \qquad \left. + \frac{\zeta'_\ell(k_0 r)}{k_0 r} \mathbf{Y}_{\ell m}(\theta, \varphi) \right) & \text{if } r > R \end{cases} \tag{3.8}$$

and:

$$\underline{\mathbf{B}}(r, \theta, \varphi) = \begin{cases} \frac{\mathrm{i}k}{\omega} \frac{\psi_\ell(kr)}{kr} \mathbf{X}_{\ell m}(\theta, \varphi) & \text{if } r \leq R \\ \frac{\mathrm{i}k_0}{\omega} \frac{\psi_\ell(kR)}{\zeta_\ell(k_0 R)} \frac{\zeta_\ell(k_0 r)}{k_0 r} \mathbf{X}_{\ell m}(\theta, \varphi) & \text{if } r > R \end{cases} \tag{3.9}$$

The mode fields on both sides of the microsphere's surface follow the boundary conditions:

$$\begin{aligned} \left[\underline{\mathbf{E}}(r, \theta, \varphi) \wedge \mathbf{e_r}\right] &= \mathbf{0}, \\ \left[\underline{\mathbf{B}}(r, \theta, \varphi) \cdot \mathbf{e_r}\right] &= 0, \\ \left[\varepsilon \underline{\mathbf{E}}(r, \theta, \varphi) \cdot \mathbf{e_r}\right] &= 0, \\ \left[\underline{\mathbf{B}}(r, \theta, \varphi) \wedge \mathbf{e_r}\right] &= \mathbf{0}. \end{aligned} \tag{3.10}$$

The resonance frequencies ω are then found by solving the so-called modal equation [66, 67]:

$$P \frac{\psi'_\ell(kR)}{\psi_\ell(kR)} = \frac{\zeta'_\ell(k_0 R)}{\zeta_\ell(k_0 R)} \tag{3.11}$$

where $P = N$ for TE modes and $P = 1/N$ for TM modes. Therefore, a mode is defined in terms of three integers: ℓ involved in the modal Equation 3.11, n used to label the modal equation's solutions for a given ℓ value and m involved in the expression of the mode field. The P constant accounts for the different solutions for each polarization mode.

As a result from this analysis, there is a mode degeneracy since there are $(2\ell+1)$ modes with the same values of ℓ and n, and therefore with the same resonance frequency. On the

other hand, they differ with respect to the m value and thus have different expressions for the electromagnetic field. The index m is called the azimuthal mode number and can take $(2\ell + 1)$ values from $-\ell$ to ℓ. Negative values of m have the physical meaning of counter-propagating modes. Furthermore, the polar mode number ℓ is the number of wavelengths that can fit around the sphere, while the radial mode number n is equal to the number of maxima of intensities in the radial direction and $(\ell - |m| + 1)$ is the number of maxima of intensities in the polar direction.

Geometric optics can be used to illustrate the concept of WGM in a simple way [68]. Considering a sphere with radius R and refractive index N, a ray of light with wavelength λ can propagate inside, hitting the surface above the critical angle, so light is totally reflected. Because of the spherical symmetry, all subsequent reflections occur at the same angle x_i, so light gets trapped as shown in Figure 3.

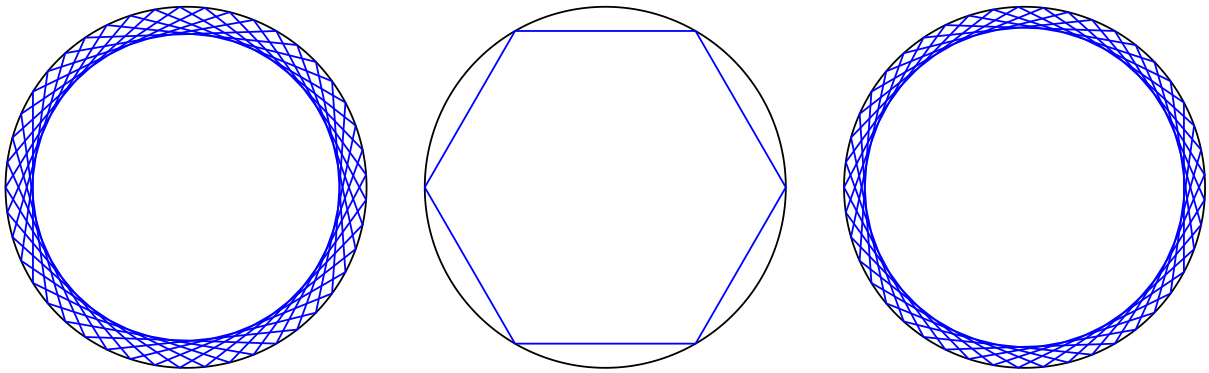

(a) $x_i = 58°$ (b) $x_i = 60°$ (c) $x_i = 62°$

Figure 3 – Light ray trajectories along a sphere great circle. a) 45 reflections and 8 round trips. b) Light ray is trapped self consistently after 6 reflections. c) 45 reflections and 7 round trips.

For each reflection, the beam moves along the arc the distance of $\pi - 2x_i$, assuming a sphere with unit radius. For $x_i = 58°$ and $x_i = 62°$ light returns to the starting point after 45 reflections. However, the former case has one round trip more than the latter. For large values of x_i, close to 90°, the number of reflections grows to 180 for only one round trip, as shown in Figure 4. The reason for the large number of reflections for $x_i = 83°$ is that every reflection at that angle will move the ray 14° along the arc, so that the least common multiplier of 14 and 360 degrees is 2520 thus generating 180 reflections and 7 round trips.

Billiards correspond to the classical (short wavelength) limit of wave equations for light in a homogeneous cavity, so that the classical dynamics is analogous to the geometrical optics approximation [69]. As discussed previously, for large spheres ($\lambda \ll R$), the ray propagates close to the sphere's surface. The resonance condition is fulfilled if a round trip equals an integer number ℓ of wavelengths leading to constructive interference. In other words, the phase needs to match after one round trip. For these modes, known as the WGMs, light is strongly confined close to the sphere's surface. A resonance condition can thus be written as:

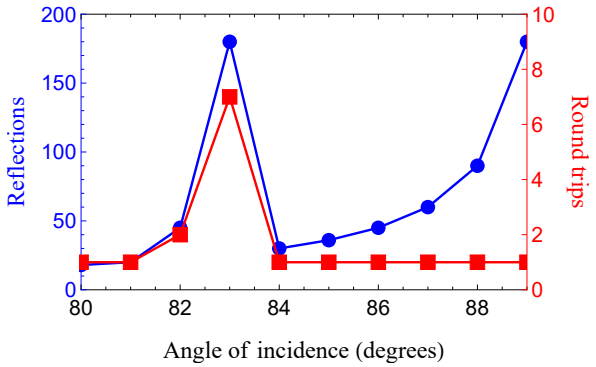

Figure 4 – Number of reflections (circles) and round trips (squares) as a function of the angle of incidence x_i.

$$\ell \approx \frac{2\pi RN}{\lambda}, \tag{3.12}$$

where ℓ (the polar mode number) is the number of wavelengths fitting along the spheres' circumference.

The goal for efficient WGM coupling is keeping $n = 1$, which corresponds to the best confined modes in the radial direction and $m = \ell$, which gives the best confinement in the polar direction. The mode satisfying those conditions and corresponding to the highest value of ℓ for which Equation 3.11 has a solution, is known as the fundamental mode. It is worth noticing that the ω solutions for Equation 3.11 are complex-valued. It is usual in the study of WGM in optical micro-resonators to introduce a radiative quality factor as:

$$Q = \frac{\mathrm{Re}(\omega)}{\mathrm{Im}(\omega)} \tag{3.13}$$

The smaller the radiation losses are, the smaller $\mathrm{Im}(\omega)$ is and therefore the higher is the radiative quality factor. Since the experimentally measured quality factor (Q-factor) of a microresonator also takes into account other losses, it is likely to happen that its value differs from the radiative quality factor. One of those losses mechanisms is the surface scattering, which will be the topic of the next sections of this chapter.

In most practical cases, the value of ℓ is often in the hundreds for the visible part of the spectrum, which correspond to a small radiative leakage outside the sphere. As a result, one can approximate the analytical solutions considering asymptotic expansions of Bessel's functions for large order ℓ, so that $\zeta_\ell(z) \approx \mathrm{i}\chi_\ell(z)$, where $\chi_\ell(z)$ denotes the Riccati-Bessel function of the second kind with order ℓ related to the Bessel function by:

$$\chi_\ell(x) = -\sqrt{\frac{\pi x}{2}} Y_{\ell+\frac{1}{2}}(x) \tag{3.14}$$

from this approximation, Equation 3.11 can be rewritten as:

$$P\frac{\psi'_\ell(kR)}{\psi_\ell(kR)} = \frac{\chi'_\ell(k_0R)}{\chi_\ell(k_0R)} \tag{3.15}$$

again $P = N$ for TE modes and $P = 1/N$ for TM modes. Equation 3.15 thus admits a real k_0 solution. For the main purposes of this thesis, we are interested into finding the positions of the WGM for a given pump wavelength. For numerical purposes it is more convenient to express Equation 3.15 in terms of Bessel functions of first and second kinds:

$$\frac{Y_{\ell-\frac{1}{2}}(k_0R)}{Y_{\ell+\frac{1}{2}}(k_0R)} - P\frac{J_{\ell-\frac{1}{2}}(kR)}{J_{\ell+\frac{1}{2}}(kR)} = \ell\left(\frac{1}{k_0R} - \frac{P}{kR}\right) \tag{3.16}$$

For a given mode number ℓ, the wavelengths λ for which resonance occurs are obtained by looking for the zeros of the modal function. For a given λ, the mode numbers ℓ corresponding to solutions to the modal equation are bound to:

$$\frac{2\pi\,(R+\delta_P)}{\lambda} < \ell + \frac{1}{2} < N\frac{2\pi\,(R+\delta_P)}{\lambda} \tag{3.17}$$

where $\delta_P \approx \frac{\lambda}{2\pi N}\frac{P}{\sqrt{N^2-1}}$. There is no solution ℓ to the modal equation greater than the upper bound value in Equation 3.17. Alternatively, there are some solutions lower than the lower bound value, but they do not correspond to WGM. In other words, for a fixed value of ℓ the resonance wavelengths λ are bound to:

$$\frac{2\pi R}{\ell + \frac{1}{2} - \alpha} < \lambda < \frac{2\pi RN}{\ell + \frac{1}{2} - \alpha N} \tag{3.18}$$

where $\alpha = P/\left(N\sqrt{N^2-1}\right)$. With the aid of the Matlab toolbox WGMode developed by Balac [61], WGM were determined for a silica microsphere of radius 50 µm excited with a laser source of 685 nm. At room temperature, the refractive index for fused silica (material with which the microspheres used in this work are made) within the range of 0.21 µm to 3.71 µm can be determined from [70]:

$$N^2 - 1 = \frac{0.6961663\lambda^2}{\lambda^2 - (0.0684043)^2} + \frac{0.4079426\lambda^2}{\lambda^2 - (0.1162414)^2} + \frac{0.8974794\lambda^2}{\lambda^2 - (9.896161)^2} \tag{3.19}$$

Thus, for 685 nm, the refractive index is 1.4556. From those considerations, one can calculate the WGM spectrum of such microsphere for a range of frequencies around that wavelength. Figure 5 shows the results given by the modal equation for the aforementioned parameters. A microsphere of diameter 100 µm was considered since its larger size allows for a denser WGM spectrum. Considering a range of 1 THz, which is typical for such microsphere size, the modes were calculated up to the third order of n for both the TE and the TM modes. The frequency difference between a mode ℓ and its neighboring mode $\ell + 1$ is the Free Spectral Range (FSR) of

the microresonator. A FSR of 662 GHz was verified for separation between successive TE or TM modes.

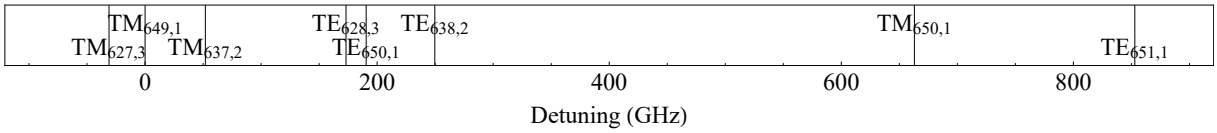

Figure 5 – WGM spectrum for a microsphere with diameter of 100 µm pumped with a tunable laser source of central wavelength 685 nm. The x-axis is the detuning frequency with respect to the $TM_{649,1}$ mode. The $TM/TE_{\ell,n}$ modes are shown up to $n = 3$.

As shown in Figure 5, the TM modes lead the TE counterparts in terms of frequency. For instance, the $TM_{650,1}$ is located 472 GHz ahead of the mode $TE_{650,1}$. On the other hand, the $TE_{651,1}$ is 190 GHz ahead of the mode $TM_{650,1}$. That can be understood as a result of the total internal reflection, which leads to a frequency shift between the TE and TM spectra, since the TE and TM modes experience different phase shifts along one round trip [71].

The knowledge of the relative positions between the TE and TM modes is helpful to define not only the FSR but also for better tuning the pump laser. As will be discussed in Chapter 4, the tunable diode laser can scan for only tens of GHz around a set wavelength, so if a fundamental mode lies outside that range, the set wavelength needs to be adjusted so that the mode can be excited. Moreover, the TE/TM modes can be selectively pumped using a half-wave plate to rotate the incident beam's polarization.

A common approximation for the FSR in WGM is given by [68]:

$$FSR \approx \frac{c}{2\pi RN} \tag{3.20}$$

which gives 656 GHz for the previous example, about 1% smaller than the result given from the modal equation. This small difference can be attributed to the approximations considered for the modal equation.

Since a perfect sphere is assumed, the modal equation cannot be used to calculate the positions of modes differing in m. The problem of determining the position of modes differing in m is shown in [72] by means of precessing modes in a slightly deformed microsphere. An arbitrary spherical function can be modeled by the precession of an inclined fundamental mode. The frequency shift can thus be interpreted as a change in the perimeter of the inclined ellipse of eccentricity ϵ. A first order approximation gives:

$$\frac{\Delta\omega}{\omega} = \pm\frac{\epsilon^2\left(\ell^2 - m^2\right)}{4\ell^2} \tag{3.21}$$

where $\Delta\omega$ is the frequency shift of a mode with certain m to the fundamental mode of the same family (same n and ℓ). The lift in degeneracy can lead to a red or blueshift depending on the shape of the microsphere. The positive sign in Equation 3.21 applies for oblate spheroid, while the negative sign is for a prolate one.

The knowledge of the electric field distribution of a mode allows one to calculate its volume. Due to the cumbersome form of the vector spherical harmonics, one approximation can be used [73, 74]:

$$V_{\text{mode}} \approx \frac{\left(\int \mathbf{E}(\mathbf{r},t)^2 d^3r\right)^2}{\int \mathbf{E}(\mathbf{r},t)^2 \mathbf{E}(\mathbf{r},t)^2 d^3r} \approx 3.4\pi^{3/2}(\lambda/2\pi N)^3 \ell^{11/6}\sqrt{\ell - m + 1} \tag{3.22}$$

which is valid for modes with $n = 1$. As an example, for λ=685 nm, N=1.4556 and $\ell = m = 650$, the resulting mode volume is 1142 μm^3 for a sphere with diameter 100 µm while its total volume is 523 599 μm^3. Therefore, the mode volume occupies about 0.2% of the sphere's total volume, thus once the ideal conditions for light coupling are met, the mode is well confined within the sphere and concentrates around its equator. Another way to quantify the mode coupling efficiency is from the resonator's Quality factor, which is the topic of the next section.

3.2 Quality factor of a resonance

One of the most important characteristics of a silica microsphere resonator is the extremely high quality factor (Q-factor) presented by the WGM it supports. The Q-factor of a resonance measures its losses and is defined as 2π times the stored energy divided by the energy losses per cycle. The Q-factor can thus be written as:

$$Q = \omega_0 \frac{\text{Stored energy}}{\text{Power loss}} \tag{3.23}$$

where ω_0 is the resonance frequency. It is possible to obtain a differential equation for the stored energy [68]:

$$\frac{dU}{dt} = -\frac{\omega_0}{Q}U \tag{3.24}$$

with solution given by $U(t) = U_0 e^{-\omega_0 t/Q}$. Therefore, the initial energy U_0 decays exponentially with decay factor $1/Q$. The oscillations in the field inside the cavity can be written as:

$$E(t) = E_0 e^{-\omega_0 t/2Q} e^{-i(\omega_0 + \Delta\omega)t} \tag{3.25}$$

where $\Delta\omega$ is a positive shift of the resonance frequency. A damped oscillation consists of a superposition of frequencies around $\omega = \omega_0 + \Delta\omega$. Thus:

$$E(t) = \frac{1}{2\pi}\int_0^\infty E(\omega) e^{-i\omega t} d\omega \tag{3.26}$$

where:

$$E(\omega) = \frac{1}{2\pi}\int_{-\infty}^{\infty} E_0 e^{-\omega_0 t/2Q} e^{i(\omega-\omega_0-\Delta\omega)t} dt \tag{3.27}$$

Evaluating Equation 3.27 gives an expression for the frequency distribution of the energy in the cavity:

$$|E(\omega)|^2 \propto \frac{1}{(\omega - \omega_o - \Delta\omega)^2 + (\omega_0/2Q)^2} \tag{3.28}$$

The resonance is given by a Lorentzian with a full width at half maximum equal to ω_0/Q. The Q-factor of the cavity can then be written as:

$$Q = \frac{\omega_0}{\delta\omega} = \omega_0\tau \tag{3.29}$$

where τ is the lifetime of the resonance, which is associated with its linewidth by $\tau = \frac{1}{\delta\omega}$. In real cavities the Q-factor of the resonances is determined by several loss mechanisms, such as absorption, scattering on surface defects, defects inside the glass, diffraction losses and coupling losses [68]. For that reason, the linewidth will be given by the sum of all contributions:

$$\frac{1}{Q} = \sum \frac{1}{Q_i} \tag{3.30}$$

where Q_i are the Q-factors associated with the various loss mechanisms. For silica microsphres, Q-factors of up to 8×10^9 at 633 nm have been reported [75]. The variety of mechanisms than can affect the Q-factor as well as the resonance frequencies for a microsphere grants to this system potential sensor applications, since it becomes very sensitive to the surrounding media conditions. One of these applications is for temperature sensing at the microscale.

3.3 WGMs as temperature sensors

A parameter on optical temperature sensors is the sensitivity (S), which can be defined as the variation of the measured parameter (MP) with the temperature:

$$S = \frac{1}{MP}\frac{dMP}{dT} \tag{3.31}$$

Using this definition one can obtain the relative sensitivity of the WGM displacement as follows [76]:

$$S_{WGM} = \frac{\delta\lambda}{\lambda\delta T} = \left(\frac{1}{N}\frac{\delta N}{\delta T} + \frac{1}{R}\frac{\delta R}{\delta T}\right) \tag{3.32}$$

For fused silica, $\delta N/\delta T = 1.28 \times 10^{-5}$/K and $\delta R/\delta T = 5.5 \times 10^{-7}$/K [77]. Since both coefficients are positive, the peak resonances will experience a redshift in the spectrum if a temperature increase takes place. Taking those values into consideration, it is possible to calculate

the displacement a resonance around 685 nm due to the silica's thermal properties. Figure 6 shows a redshift of approximately 743 GHz or 1.2 nm, for a temperature increment of 50 K around room temperature.

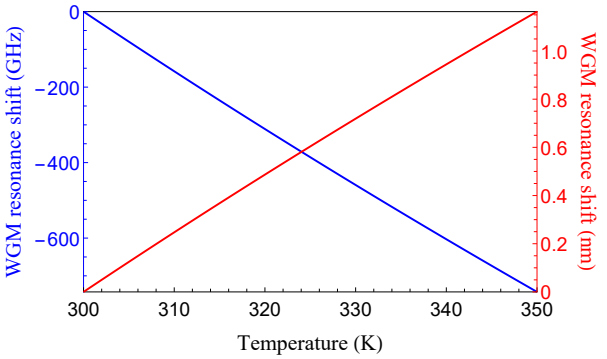

Figure 6 – WGM resonance shift of the 685 nm resonance as a function of temperature for a microsphere of diameter 100 µm. The blue line represents the displacement in gigahertz, while the red one represents the displacement in nanommeters.

The WGM resonance shift can then be greater than the microsphere's FSR (662 GHz), thus another key factor for efficient WGM coupling is keeping the microsphere's temperature stable, since temperature fluctuations are capable of shifting the resonance positions. If one recalls the results from Figure 2, while in that case the thermal effect could be barely detectable for temperature increments of 50 K, in this case, the effect can be overwhelming, and the resonance peak can just be shifted away from the tunable laser source range.

This technique for temperature sensing has some disadvantages. First of all, since it relies on tracking a single mode, it limits the temperature range, which is constrained by the light source that has to be tuned to follow the given mode. Secondly, one cannot determine the actual temperature from the spectrum but rather a relative temperature change. In order to overcome those limitations, one could combine the single mode technique with other techniques for absolute temperature sensing, such as "Fluorescence Intensity Ratio", which could be achieved, for instance, with rare earth-doped micropsheres [76, 77]. If two resonances were tracked at the same time, their spectral separation could be considered as a MP, however, one or both resonances could still lie outside the range of the tunable light source even for temperature increments in the order of tens of Kelvin.

Recently, a barcode-based sensing technique was developed to measure the temperature directly from the WGM spectrum by means of collective multimode information [18]. The transmission spectrum of a WGM resonator has distinct spectral features at different temperatures, such as resonant wavelengths, mode spacing and linewidths. Therefore, the temperature determines the overall aspect of the spectrum and this collective picture could determine the local temperature with high accuracy and range.

In this thesis, different systems for temperature sensing for optical microresonators will be evaluated so that the best candidate can be pointed out for our particular experimental setup.

The systems are based on rare earth-doped yttria nanoparticles which were chosen to match tunable laser sources available for WGM coupling.

Considering the reduced volume of typical microsphere resonators ($1 \times 10^4\,\mu m^3$ to $1 \times 10^6\,\mu m^3$), measuring the surface's temperature accurately without disturbing the mode coupling can be a challenge. A nanoparticle can thus be used to scan the microsphere while its temperature is monitored preferably by means of a contactless technique. For that reason, the influence of bringing a near-field probe close to a microsphere on its Q-factor needs to be taken into consideration.

3.4 Influence of bringing a near-field probe to the WGM

The ideal configuration for scanning the microsphere's surface with a nanometric probe would be placing the NP directly at the intensity maximum of the WGM around its equator, which can be achieved by attaching the NP to the end of a near-field probe [78, 79]. The temperature could be measured at any given point of the microsphere's surface, since the thermal equilibrium is assumed. However, the equator where the WGMs has an intensity maximum gives the opportunity to assess the temperature from the fluorescence of a doped nanoprobe. Unfortunately, the fiber holding the NP also couples to the WGM and thus introduces an additional loss mechanism, which can be written as [80]:

$$1/Q_{total}(z) = 1/Q_0 + 1/Q_{tip}(z) \tag{3.33}$$

where z is the distance fom the tip to the sphere's surface and $Q_{tip}(z)$ is the induced loss mechanism, which can be assumed to be exponentially decreasing along z, due to the nature of the evanescent field outside the microsphere [80]. Moreover, the Q-factor reduction due to the presence of a fiber probe is expected to be less pronounced if the initial Q-factor, Q_0, is smaller.

In order to get a qualitative understanding on the effects of the interaction between the near-field probe and the microsphere, one can consider the Rayleigh scattering applied to a sphere of radius r (not to be confused with the microsphere's radius R) which is small when compared to the mode wavelength. Additionally, the mode field will be assumed to be as a plane monochromatic wave, while in the real experiment the tip is placed in an evanescent field. For the Rayleigh approximation the extinction cross section σ can be written as [81]:

$$\sigma = \frac{8\pi}{3}\left(\frac{2\pi n_{\text{med}}}{\lambda_0}\right)^4 r^6 \left|\frac{\epsilon^2 - 1}{\epsilon^2 + 2}\right|^2 \tag{3.34}$$

where λ_0 is the vacuum wavelength, ϵ is the dielectric constant and N_{med} is the refractive index of the surrounding medium. The Rayleigh extinction cross section is clearly proportional to λ_0^{-4} and there's is a strong dependency on the radius of the scattering particle (r^6). The term $\left(\frac{2\pi N_{\text{med}}}{\lambda_0}\right)$ can be written as the wavenumber k so that Equation 3.34 can be rewritten as [68]:

$$\sigma = \frac{8\pi}{3} k^4 r^6 \left| \frac{\epsilon - 1}{\epsilon + 2} \right|^2 \tag{3.35}$$

Assuming a fundamental mode of volume V_{mode} in a silica microsphere of radius R, light propagates in a circle around the sphere's equator losing energy in every round trip when reaching the scatterer. The loss is given by the ratio of areas:

$$\frac{\Delta E}{E_0} = \frac{\sigma \frac{I(d)}{I_0}}{A_{\text{mode}}}, \tag{3.36}$$

where E_0 is the energy stored in the resonator and A_{mode} is the cross section through the mode volume, $A_{\text{mode}} = \frac{V_{\text{mode}}}{2\pi a}$. $I(d)$ is the radial intensity distribution which can be calculated from the radial field distribution and d is the distance to the microsphere's surface. $\frac{I(d)}{I_0}$ is thus the normalized intensity distribution, which takes into account the fact that the losses will be lower in regions where the intensity is lower. As the scatterer lies outside the microsphere, $I(d)$ is given by the exponentially decaying evanescent field:

$$I(d) = |\mathbf{E}(d)|^2 \propto e^{-2d/r^*} \tag{3.37}$$

where:

$$r^* \approx \lambda/2\pi \times \left(\sqrt{N^2 - 1} \right) \tag{3.38}$$

r^* is the decay length of the evanescent field. After one round trip, the energy will be decreased to a value $E_{rt} = E_0 - \Delta E$. Combining Equations 3.36 and 3.37, one gets:

$$\frac{E_{rt}}{E_0} = 1 - \frac{\Delta E}{E_0} = 1 - \frac{\sigma}{A_{\text{mode}}} e^{-2d/r^*} \tag{3.39}$$

The energy inside the resonator $E(t)^*$ will be proportional to the square of the field inside the cavity. The temporal evolution can be found by inserting Equation 3.29 into Equation 3.25, which gives:

$$E(t)^* = E_0 e^{-t/\tau} \tag{3.40}$$

while the decay time is given by:

$$\frac{1}{\tau} = \frac{1}{\tau_0} + \frac{1}{\tau_{sct}} \tag{3.41}$$

since $\tau \propto Q$. τ_0 is the decay time of the cavity in the absence of the scatterer and τ_{sct} is the decay time due to the losses introduced by the scatterer. The time spent for one round trip is given by:

$$t_{rt} = \frac{2\pi RN}{c} \tag{3.42}$$

Therefore, the left hand side of Equation 3.39 can be rewritten as:

$$\frac{E_{rt}}{E_0} = e^{-t_{rt}/\tau_0} e^{-t_{rt}/\tau_{sct}} \tag{3.43}$$

thus:

$$e^{-t_{rt}/\tau_0} e^{-t_{rt}/\tau_{sct}} = 1 - \frac{\sigma}{A_{\text{mode}}} e^{-2d/r^*} \tag{3.44}$$

For a high Q-factor microsphere, $t_{rt} \ll \tau_0$, thus the decay constant can be determined as:

$$\tau_{sct} = \frac{t_{rt}}{-\ln\left(1 - \frac{\sigma}{A_{\text{mode}}} e^{-2d/r^*}\right)} \tag{3.45}$$

one can calculate the Q-factor using Equation 3.30:

$$\frac{1}{Q_{\text{total}}} = \frac{1}{Q_0} + \frac{1}{Q_{sct}} \tag{3.46}$$

with $Q_{sct} = \omega_0 \tau_{sct}$. The total Q-factor is then given by:

$$Q_{\text{total}} = \frac{1}{\frac{1}{Q_0} - \frac{\ln\left(1 - \frac{\sigma}{A_{\text{mode}}} e^{-2d/r^*}\right)}{t_{rt}\omega_0}} \tag{3.47}$$

Setting the distance from the probe to the microsphere's surface equal to zero, it can be shown that for a probe radius of 50 nm, the Q-factor degrades by a factor of about 30%. This could be an overestimation considering the model's limitations. However, it gives a starting point for considering the effects of placing a near-field probe close to microsphere's surface. Considering the high Q-factors that can be reached with silica microspheres, such degradation can still be considered as a trade-off for the benefits of avoiding the single mode tracking technique.

The next chapter will discuss in more detail the instrumental aspects for WGM coupling and for Scanning Near-Field Optical Microscopy. The system was optimized for both the optical microresonators and for the fluorescence microscopy required for temperature sensing using rare earth-doped yttria nanoparticles.

4 INSTRUMENTATION FOR WGMs EXCITATION

In this chapter, some preliminary aspects of the experimental setup for WGMs spectroscopy will be described. Several control experiments were performed in order to optimize the setup as well as to calibrate the instruments. The microsphere-prism coupling geometry was taken into consideration in order to position the focusing lens while the scanning frequency was monitored using a Fabry-Perot interferometer. Using those procedures, pairs of TE/TM modes were observed, thus giving a starting point for efficient light coupling.

4.1 Phase matching condition for microsphere-prism coupling

In order to achieve phase matching conditions for light coupling in a microsphere, it is necessary that the light emerges from the evanescent spot in such an angle that the transmitted wave reaches the sphere's surface tangentially. That can be done by adjusting the incidence angle γ with respect to the prism surface. The incident wave in the coupling prism can be approximated as a finite-width Gaussian beam and the complete calculation of the evanescent intensity for that geometry is well-known [82]. The evanescent intensity profile can be approximated by an asymmetric Gaussian shape for most practical situations and the evanescent penetration depth does not vary appreciably at the xy plane. The widths of the profile can thus be adjusted by changing the incidence angle and/or the ratio of the focal length of the lens to the incident beam's waist.

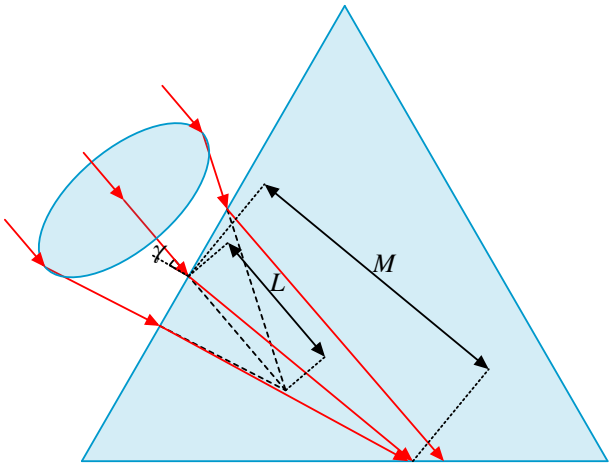

Figure 7 – Prism coupling geometry. L is the distance between the prism's surface and the lens' focal point if the refraction inside the prism is neglected. M is the actual focal distance after the light propagates inside the prism and is directed to sphere's surface (not shown in the diagram). The z-axis points outwards from the page.

Figure 7 shows the parameters describing a laser beam of vacuum wavelength λ_0 and

of Gaussian intensity profile which is focused by a lens inside a triangular prism and then is internally reflected. The original direction of propagation of the beam and the optical axis of the lens are colinear and make an angle γ with the normal to the air/prism interface and the angle μ defines the exit pupil of the lens. The refractive indices of the air and prism are n_a and n_p respectively. The center of the focused beam in the absence of the prism does not lie on the prism/sphere interface. The distance between the air/prism interface and this central focal point is defined as L and is determined by the focal length of the lens. The angle θ refers to the change in direction after refraction at the air/prism interface, and is given by:

$$\theta = \gamma - \sin^{-1}\left[n_a \frac{\sin(\gamma)}{n_p}\right] \tag{4.1}$$

Following Snell's law and assuming $n_a = 1$, for an equilateral triangle prism, one gets:

$$\sin^{-1}\left(\frac{\sin(\gamma)}{n_p}\right) + \sin^{-1}\left(\frac{n_s}{n_p}\right) = \frac{\pi}{3}, \tag{4.2}$$

where n_p and n_s are the refractive indexes of the prism and microsphere respectively. The angle γ is expected to be small, so Equation 4.2 can be approximated up to the first order to isolate γ:

$$\gamma \approx n_p\left(\frac{\pi}{3} - \sin^{-1}\left(\frac{n_s}{n_p}\right)\right) \tag{4.3}$$

For typical values for $n_{p,s}$, values of γ of about 2 degrees are found, so a perpendicular incidence at the prism's surface can be used as a starting point to find optimal coupling conditions. Once this condition is roughly satisfied, the evanescent focusing spot might become visible once a microsphere or a scanning probe is brought close to it. In either situation, such devices need to be brought close to the prism in a controlled manner, so a 3D piezoelectric stage can be used to control their position with nanometric precision. On the other hand, the piezo stages need to be properly calibrated, so the displacements can be accurately determined by the supply voltage in each axis. In order to do so, a Michelson interferometer was used to calibrate the piezo stages, as will be described in the next section.

4.2 Calibrating a 3D piezo stage with a Michelson interferometer

Apart from controlling the position of a microsphere, a 3D piezo stage can also be used for scanning its surface for spatial mode distribution. Therefore, a proper calibration is necessary in order to avoid distortions in the images as well as to monitor the actual position of the scanning probe. Calibration for the stage took place by means of a Michelson Interferometer (MI) built in such a way that each one of the three axis of the piezo stage coincided with a movable mirror.

The MI splits a single beam of light into two paths, one of which is directed to a fixed mirror (M_2) and the other goes to a movable mirror (M_1), as shown in Figure 8. Both beams are

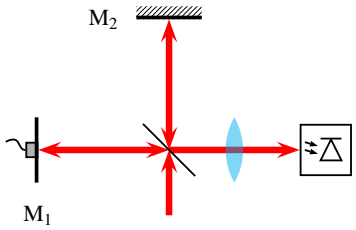

Figure 8 – Michelson interferometer. M_1: movable mirror, M_2: fixed mirror. After being splitted, the light beams are focused at a photodiode.

recombined at a photodetector so the light intensity profile can be recorded as a function of the movable mirror's position. Since the beams travel over two different paths to a detector, the field at the detector will be determined by the optical path difference:

$$\Delta x = 2(x_1 - x_2) = \delta \tag{4.4}$$

$$\Delta\phi_\delta = 2k(x_1 - x_2) \tag{4.5}$$

where x_1 and x_2 are the positions of (M_1) and M_2, respectively. Changing x_1 changes the phase shifts between destructive and constructive interference. For a given fringe order $m \in \mathbb{Z}$, constructive interference happens when the waves are in phase ($\Delta\phi = 2m\pi$), and destructive interference happens when the waves are opposite in phase ($\Delta\phi = (2m+1)\,\pi$). If M_1 moves a distance $\frac{\lambda}{2}$ then the incident ray of light has to travel an extra distance $\frac{\lambda}{2}$ to reach the mirror and then the reflected ray of light has to move an extra $\frac{\lambda}{2}$, thus a total extra distance of λ. If the path length changes by one wavelength then there is a movement of one fringe.

In order to calibrate the piezo stage a HeNe laser (632.8 nm) was used as a light source and a small mirror was mounted on each one of the piezo's axis. An increasing voltage ramp was supplied to the piezo while the photodectector signal was recorded by an oscilloscope. the voltage ramp is also sent to the oscilloscope for reference. The peaks at the photodetector are correlated to the corresponding voltage reading so the M_1 displacement can be calculated as a function of the supplied voltage, as shown in Figure 9.

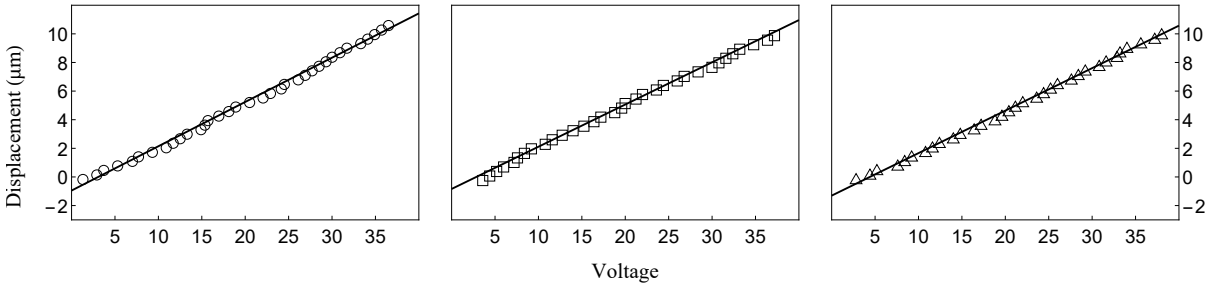

Figure 9 – 3D piezo stage calibration. From left to right, the x, y and z-axis. The solid lines represent the best linear fit.

Following the MI method, a calibration factor of approximately 30 µm/100 V was observed for all three axes, which matches the manufacturer's specifications. This factor is then incorporated into the control software, taking into account the gain introduced by the amplification circuitry. Once the piezo unit is properly calibrated, it can be used to control a Scanning Near-Field Optical Microscopy (SNOM) probe. The probe can then be brought within a few nanometers of surfaces such as the microsphere or the prism *xy* plane.

The SNOM probe's distance from a given surface can be set by means of shear force feedback mode. In that configuration, a tuning fork is mounted alongside the tip and made to oscillate at its resonance frequency. The amplitude is related to the tip-surface distance, and thus used electronically as a feedback mechanism, as will be described in the next section.

4.3 Determining the resonance frequency of a quartz tuning fork

SNOM probes were made by gluing a fine silica tip on top of a quartz tuning fork (WTL International Limited with resonance frequency of 75 kHz). The tips were obtained by controlled heat and pulling of an optical fiber. Once the tips are glued with instant glue to the top tine at the tuning fork, additional epoxy glue is added at the base of the tuning fork for stability, as shown in Figure 10.

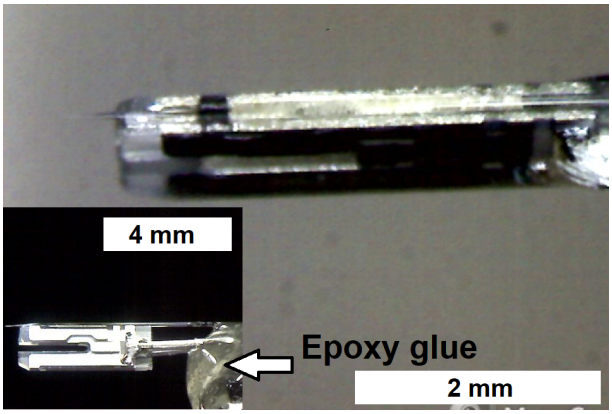

Figure 10 – SNOM probe composed of a fiber tip on top of a quartz tuning fork.

Quartz crystal tuning forks (QTF) consist of two tines connected at one end and capable of maintaining a selected resonance frequency in a wide temperature range. Since quartz is a piezoelectric material, a mechanical stress can be converted to an electric signal and vice versa. Their resonance frequencies are determined by the elastic properties of quartz as well as their shapes and sizes [83].

The mode shape and resonance frequency of a QTF can be found by considering one tine of the fork as a cantilever beam vibrating in flexure [84, 85]. In the fundamental flexural mode of oscillation, the tines move in opposite directions and the centre of mass remains stationary [86]. The flexural dynamics of a vibrating beam can be seen for example in [84] and a brief review

follows below.A body acted on by an external force will experience a deformation that can be described by two types of strain tensors. The first one describes the relative elongation δ of a bar of length l and is defined by[1]:

$$\epsilon = \frac{\delta}{l} \tag{4.6}$$

where the strain ϵ is in the same direction as the stress. As long as the deformed body is in its elastic regime, there will be a linear relationship between the stress σ and the strain at any given point in the body:

$$\sigma = E\epsilon \tag{4.7}$$

where E is the Young's modulus. The second kind of strain, γ, is the relative deformation in a direction perpendicular to the direction of the stress, given by:

$$\tau = G\gamma \tag{4.8}$$

where G is the shear modulus of elasticity. The constants E and G, therefore, describe the resistance of the lever to bending. For the first kind of strain tensor, it can be shown that:

$$\delta = \frac{lF}{AE} \tag{4.9}$$

Which relates the external force to the elongation of a spring.

Consider a bent beam with its associated parameters as shown in Figure 11. The bending gives rise to a compression above a line passing through the center of the beam and a dilation below that line. This line, along which there is no compression or dilation, is called the neutral axis.

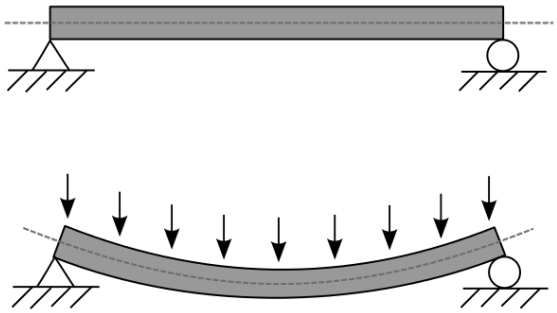

Figure 11 – Neutral axis in a bent body. zy is the plane of the page while x points outwards.

If the beam's cross section is symmetric, isotropic and not curved before bending, the neutral axis is at the geometric centroid. The angle of bending, $d\phi$, is related to the distance ds

[1] Tensorial notation was omitted for simplicity

by $R = \frac{ds}{d\phi}$, where R is the bending radius. Similarly, the deformation of a section of the beam at a distance z to the neutral axis is $dy = zd\phi$, which yelds the strain:

$$\epsilon = -\frac{dy}{ds} = \frac{-z}{R} \Rightarrow \sigma = -\frac{Ez}{R} \tag{4.10}$$

Therefore, both the stress and strain are proportional to the distance z to the neutral axis. At equilibrium, the external moment M will equal the internal moments generated by the stress that are distributed throughout any given cross section A. The area moment of inertia is given by:

$$I = \int_A z^2 dA \tag{4.11}$$

and the external moment is give by:

$$M = \int_A z\sigma dA \tag{4.12}$$

Therefore, it can be showed that:

$$R = \frac{EI}{M} \tag{4.13}$$

From the curvature of a plane curve:

$$\frac{1}{R} = \frac{\frac{d^2z}{dy^2}}{\left[1 + \left(\frac{dz}{dy}\right)^2\right]^{\frac{3}{2}}} \tag{4.14}$$

And defining a shear force V by:

$$V = \frac{\partial M}{\partial y} \tag{4.15}$$

and then equating dV acting on an element of mass $\rho A dy$ with the acceleration, one gets:

$$dV = -\rho A dy \frac{\partial^2 z}{\partial t^2} \tag{4.16}$$

However, if the slope of z is small compared to the unit, Equations 4.13 and 4.13 can be used to state that:

$$\frac{\partial^2 z}{\partial y^2} = \frac{M}{EI} \tag{4.17}$$

Therefore, the motion equation for the lever is:

$$EI\frac{\partial^4 z}{\partial y^4} + \rho A \frac{\partial^2 z}{\partial t^2} = 0 \tag{4.18}$$

whose solution is:

$$z(y,t) = z(y)\left[\cos\left(\omega_j t + \theta\right)\right], \tag{4.19}$$

where j is the order of the mode. Equation 4.18 can be written as:

$$\frac{d^4 z(y)}{dy^4} = \kappa^4 z(y) \tag{4.20}$$

where:

$$\kappa^4 = \frac{\omega_j^2 \rho A}{EI} \tag{4.21}$$

The solution for Equation 4.20 is:

$$z(y) = A_1 \sin \kappa y + A_2 \cos \kappa y + A_3 \sinh \kappa y + A_4 \cosh \kappa y \tag{4.22}$$

The present work is interested in vibrating lever attached at a fixed point. Considering the fixed point at $z = 0$, the deflection and slope can be written as:

$$z(0) = \frac{\partial z(y)}{\partial y}\Big|_{y=0} = 0 \tag{4.23}$$

Meanwhile, the moment and shear force at the lever's vibrating end shall be null, implying the following boundary conditions:

$$\frac{\partial^2 z(y)}{\partial y^2}\Big|_{y=l} = \frac{\partial^3 z(y)}{\partial y^3}\Big|_{y=l} = 0 \tag{4.24}$$

Therefore, the equation for the modes is:

$$\cos(\kappa l)\cosh(\kappa l) + 1 = 0 \tag{4.25}$$

For a rectangular lever, $I = \frac{wt^3}{12}$, where w is the width and t is the thickness of the lever, which are perpendicular and parallel to the direction of the bending, respectively. The resonance frequencies are given by:

$$\omega_j = \frac{\kappa_j^2 t}{\sqrt{12}}\sqrt{\frac{E}{\rho}} \Rightarrow f_0 = \frac{0.162t}{l^2}\sqrt{\frac{E}{\rho}} \tag{4.26}$$

with the relevant constants given by Table 2. Using the values from Table 2, Equation 4.26 yields a fundamental resonance frequency of approximately 72 kHz, close to the manufacturer's specifications.

QTF dimensions		E	ρ	κl		Resonance Frequency	
length	thickness	78.7 GPa	2650 kg/m^3	j=0	j=1	Calculated	Measured
4.0 mm	1.3 mm			1.875	4.694	72 kHz	75 kHz

Table 2 – QTF parameters [87, 88]. The measured resonance frequency matched the manufacturer's specifications, while the calculated one turned out to be 4% smaller.

The resonance frequency and quality factor of the both the bare QTF and the SNOM probe were measured using a sinusoidal signal from a function generator to drive the tuning forks at a variable frequency and constant amplitude. The signal goes to a preamplifier to compensate for the parasitic capacitance of the tuning fork, then it is amplified by a factor of 50 and detected by a lock-in amplifier. The variable frequency of the function generator also acts as a reference for

the lock-in. The Q factor is determined by a Lorentzian fit around the resonance. The Q factors of a QTF were found to be around 5000, while the ones for a SNOM probe were found to be around 2500, as shown in Figure 12.

Compared to the bare QTF, the SNOM probes showed lower Q factors, which is desired for SNOM applications and higher resonance frequencies, around 77 kHz. The reason for the lower Q factors can be attributed to the damping introduced by the tip and glue [89]. On the other hand, the blueshift in resonance frequency suggests an increased stiffness of the system [88]. It is worthwhile to mention that the cantilever-based model for QTF has lead to discrepancies in the literature for the calculation of the spring constant and resonance frequency so other approaches such as the finite element analysis were developed [90].

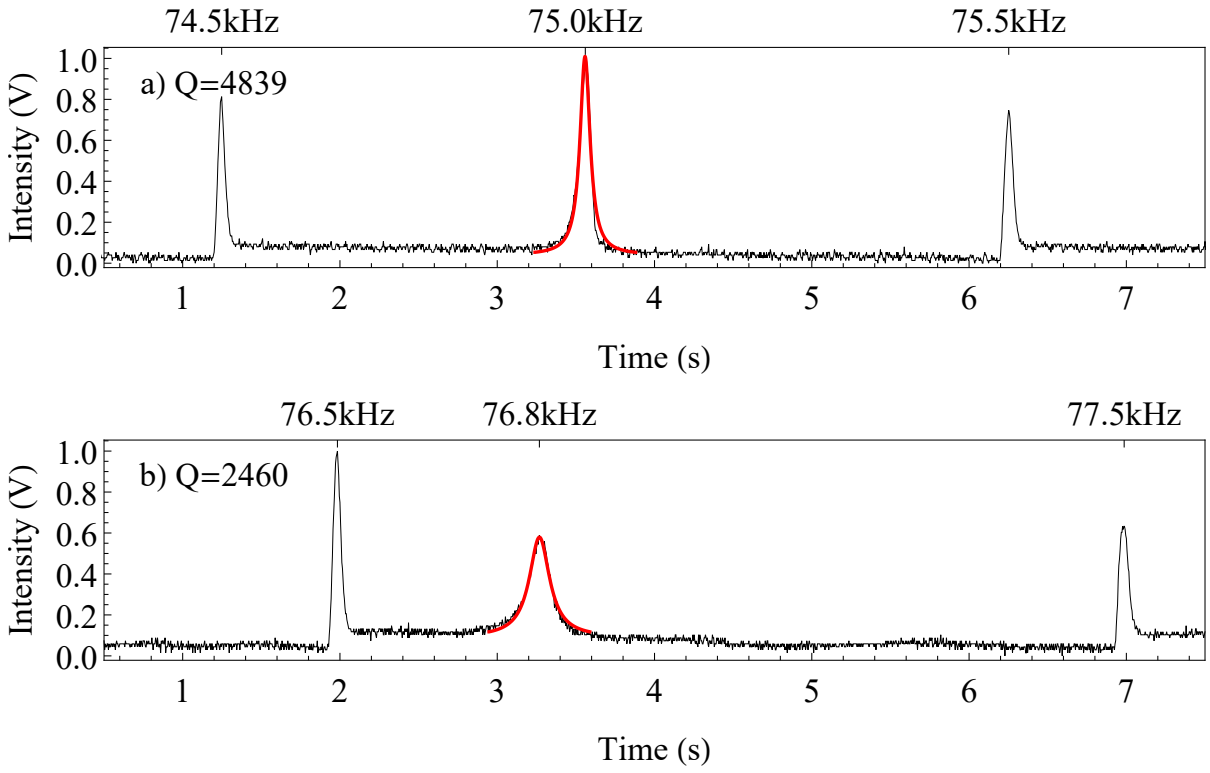

Figure 12 – Resonance of a quartz tuning fork (a) and of a SNOM probe after the fiber tip is glued (b). The Q factors are respectively 4839 and 2460, while the resonance frequencies are 75 kHz and 76.8 kHz. The lower x-axis is a time scale, during which the frequency sweeps 1 kHz in 5 s. The red curves are Lorentzian fits around the resonance peaks. The peaks around the resonance are caused by the frequency generator when the sweep starts or stops.

One of the possible applications for a SNOM probe is to develop a homemade surface probe for topological measurements with nanometric accuracy. For our analysis, it can be useful to determine the radius of a given microsphere without disturbing the system, so the SNOM probe can be a good candidate for such task. In the next section, an algorithm for fitting a 3D set of points to a surface will be described so it can be applied to a system similar to the one in use

in this work.

4.4 Measuring a microsphere's radius using a SNOM probe

The microsphere's radius is a crucial factor to calculate the WGM resonances and FSR. A SNOM probe can be used to determinate such quantities in a non-destructive manner, since it can scan over a surface very close (typically less than 100 nm) to the microsphere's and with small fluctuations (about 10 nm). Once the spatial positions of the probe are known, the spherical surface can be fitted using least squares method [91]. The procedure is described as follows:

Given a set of points:

$$\begin{bmatrix} x_1 & y_1 & z_1 \\ x_2 & y_2 & z_2 \\ x_3 & y_3 & z_3 \\ \vdots & \vdots & \vdots \\ x_n & y_n & z_n \end{bmatrix} \tag{4.27}$$

those points are obtained by the 3D movement of the SNOM probe, using the calibration factor measured with the MI apparatus. From those points, the goal is to find the best fit to a sphere of equation:

$$(x-a)^2 + (y-b)^2 + (z-c)^2 = r^2, \tag{4.28}$$

where (a, b, c) is the sphere's center and r is the radius. Assuming that not all points are coplanar, one has to minimize the function:

$$F(a, b, c, r) = \sum_{i=1}^{n} (r_i - r)^2, \tag{4.29}$$

where:

$$r_i = \sqrt{(x_i - a)^2 + (y_i - b)^2 + (z_i - c)^2} \tag{4.30}$$

Taking the partial derivative of F with respect to r on Equation 4.29:

$$\frac{\partial F}{\partial r} = -2 \sum_{i=1}^{n} (r_i - r) \tag{4.31}$$

and making it equal to zero:

$$r = \frac{1}{n} \sum_{i=1}^{n} r_i \tag{4.32}$$

Similarly, taking the other partial derivatives and making them equal to zero:

$$\begin{aligned} a &= \frac{1}{n}\sum_{i=1}^{n} x_i + \frac{r}{n}\sum_{i=1}^{n}\frac{\partial r_i}{\partial a} \\ b &= \frac{1}{n}\sum_{i=1}^{n} y_i + \frac{r}{n}\sum_{i=1}^{n}\frac{\partial r_i}{\partial b} \\ c &= \frac{1}{n}\sum_{i=1}^{m} z_i + \frac{r}{n}\sum_{i=1}^{n}\frac{\partial r_i}{\partial c} \end{aligned} \tag{4.33}$$

From Equation 4.30:

$$\begin{aligned} \frac{\partial r_i}{\partial a} &= \frac{(a - x_i)}{r_i} \\ \frac{\partial r_i}{\partial b} &= \frac{(b - y_i)}{r_i} \\ \frac{\partial r_i}{\partial c} &= \frac{(c - z_i)}{r_i} \end{aligned} \tag{4.34}$$

Combining Equations 4.32, 4.33 and 4.34, one gets:

$$\begin{aligned} a &= \frac{1}{n}\sum_{i=1}^{n} x_i + \frac{1}{n^2}\sum_{i=1}^{n} r_i \sum_{i=1}^{n}\frac{(a - x_i)}{r_i} \\ b &= \frac{1}{n}\sum_{i=1}^{n} y_i + \frac{1}{n^2}\sum_{i=1}^{n} r_i \sum_{i=1}^{n}\frac{(b - y_i)}{r_i} \\ c &= \frac{1}{n}\sum_{i=1}^{n} z_i + \frac{1}{n^2}\sum_{i=1}^{n} r_i \sum_{i=1}^{n}\frac{(c - z_i)}{r_i} \end{aligned} \tag{4.35}$$

The center of the sphere is given by the solution of Equation 4.35 while the radius is given by Equation 4.32. However, finding analytical solutions is cumbersome due to the dependency of r_i on (a, b, c). In order to overcome this problem, one could try an iterative solution. That approach required a large amount of iterations and thus a long machine time. An alternative is to modify Equation 4.29 as:

$$G\left(a, b, c, r^2\right) = \sum_{i=1}^{n}\left(r_i^2 - r^2\right)^2 \tag{4.36}$$

which is also a reasonable guess for an optimization function. Then, Equation 4.32 becomes:

$$r^2 = \frac{1}{n}\sum_{i=1}^{n} r_i^2 \tag{4.37}$$

The squared radius becomes the average of the squared distances from the sample points

to the center (a, b, c). Now, taking the partial derivative of G with respect to the other parameters:

$$\begin{aligned}
\frac{\partial G}{\partial a} &= 4 \sum_{i=1}^{n} \left(r_i^2 - r^2\right)(a - x_i) = 0 \\
\frac{\partial G}{\partial b} &= 4 \sum_{i=1}^{n} \left(r_i^2 - r^2\right)(b - y_i) = 0 \\
\frac{\partial G}{\partial c} &= 4 \sum_{i=1}^{n} \left(r_i^2 - r^2\right)(c - z_i) = 0
\end{aligned} \tag{4.38}$$

It is convenient to introduce a vector notation. Let:

$$\mathbf{C} \equiv (a, b, c) \tag{4.39}$$

$$\mathbf{X_i} \equiv (x_i, y_i, z_i) \tag{4.40}$$

$$\mathbf{\Delta_i} \equiv \mathbf{C} - \mathbf{X_i} \tag{4.41}$$

$$\mathbf{A} \equiv \frac{1}{n} \sum_{i=1}^{n} \mathbf{X_i} \tag{4.42}$$

$$\mathbf{B_i} \equiv \mathbf{X_i} - \mathbf{A} \tag{4.43}$$

Equation 4.38 can be written as:

$$\sum_{i=1}^{n} \left(\mathbf{\Delta_i^T \Delta_i} - r^2\right) \mathbf{\Delta_i} = 0 \tag{4.44}$$

And for Equation 4.37:

$$r^2 = \frac{1}{n} \sum_{i=1}^{n} \mathbf{\Delta_i^T \Delta_i} \tag{4.45}$$

Some algebraic manipulation leads to:

$$\mathbf{\Delta_i^T \Delta_i} = |\mathbf{C}|^2 - 2\mathbf{C^T X_i} + |\mathbf{X_i}|^2 \tag{4.46}$$

$$r^2 = |\mathbf{C}|^2 - 2\mathbf{C^T A} + \frac{1}{n} \sum_{i=1}^{n} |\mathbf{X_i}|^2 \tag{4.47}$$

Thus:

$$\mathbf{\Delta_i^T \Delta_i} - r^2 = 2\mathbf{C^T}\left(\mathbf{A} - \mathbf{X_i}\right) + |\mathbf{X_i}|^2 - \frac{1}{n} \sum_{i=1}^{n} |\mathbf{X_i}|^2 \tag{4.48}$$

Now, one can go back and solve Equation 4.44. After some more algebra:

$$2\left(\sum_{i=1}^{n} \mathbf{B_i B_i^T}\right)(\mathbf{C} - \mathbf{A}) = \sum_{i=1}^{n} \left(\mathbf{B_i^T B_i}\right) \mathbf{B_i} \tag{4.49}$$

It's more convenient to write the previous equation in the form of a linear system of equations:

$$\underbrace{2\left[\sum_{i=1}^{n} (\mathbf{X_i} - \mathbf{A})\, \mathbf{X_i}\right]}_{\mathbf{D}} \mathbf{C} = \underbrace{\sum_{i=1}^{n} (\mathbf{X_i} - \mathbf{A})\, |\mathbf{X_i}|^2}_{\mathbf{E}} \tag{4.50}$$

Then:

$$\mathbf{D} = 2\begin{bmatrix} \sum_{i=1}^{n} x_i\,(x_i-\bar{x}) & \sum_{i=1}^{n} x_i\,(y_i-\bar{y}) & \sum_{i=1}^{n} x_i\,(z_i-\bar{z}) \\ \sum_{i=1}^{n} y_i\,(x_i-\bar{x}) & \sum_{i=1}^{n} y_i\,(y_i-\bar{y}) & \sum_{i=1}^{n} y_i\,(z_i-\bar{z}) \\ \sum_{i=1}^{n} z_i\,(x_i-\bar{x}) & \sum_{i=1}^{n} z_i\,(y_i-\bar{y}) & \sum_{i=1}^{n} z_i\,(z_i-\bar{z}) \end{bmatrix} \tag{4.51}$$

$$\mathbf{E} = \begin{bmatrix} \sum_{i=1}^{n} \left(x_i^2+y_i^2+z_i^2\right)(x_i-\bar{x}) \\ \sum_{i=1}^{n} \left(x_i^2+y_i^2+z_i^2\right)(y_i-\bar{y}) \\ \sum_{i=1}^{n} \left(x_i^2+y_i^2+z_i^2\right)(z_i-\bar{z}) \end{bmatrix} \tag{4.52}$$

Equation 4.50 can be solved by the operation:

$$\mathbf{C} = \begin{bmatrix} a \\ b \\ c \end{bmatrix} = \mathbf{D}^{-1}\mathbf{E} \tag{4.53}$$

Equation 4.53 is much simpler to be applied to a set of points than Equation 4.35. It also has the advantage of being a non-iterative solution. As before, the microsphere's radius is given by Equation 4.37. Figure 13 shows a simulation of this optimization procedure. Here, some data was generated for a SNOM probe scanning right above a 50 µm radius sphere in 50 steps of 100 nm each. A random fluctuation of 10 nm was added to each z coordinate. The probe advanced about 125 nm along the z-axis with respect to its maximum position (z=0 at x, y=0). That translates to a radius of 49.5 µm fitted by the algorithm, close to the actual radius.

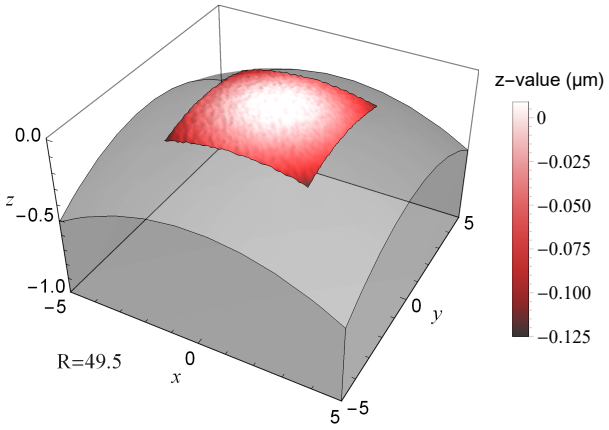

Figure 13 – SNOM probe imaging at a 5 µm by 5 µm area (red) on top of a microsphere (gray). All units in micrometers.

The center of the sphere is measured at a reference frame given by the SNOM tip, say the center of the xy scan. Therefore, it is possible to measure the radius even if a pole of the sphere is not perfectly centered during the scan. The relative coordinates can be used to correct this offset. Unfortunately, shortly after the SNOM apparatus was optimized for topological measurements, two of the three available 3-axis piezo units showed malfunctions and required a complete refurbishment. The process of sending the units all the way to the manufacturer's headquarters in

Germany and getting them back took over one year so no further tests could be performed with the SNOM apparatus.

Moving forward with the control experiments, it's also necessary to calibrate the spectral displacement of the pump laser for whisper galley modes coupling. That was achieved by means of a spherical mirror Fabry-Perot interferometer, which will be the topic of the next section.

4.5 The spherical mirror Fabry-Perot interferometer

The Fabry-Perot spherical interferometer (FPS) is composed of two identical spherical mirrors separated by a distance very close to their common radius of curvature [92]. Light entering the etalon undergoes multiple reflections and the interference causes a modulation in the transmitted and reflected beams. The FPS can thus be used to measure a detuning in the light frequency while the laser is scanned in real time.

If the axial mirror spacing is $r + \epsilon$, with $|\epsilon| \leq \lambda$, the light path after two round trips is smaller than the paraxial path $4r$ by an amount [93]:

$$\Delta\left(\rho\right) \approx \frac{\rho^4}{r^3} + \frac{4\epsilon\,\rho^2}{r^2} \tag{4.54}$$

where ρ is the height at which an entering ray crosses the central plane of the FPS for a small distant source close to the interferometer's axis. A change of $\frac{\lambda}{4}$ in the mirror separation scans through a free spectral range of:

$$FSR = \frac{c}{4\left(r + \epsilon\right)} \tag{4.55}$$

In Figure 14, for each entering ray there are two sets of transmitted rays: those which have been reflected $4m$ times, emerging from point P_1 and those which have been reflected $(4m + 2)$ times, emerging from point P_2, where m is an integer.

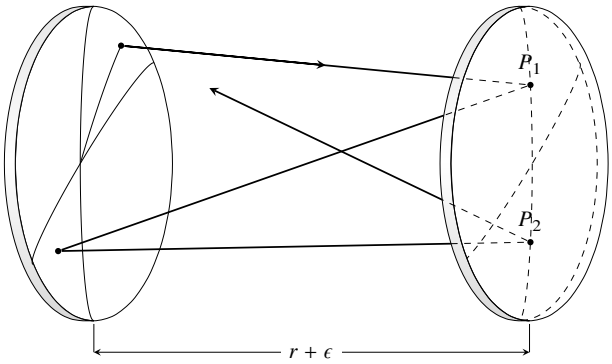

Figure 14 – General ray path in a FPS. r: radius; ϵ: perturbation from the confocal configuration

The condition for bright fringes in the central plane of the interferometer is obtained making Equation 4.54 equal to $m\lambda$. Fringes thus have radii given by [93]:

$$\rho_m = \left[-2\epsilon r \pm \left(4\epsilon^2 r^2 + m\lambda r^3 \right)^{\frac{1}{2}} \right]^{\frac{1}{2}} \tag{4.56}$$

Figure 15 shows the fringe pattern in cross section. From Equation 4.56, if $\epsilon > 0$, ρ_m is single-valued and $m > 0$. If $\epsilon < 0$, ρ_m is two-valued for $m \leq 0$ and single-valued for $m > 0$. From the same equation, it can be shown that the radial dispersion in the fringe pattern is nonlinear near the axis when the FPS is precisely confocal. This provides the basis for the high étendue[2] which is characteristic of this instrument. At constant finesse, as resolving power increases, so does the étendue. By contrast, in a flat-plate interferometer as resolving power increases the étendue decreases, therefore an increase in light intensity decreases resolution.

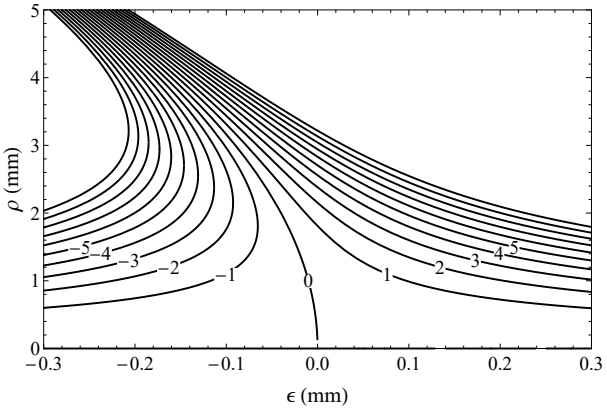

Figure 15 – Near confocal FPS fringe patterns. At each value of ϵ, the solid curves give the radii of the circular interference fringes for a monochromatic light source and a bright fringe on the axis. In this simulation, λ=685 nm and r=25 mm. The numbers on the curves indicate the fringe order.

From Figure 15, in order to operate at the zeroth order fringe, ρ_m must be around 500 µm, which is easily attainable with regular focusing lens. Therefore, the alignment for the FPS is of paramount importance for a proper calibration. This can be further explored introducing the spectral resolving power ($\mathcal{R}$) of a spectroscopic instrument, which can be defined as:

$$\mathcal{R} = \frac{\nu}{\Delta\nu_m} = \frac{\lambda}{\Delta\lambda_m} \tag{4.57}$$

where $\Delta\nu_m$ is the minimum resolvable frequency increment in the vicinity of a frequency ν.

The ratio of the FSR and the instrumental width gives the finesse $\mathcal{F}$ of the interferometer, which is a measure for how narrow the resonances are with respect to their frequency distance.

$$\mathcal{F} = \frac{FSR}{\Delta\nu_m} \tag{4.58}$$

From Equations 4.55, 4.57 and 4.58, the resolving power can be written in terms of $\mathcal{F}$ as:

[2] Étendue is defined as the radiation from a source within a solid angle, Ω, subtended by an aperture with area A.

$$\mathcal{R} = \frac{4\,(r+\epsilon)\,\mathcal{F}}{\lambda} \tag{4.59}$$

which in turn quantifies the capability of an interferometer to resolve two close wavelengths. An experimentally measured finesse has a number of contributions, particularly the mirror reflective losses and the correction for spherical aberration. An expression for the total finesse can be written as:

$$\mathcal{F}_t = \left[\left(\frac{1}{\mathcal{F}_r}\right)^2 + \left(\frac{1}{\mathcal{F}_a}\right)^2\right]^{-\frac{1}{2}} \tag{4.60}$$

where $\mathcal{F}_r$ accounts for the reflection losses and $\mathcal{F}_a$ for the spherical aberration. For mirrors with reflectivity close to unit, we have [94]:

$$\mathcal{F}_r = \frac{\pi R}{1-R^2}, \tag{4.61}$$

where R is the reflectivity. $\mathcal{F}_a$ has the effect of reducing the resolution as the input beam is offset.

To quantify the effects of the path length on $\mathcal{F}_a$, consider a monochromatic input, a delta function in frequency entering the FPS coaxial to the optic axis and having a beam radius a. The light entering the interferometer at $\rho = a$ will cause a shift in the transmitted output spectrum, since the optical path length of the cavity will be smaller by a factor of $\frac{\Delta(a)}{4}$ as given by Equation 4.54. The transmitted spectrum will be broadened due to the shifts in the optical path length. As a result, the wavelength input delta function will produce an output peak with a $\Delta\nu_m = \frac{\Delta(a)}{4}$. Moreover, a change of $\frac{\lambda}{4}$ is responsible for a change from one longitudinal mode to the next. We then get:

$$\mathcal{F}_a = \frac{\lambda r^3}{\rho^4 + 4\epsilon\,\rho^2 r} \tag{4.62}$$

Substituting Equations 4.61 and 4.62 into 4.60, with $\epsilon = 0$, one gets:

$$\mathcal{F}_t = \left[\left(\frac{1-R^2}{\pi R}\right)^2 + \left(\frac{\rho^4}{\lambda r^3}\right)^2\right]^{-\frac{1}{2}} \tag{4.63}$$

Equation 4.63 can be plotted using the same parameters as in Figure 15, as shown in Figure 16. From Equation 4.63, one can see that a maximum value for $\mathcal{F}_t$ is $\approx \frac{\pi}{2(1-R)}$, typically about 300 considering only reflection losses. The $\mathcal{F}_a$ contribution is only significant for ρ larger than $\sqrt[4]{\frac{2r^3\lambda(1-R)}{\pi}}$ or ≈400 µm, above which the finesse quickly degrades and $\Delta\nu_m \propto \rho^4$. Since the coupling lens at the entrance mirror on the FPS can produce a spot of less than 50 µm, it is expected that reflection losses and the overall alignment will be the critical factors for the interferometer's performance.

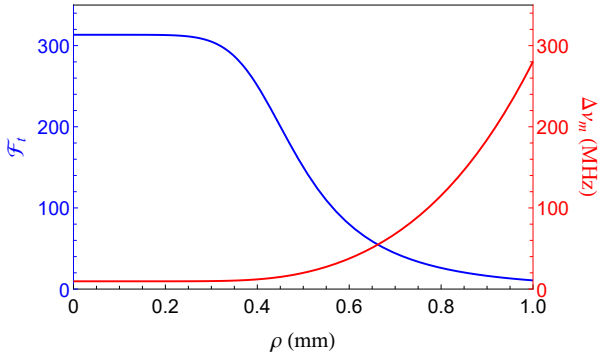

Figure 16 – Resolution in a confocal ($\epsilon = 0$) FPS. $\mathcal{F}_t$ (blue) and $\Delta\nu_m$ (red). In this simulation, λ=685 nm and r=25 mm, which are identical to the conditions of the performed experiments.

Looking at the minimum resolvable frequency $\Delta\nu_m$, it is then theoretically possible to resolve up to $\approx \frac{c(1-R)}{2\pi r}$ or ≈10 MHz in the interval for which the total finesse is around 300. From the results shown in Figures 15 and 16, keeping the FPS at the correct focal position helps to achieve a high finesse and operation at the zeroth order fringe.

Parameter	Value
Operating wavelength (λ)	685 nm
Cavity length and curvature radii (r)	25 mm
FSR	3 GHz
Reflectivity (R)	99.5%
Resonance linewidth	35 MHz
Resolving power ($\mathcal{R}$)	8×10^{-8}
Finesse ($\mathcal{F}$)	86

Table 3 – Experimental parameters for the FPS.

Once the FPS was aligned, it was used to calibrate the laser source for WGMs coupling taking into account the parameters summarized in Table 3. The FPS can be used in two basic configurations: i) scanning the cavity length by means of an attached piezo translator or ii) keeping the cavity at a constant length and scanning the light source frequency. The latter approach was used to calibrate our Tunable Diode Laser (TDL), since its wavelength can be modulated with an external electric signal, as will be described in the next section.

4.6 Calibrating a tunable diode laser

The “workhorse” laser for spectral characterization of WGM in our experiments is the New Focus 6300 series external-cavity TDL. It is a stable, narrow-linewidth source of tunable light. The working principle of such lasers is as shown in Figure 17. The laser cavity is formed by a high-reflection coating on one end of the laser diode and a high-reflecting tuning mirror on the other end. Starting from the diode, the beam passes through a collimating lens and then

strikes a diffraction grating at near grazing incidence. The beam is diffracted towards the tuning mirror which reflects the light ray back on itself. Part of the light from the diode is reflected by the grating, which forms the output beam.

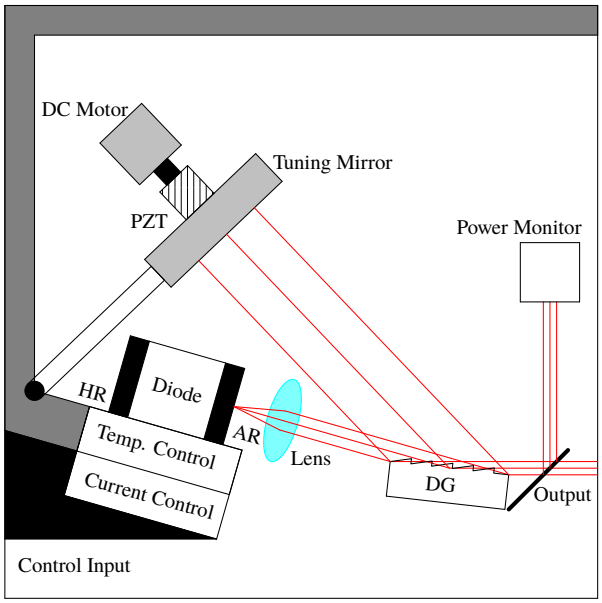

Figure 17 – New Focus TDL. AR: anti-reflection coating; DG: diffraction grating; HR: high-reflection coating.

The grating functions as a narrow spectral filter, only a few gigahertz wide. The high wavelength selectivity results because many lines of the grating are illuminated by the grazing-incidence beam and because the beam is diffracted by the grating twice in each round trip through the cavity. The grating spectral filter is narrow enough to force the laser to operate in a single longitudinal mode. Different wavelengths diffract off the grating at different angles. However, only one wavelength leaves the grating in a direction that is exactly perpendicular to the surface of the tuning mirror. This is the lasing wavelength, because it's the only one where photons will survive for many cavity round trips. It follows then, that one can tune the laser by changing the angle of the tuning mirror.

In order to avoid mode hops as we tune the laser, the number of waves in the cavity must be kept constant (even though the wavelength of the light in the cavity is changing). The number of waves in the cavity is maintained by having the tuning mirror rotate around a specific pivot point. The pivot point creates a relationship between the cavity length and the laser wavelength. The laser wavelength is set by the standard law for diffraction of light off a grating as follows:

$$\lambda = \Lambda \left(\sin \theta_i + \sin \theta_d\right) \tag{4.64}$$

where Λ is the spacing between grooves in the grating and θ_i and θ_d are the incident and diffracted angles. If L is the distance from the pivot point to the place where the beam strikes the grating, it can be shown that:

$$l_1 = L \sin \theta_i \tag{4.65}$$

$$l_2 = L \sin \theta_d \tag{4.66}$$

The total length of the cavity is given by:

$$D = l_1 + l_2 = L \left(\sin \theta_i + \sin \theta_d \right) \tag{4.67}$$

Dividing Equation 4.67 by Equation 4.64, one gets:

$$\frac{D}{\lambda} = \frac{L}{\Lambda} \tag{4.68}$$

Therefore, since θ_i and θ_d are constants, the total number of waves in the cavity is $\frac{L}{\Lambda}$ which is a constant (no mode hops). The TDL has a frequency modulation (FM) input for external analog control of the wavelength through the voltage applied to PZT on the tuning arm. Increasing voltage at the FM corresponds to a decrease in piezo voltage and an increase in laser frequency. In Figure 18 (left), the FM is swept from -1V to +1V while the TDL is directed to a wavemeter. A LabVIEW program collects the frequency values while the laser scans across the voltage range.

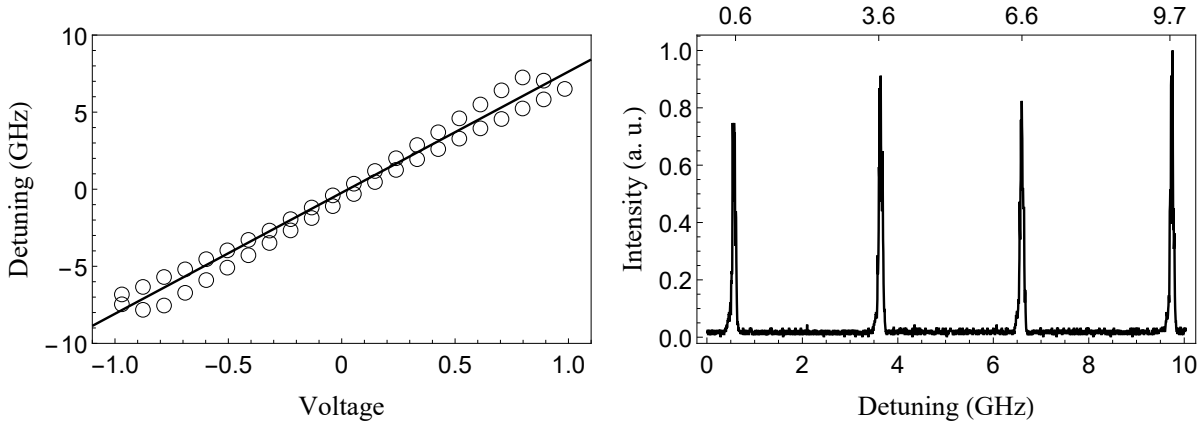

Figure 18 – (Left) FM at the TDL as measured by the wavemeter; (Right) Optical spectrum scanned with a FPS. The upper axis on the right graph represents the peaks' positions and thus the FSR spacing.

Figure 18 shows some hysteresis, which is typical for piezo driven systems. A calibration factor of (7.74 ± 0.10) GHz/V was observed for the red TDL scanning around 685 nm. With this calibration factor in mind, the laser was sent to a confocal Fabry-Perot interferometer as described in the previous section (cavity length 25 mm) so that a FSR of 3 GHz was expected (see Table 3).

Figure 18 (right) also shows the optical spectrum taking into account the calibration factor from Figure 18. No spurious peaks within the cavity FSR were observed, evidencing single longitudinal modes. Both calibration methods are then consistent, however, the calibration factor was smaller than the one given by the manufacturer (11.66 GHz/V). That can be a result

of communication issues between the DAQ board and the TDL driver. Nevertheless, since the FPS can act as a reference, the actual frequency range can always be monitored as the TDL is scanned, whithout the need of a wavemeter. After completing all the aforementioned control and calibration experiments, the TDL can finally be used to couple light into a glass microsphere.

4.7 Coupling light into a microsphere: selecting TE and TM modes

One of the first stages to identify resonances in a microsphere is to make sure that either the TE or the TM modes are being excited. The TE/TM polarization corresponds to the electric field perpendicular/parallel to the WGM plane [95]. In order to do so, a silica microsphere of diameter 100 µm was brought very close to the surface of the coupling prism. The relatively larger size was chosen in order to decrease the FSR so that a mode excitation is more likely. The focusing lens shown in Figure 7 was adjusted with a five-axis micropositioner (MDE277 - Elliot Scientific) in order to maximize the coupling efficiency.

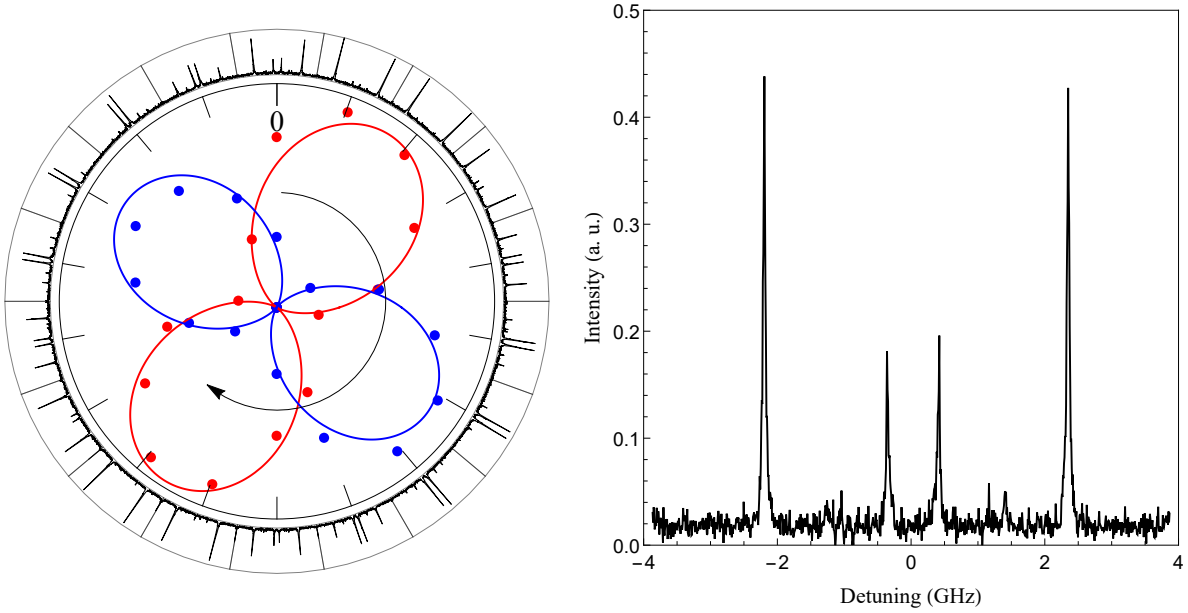

Figure 19 – Left: intensity of each resonance peak recorded as a function of the incident polarization angle. Outer ring: 18 spectra of the same pair of resonances recorded at 20° intervals, including a scan reversal. Red (blue) dots: Intensity of the first (second) peak. On the right graph, a single frequency scan in shown (including the scan reversal) for the spectrum shown at the position 0°.

Using a TDL set at 685 nm, WGMs of Q-factor of 10^6 were detected with a photomultiplier while a half-wave plate was set before the coupling fiber. Once a pair of resonances was found, a rotation of 180 degrees was given to the wave plate in increments of 10 degrees, thus introducing a complete revolution for the incident polarization. For each increment, the spectrum was recorded as well as that the intensity of each resonance peak. A fiber polarization controller was used to increase the extinction between the TE and TM modes.

As shown in Figure 19, the peaks' relative intensities are correlated. Once the first peak (represented by the red dots) reaches a maximum, the second peak is minimum. Both sets of points can be fitted as:

$$I = A \sin^2 (\phi + t) , \tag{4.69}$$

where I is the intensity and t the polar angle. A and ϕ are fitting coefficients. As given by Table 4, setting the wave plate to 17° maximizes the first peak, while setting it to 62° maximizes the second and the peaks are out of phase by a factor of $\frac{\pi}{2}$, as expected for TE/TM modes.

	A (a. u.)	ϕ (rad)	WP pos. (deg)
Peak 1	0.53±0.01	0.58±0.02	17±1
Peak 2	0.47±0.01	2.17±0.02	62±1

Table 4 – Fitting coefficients for a pair of TE/TM modes.

As for the A coefficient in Equation 4.69, the peak shown in red has a better coupling efficiency than the one in blue. This might be a result of coupling modes of different l, n numbers, so that within the same frequency range, the total energy is distributed unevenly. The next steps would be further optimizing the light coupling using a SNOM probe to scan the microsphere's surface for the spatial modes distribution. However, the overall coupling process for such microspheres turned out to be much more complicated than originally anticipated. Therefore, the light coupling procedure was limited to the basic TE/TM modes shown in Figure 19.

One of the main problems to achieve an efficient light coupling was controlling the focusing lens shown in Figure 7. The original positioner was made in a lathe machine in our mechanical workshop, however, it was not precise or mechanically stable enough to handle the fine tuning adjustments needed for efficient light coupling. The commercial piece had to be made-to-order and imported during the current COVID-19 pandemic, which significantly delayed the experiments. The lack of a working SNOM probe also contributed to a less than ideal coupling efficiency, since spatial modes distribution could not be optimized. Therefore, in order to proceed with the experimental results required for this work, the WGMs had to be put on hold so that the fluorescence spectroscopy experiments could be carried out. Those experiments will be the topic of the next chapters.

Considering the available TDL with a pump wavelength around 685 nm, a suited candidate for fluorescence spectroscopy are the Neodymium (Nd^{3+}) ions. In the next chapter, a nanothermometer based on single Nd^{3+}-doped Y_2O_3 nanoparticles is reported, followed by a similar system based on Erbium & Ytterbium co-doped yttria matrix, which is more adequate for infrared excitation.

5 NANOTHERMOMETRY WITH Nd^{3+}:Y_2O_3 NPs

A thermometer based on single Nd^{3+}:Y_2O_3 nanoparticles (NPs) is reported[1]. The nanothermometer relies on the ratio of the intensities of the light emitted due to transitions coming from thermally coupled energy levels accessible by either continuous-wave upconversion under 880 nm or downconversion under 532 nm excitation wavelengths. Both processes are modeled through rate equation systems based on multiphonon interactions between excited luminescent states, which led to excellent agreement with the experimental data. Moreover, the Nd^{3+}:Y_2O_3 effective phonon mode energy was determined, showing the appropriateness of the theoretical approach used. The system presented a relative sensitivity up to 1.36% at 300 K while working within the first biological window, thus particularly useful for biological sensing applications.

5.1 Rare-earth doped nanoparticles for temperature sensing

Rare-earth (RE) ions possess several characteristics that make them suitable for temperature sensing applications, such as the presence of thermally coupled emitting levels, high quantum yield, sharp emission lines and the possibility for energy down- and up-conversion [97]. Particularly for Nd^{3+}, it's possible to work within the first biological window, for both the excitation and fluorescence signals [98–101]. Moreover, the spectral separation between energy levels of Nd^{3+} is responsible for high thermal sensitivity (S_R>1% K^{-1} as defined below) at physiological temperatures, which meets the requirements for in vivo nanothermometry [102]. Once combined with a low maximum phonon energy matrix, such as yttria (dominant phonon mode energy: 380 cm^{-1} [103]) upconversion (UC) processes are particularly efficient [104, 105]. Apart from the low phonon energy, Y_2O_3 has an excellent chemical stability and high solubility for the RE ions [106], making it suited for sensing in catalytic environments [107]. A large number of synthesis methodologies of nano and microstructured Y_2O_3 particles have been reported, which show diverse parameters to control the particle's structure, size and morphology [108–110].

Several temperature dependent luminescence parameters can be used to measure local temperature, such as: emission intensity (or band shape), spectral line position, bandwidth, lifetime and polarization [58, 111, 112]. The Fluorescence Intensity Ratio (FIR) is a temperature determination technique based on the change in the relative intensities of two radiative transitions, generally from rare earth doped materials [113]. It has practical advantages over alternative thermometry techniques like fluorescence lifetime measurements, since, among other reasons, it is immune to pump light fluctuations and it can be done with continuous-wave (CW) excitation [114].

Particularly for single NPs, any temperature sensing technique sensitive to pump fluctuations becomes challenging from the experimental point of view. Normally, such NPs are

[1] Published in [96].

illuminated under tight focusing conditions and even a slight spatial deviation can affect the fluorescence signal. In this chapter, a nanothermometer based on single Nd^{3+}:Y_2O_3 NPs was characterized exploiting an UC as well as a downconversion (DC) excitation routes. The thermometer works due to the presence of thermally coupled states of Nd^{3+} accessible by a ladder-level phonon assisted process. The results were modeled following rate equation systems based on multiphonon interactions between luminescent states for each excitation routes investigated.

5.2 Nanoparticles synthesis and characterization

The synthesis was performed at the Chemistry Department of São Paulo state University (Universidade de São Paulo) by the reseach group lead by Professor Rogéria Rocha Gonçalves. For the sake of completeness, the route is described as follows. Nd^{3+}:Y_2O_3 NPs were prepared using homogeneous precipitation method followed by thermal annealing [115, 116]. Neodymium-doped $Y(OH)CO_3.nH_2O$ particles were firstly prepared as precursor via urea thermolysis by using $Y(NO_3)_3{\cdot}6H_2O$ (99.8% purity, Sigma-Aldrich) and urea (99–100% purity, Cinética). An aqueous solution of $Y(NO_3)_3$ and another of urea were mixed at room temperature so that the final concentrations were 0.01 and 2.00 mol L^{-1} respectively. The Nd^{3+} was introduced as ethanolic neodymium chloride solution, which was prepared from the respective oxide (99% purity, Sigma-Aldrich) by dissolution in aqueous hydrochloric acid solution, followed by careful drying at 80 °C with subsequent addition of anhydrous ethanol, to prepare the 0.10 mol L^{-1} concentration stock solution. The Nd^{3+} ions concentration was set to 1 mol% in relation to yttrium concentration. An increase in doping concentration increases the number of luminescence centers, however there's also a higher probability of energy transfers between Nd^{3+} ions, enhancing nonradiative processes. Therefore, the concentration was chosen in accordance to the optimum value reported in the literature [117]. The final solution was placed in an isothermal bath and maintained at 80 °C for 2 h in a closed flask. After a complete reaction, the precipitates were isolated by centrifugation, washed with distilled water and dried at 70 °C. Spherical Nd^{3+}:Y_2O_3 NPs were obtained after thermal annealing of [$Y(OH)CO_3.nH_2O$] under air during 2 h at 900 °C. This temperature was reached starting from room temperature and using a heating rate of 1 °C min^{-1}. This is important for eliminating carbonates and hydroxyls, minimizing residues in the final product.

Raman spectroscopy (LabRAM HR Horiba at 632.8 nm) was performed at the Chemistry Department of São Paulo state University (Universidade de São Paulo) in order to complement the structural analysis as well as to identify any secondary crystalline phases other than the cubic. As shown in Figure 20, scattering by phonons with a wavenumber of 377 cm^{-1} predominates. The assigned peaks shown in Table 5 are well-known in the literature for the cubic phase of Y_2O_3. Since it is difficult to perform absorption experiments in single NPs, a powder sample was used for performing diffuse reflectance measurements. The results show manifolds with partially resolved Stark levels, characteristic of crystalline samples, related to transitions from the Nd^{3+} ground state $^4I_{9/2}$ to excited states. Those results will be presented alongside the fluorescence

spectra.

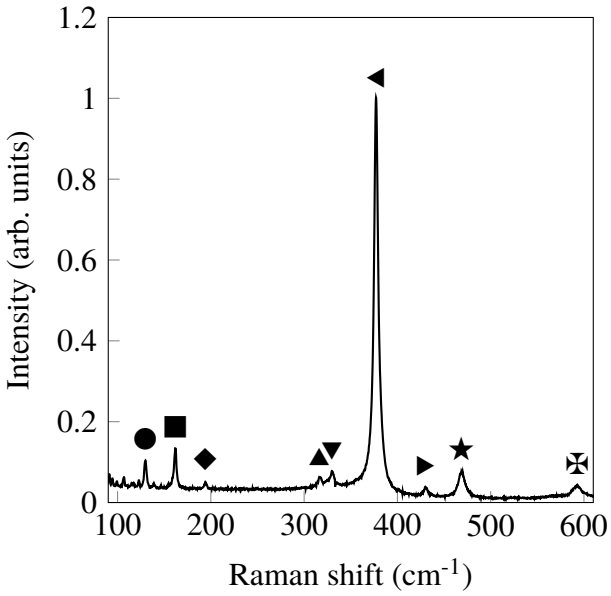

Figure 20 – Raman spectrum of of cubic Y_2O_3. The various symbols mark the positions of the Raman peaks, shown in detail in Table 5.

Mode	Wavenumber (cm^{-1})			
	This work	[118]	[119]	[120]
●	130	130	130	130
■	162	162	162	163
◆	194	194	192	195
▲	316	318	317	318
▼	330	330	328	331
◀	377	377	377	379
▶	430	430	429	432
★	469	†	469	471
✠	593	591	591	595

Table 5 – Phonon modes of cubic Y_2O_3. †: value not reported.

Transmission Electron Microscopy (TEM) images of the Nd^{3+}-doped Y_2O_3 polycrystalline NPs are illustrated in Figure 21 (a,b). Spherical monodisperse NPs were observed happening often as agglomerates and exhibiting a narrow size distribution, with a diameter of about 170 nm, which indicates the formation of polycrystalline NPs with average grain diameter about 30 nm. A preparation protocol was developed in order to separate those aggregates. An isopropanol suspension was put under an ultrasonic probe and a 10 µL aliquot was spin coated on a glass coverslip. Scanning Electron Microscopy (SEM) images for a typical sample can are shown in Figure 21 (c,d). In various areas on the coverslip, single NPs can be seen, all having similar sizes of about 170 nm laying on the coverslip micrometers away from each other. The sample

preparation protocol thus guarantees that there is a high probability that the NPs investigated under the microscope are indeed individual.

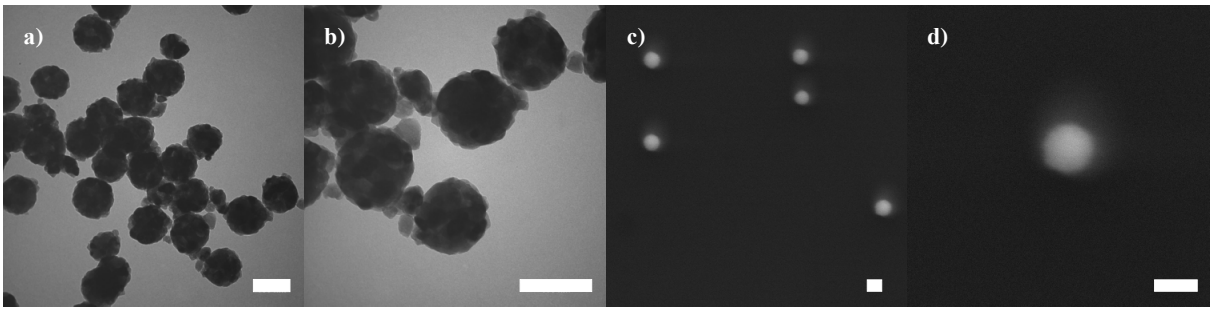

Figure 21 – a) and b): TEM characterization of samples. c) and d): SEM after spin coating. The white bars represent a length of 150 nm. Images a) and b) were done at the Chemistry Department of São Paulo state University (Universidade de São Paulo) while images c) and d) were done at the Physics Department of the Federal University of Pernambuco (Universidade Federal de Pernambuco).

5.3 Experimental setup

With confidence that the sample preparation protocol leads to the occurrence of single NPs within an area larger than the detectable spot under tight focusing conditions, it's possible to proceed with the optical spectroscopy characterization of such particles. The multiple thermally coupled Nd^{3+} levels are reached by both UC and DC processes observed with the aid of an inverted scanning optical microscope. A raster scan procedure was used to locate individual NPs while the focal spot of the excitation light is kept at a constant position. The single NPs temperature for both UC and DC nanothermometry approaches (sections 3.1 and 3.2, below) was set by a heating mantle embracing the microscope objective, ranging from 298 K to 347 K as measured at the sample's position by an IR camera (FLIR Systems-i5). During the pump power dependency tests, the NPs temperature was set to 298 K, while for the FIR measurements, a local temperature within the mentioned range was assigned to each fluorescence spectrum.

5.3.1 Upconversion

UC is a light-matter interaction phenomenon in which a longer wavelength light (typically in the infrared spectrum) is converted into radiation with a shorter wavelength through some atomic, ionic or molecular interaction. A multitude of UC processes has already been demonstrated in different matrices, involving one [121] or more [122] Nd^{3+} ions, using CW and pulsed excitation schemes [123].

For studying nanothermometry exploiting an UC excitation scheme, the experimental setup shown in Figure 22 was built. A CW Ti:Sapphire laser tuned to 880 nm was sent to

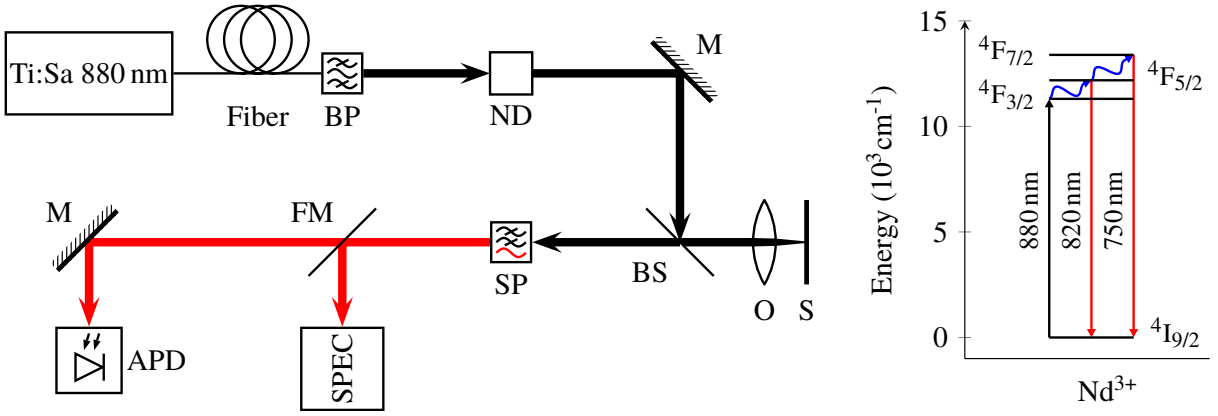

Figure 22 – Experimental setup for UC detection (left) and energy diagram for Y_2O_3:Nd^{3+} (right). BP: bandpass filter; ND: neutral density filters; M: mirror; BS: beamsplitter; O: objective; S: sample; SP: shortpass filter; FM: flip mirror; APD: avalanche photodiode. Blue arrows indicate the annihilation of phonons.

an inverted microscope by means of an optical fiber. In order to eliminate any spurious light generated along the fiber (*e.g.*, Stokes or anti-Stokes scattering), a "bandpass" filter composed of a shortpass (Thorlabs FESH0900) and a longpass (Thorlabs FEL0850) filters was mounted after the decoupling fiber objective. The laser is then directed to the microscope objective (NA=1.25), which focuses the excitation light at a diffraction limited spot at the sample, so that when a single NP is placed right at the focal point by a 3-axis piezo stage; the emitted fluorescence can be collected by the same objective and directed to either a spectrometer or an avalanche photodiode using a flip mirror. A shortpass spectral filter (Thorlabs FESH0850) is used to filter out residual pump laser light from the UC fluorescence. The beamsplitter BS could incorporate the shortpass function if replaced by a dichroic mirror, but that would make the apparatus less versatile in terms of pump laser wavelength as well as the collected signal. Therefore, in order to find a good compromise between losses and versatility, a beamsplitter and a good shortpass is a suitable option.

The energy diagram for the UC processes is also shown in Figure 22. By means of phonon annihilation in the lattice, electrons can be promoted from the $^4F_{3/2}$ to the $^4F_{5/2}$ state, distant about 900 cm^{-1}. An additional phonon-assisted promotion can happen from $^4F_{5/2}$ to $^4F_{7/2}$, further 1200 cm^{-1} away [124]. Once the APD detected the UC signal from a NP, the Ti:Sapphire laser was fine tuned around 880 nm in order to optimize the counts coming from both UC processes. Then, fluorescence spectra were recorded for a range of pump powers.

For the first UC process, shown in Figure 23(a,b), a signal intensity linearly dependent on the pump power (exponent (1.0 ± 0.1)) was observed for all the five major peaks within the transition and for the total counts (integrated from 800 nm to 850 nm), meaning that only one photon of the pump laser was needed to produce a photon of the UC light and these are phonon-assisted UC emission lines. For the experiments in this chapter, all pump power values reported were measured right after the objective *O* as shown in Figure 22. The fluorescence

spectrum on Figure 4(a) matches the dips at the diffuse reflectance [125] shown in the same graph, indicating that those are indeed sub-levels for the $^4F_{5/2} \rightarrow {}^4I_{9/2}$ transition. The slight discrepancy between those spectra can be attributed to different calibration factors between the equipment.

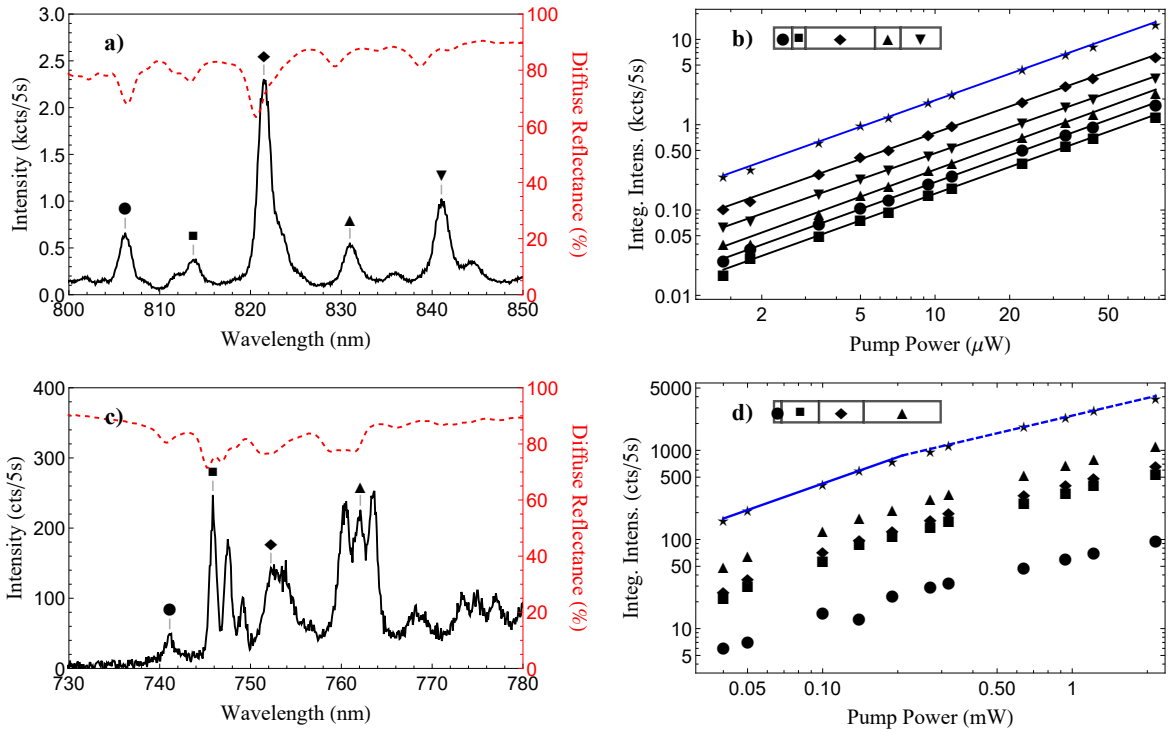

Figure 23 – Fluorescence (black lines) and diffuse reflectance spectra (red lines) for $^4F_{5/2} \rightarrow {}^4I_{9/2}$ (a) and $^4F_{7/2} \rightarrow {}^4I_{9/2}$ (c) transitions. b) and d): respective linear dependencies on pump power. The total counts for each transition is represented by a $\star$. The horizontal bar on b) [d)] represents the percent contribution of each Stark sublevel of the $^4F_{5/2}$ ($^4F_{7/2}$) manifold on the total counts. On b) and d), the solid blue line has an apparent slope of (1.0 ± 0.1) while the dashed one on d) has a slope of (0.7 ± 0.1).

By increasing the pump power to a range of hundreds of microwatts up to 2 mW, the second UC process $^4F_{7/2} \rightarrow {}^4I_{9/2}$ becomes detectable. Again, the fluorescence spectrum matched the features seen in diffuse reflectance measurements. The higher pump power required is due to the larger energy separation between the two upper detected levels, so that a second phonon-assisted promotion requires a higher population at the $^4F_{5/2}$ state. As shown in Figure 23(d), the pump power dependence of the fluorescence resulting from the decay $^4F_{7/2} \rightarrow {}^4I_{9/2}$ is no longer linear. Instead, a sublinear (approximately 0.7) power dependence is observed for a pump power above 500 μW which goes to the unity for lower pump powers. Such sublinear power dependence is not relevant for the present nanothermometry experiments, since these are carried out at a constant low power in the range of tens of μW.

A disadvantage of this UC excitation scheme is that the $^4F_{3/2} \rightarrow {}^4I_{9/2}$ transition becomes inaccessible since it coincides with the pump wavelength. In order to study this transition, one can exploit a DC route. Here the versatility of the inverted microscope plays an important role and the experimental setup can be easily adapted for this new configuration.

5.3.2 Downconversion

DC is an energy conversion process inverse from UC. Here, light of a shorter wavelength is converted into radiation with a longer wavelength. Using the same basic setup as in the previous experiment, a 532 nm CW laser was sent through the inverted microscope, as shown in Figure 24. This time, however, the spectral filter (LP) was chosen as a combination of a FEL0550 (Thorlabs) and a notch filter. From that configuration, it is possible to observe a DC signal from the $^4F_{5/2} \rightarrow {}^4I_{9/2}$ transition as well as $^4F_{3/2} \rightarrow {}^4I_{9/2}$.

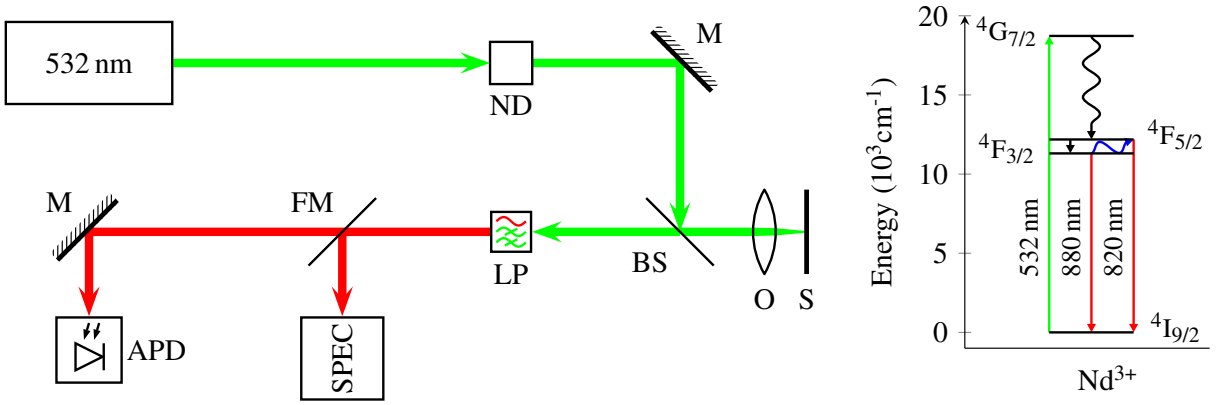

Figure 24 – Experimental setup for DC detection (left) and energy diagram for Y_2O_3:Nd^{3+} (right). ND: neutral density filters; M: mirror; BS: beamsplitter; O: objective; S: sample; LP: longpass filter; FM: flip mirror; APD: avalanche photodiode. Blue arrows indicate the annihilation of phonons. Black arrows indicate non-radiative decays.

For the $^4F_{3/2} \rightarrow {}^4I_{9/2}$ transition, that was used in the previous experiment as excitation path, the fluorescence spectrum and power dependence are shown in Figure 25(a,b). In this case, there are peaks resolved for that transition that are not present in the diffuse reflectance, since they lie outside of the spectrophotometer's range 360 nm to 740 nm (Minolta CM2600-D). That can be understood as a result of the $^4F_{3/2} \rightarrow {}^4I_{9/2}$ manifolds [126, 127].

Again, a linear power dependence of (1.0 ± 0.1) was observed for all sublevels as well as for the entire transition (integrating from 870 nm to 940 nm). For the $^4F_{5/2} \rightarrow {}^4I_{9/2}$ transition, a similar behaviour was observed, as shown in Figure 25(c,d). That transition shows the same features as the one in Figure 23(a), although it is reached by a distinct single-photon process.

Now that three important transitions for the Nd^{3+} have been characterized, two pairs of transitions can be studied for their thermometric capabilities. The first pair comes from the UC experiment, $^4F_{5/2} \rightarrow {}^4I_{9/2}$ and $^4F_{7/2} \rightarrow {}^4I_{9/2}$ while the second pair comes from the DC one, $^4F_{3/2} \rightarrow {}^4I_{9/2}$ and $^4F_{5/2} \rightarrow {}^4I_{9/2}$. The best suited nanothermometry technique for both cases is the so called Fluoresce Intensity Ratio (FIR).

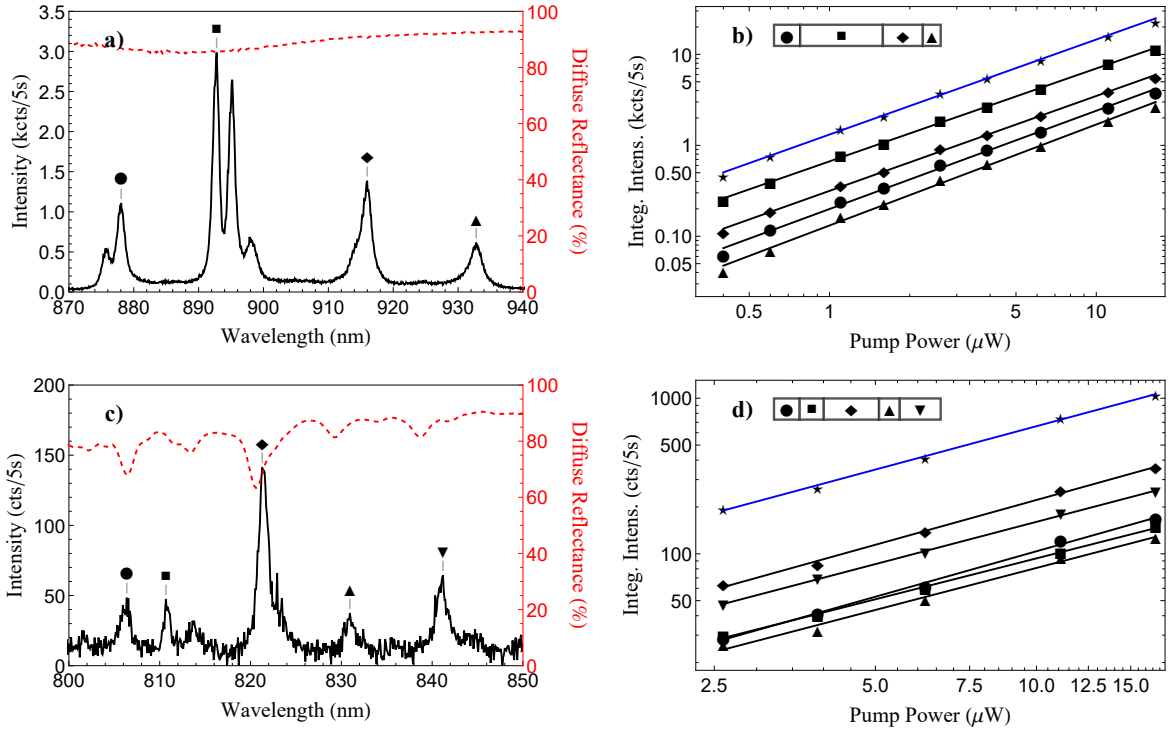

Figure 25 – Fluorescence (black lines) and diffuse reflectance (red lines) spectra for $^4F_{3/2} \rightarrow {}^4I_{9/2}$ (a) and $^4F_{5/2} \rightarrow {}^4I_{9/2}$ (c) transitions. b) and d): respective linear dependencies on pump power. The total counts for each transition is represented by a $\star$. The horizontal bar on b) [d)] represents the percent contribution of each Stark sublevel of the $^4F_{3/2}$ ($^4F_{5/2}$) manifold on the total counts. On b) and d) the solid blue lines represent the best apparent linear fit, with a slope of (1.0 ± 0.1).

5.4 FIR thermometry

Starting from the DC experiment, the proximity between the electronic levels $^4F_{3/2}$ (E_1) and $^4F_{5/2}$ (E_2) allows the upper level to be populated from the lower by thermal redistribution. The relative population between the two emitting levels, R, follows a Boltzmann-type population distribution given by [77]:

$$R = \frac{I_{20}}{I_{10}} = \frac{\gamma_{20} g_2 h\nu_2}{\gamma_{10} g_1 h\nu_1} \exp\left(\frac{-E_{21}}{k_B T}\right) = A \exp\left(\frac{-E_{21}}{kT}\right) \tag{5.1}$$

where k_B is the Boltzmann's constant, E_{21} is the energy gap between these two excited levels, g_2 and g_1 are the degeneracies $(2J + 1)$ of the levels and γ_{20} and γ_{10} are the spontaneous emission rates of the E_2 and E_1 levels to the E_0 level, respectively. Equation 5.1 can be written as:

$$\ln(R) = \beta - \frac{\alpha}{T} \tag{5.2}$$

where $\beta = \ln(A)$ and $\alpha = \left(\frac{E_{21}}{k}\right)$. β is an adimensional parameter that takes into account the ratios between the lifetimes and energies of each coupled levels, while α has dimension of temperature

and gives the apparent or effective energy separation measured for the FIR. For a FIR-based sensor, the sensitivity is the rate of change of the intensity ratio with the temperature [128]:

$$S = \frac{dR}{dT} = R\frac{\alpha}{T^2} \tag{5.3}$$

However, a relative sensitivity S_R is often used in order to analyze the sensing performance of various host materials [77]:

$$S_R = \frac{S}{R} = \frac{\alpha}{T^2} \tag{5.4}$$

Since the FIR technique only takes into account the relative intensities of two thermally coupled transitions, systematic fluctuations in intensity should not affect the data acquisition and the accuracy of the experimental results. For instance, single NPs are prone to migrate from the focal position, particularly once the substrate is heated, thus affecting the absolute counts at a given time. However, as long as the temperature is kept constant and both transitions are recorded simultaneously, the relative ratio can still be used as a reliable measurement strategy for such thermometer.

Thus, plotting the logarithm of the relative intensities between the $^4F_{3/2}$ and $^4F_{5/2}$ transitions versus the inverse of the temperature at which the emission spectra were taken, one should obtain a straight line, as given by Equation 5.2. FIR measurements under 532 nm pump were taken from the ratio between each one of the five most intense peaks in Figure 25(c) and the first peak shown in Figure 25(a), around 880 nm.

Due to the spectrometer's diffraction grating used, only about 90 nm can be recorded in a single snapshot. One finds that the first sublevel of $^4F_{3/2} \rightarrow {}^4I_{9/2}$, represented by a ● in Figure 25(a), accounts for about 16% of the whole transition luminescence. Figure 26(b) shows a linear behavior as expected. Taking the $^4F_{5/2} \rightarrow {}^4I_{9/2}$ transition as a whole, one finds $\beta = (2.53 \pm 0.08)$ and $\alpha = (1134 \pm 25)$ K, thus $S_R = (1.26 \pm 0.03)$ % at 300 K. It's possible to apply the same procedure to the UC process, as shown in Figure 26(c,d). This time, however, the first peak of the $^4F_{5/2} \rightarrow {}^4I_{9/2}$ transition, represented by a ● in Figure 23(a) only accounts for 11% of the total counts. One finds $\beta = (2.41 \pm 0.23)$ and $\alpha = (1228 \pm 75)$ K, thus $S_R = (1.36 \pm 0.08)$ % at 300 K. This higher sensitivity is to be expected, since for the FIR measurements using an UC excitation scheme the energy separation between the thermally coupled levels is larger than the one for the DC process.

The host matrix, Y_2O_3, is known for being able to resolve the fine Stark structure of Nd^{3+} transitions. That allows the so called single-band nanothermometry, where FIR measurements are made within the manifolds of a single energy level [129]. However, that often generates small sensitivities (S_R<1% K^{-1}). For instance, [97] reported a maximum of S_R=0.34% for single-band nanothermometry between $^4F_{3/2(2)} \rightarrow {}^4I_{9/2(2)}$ and $^4F_{3/2(1)} \rightarrow {}^4I_{9/2(5)}$ transitions, while [58] reported up to S_R=1.51% for a FIR between $^4F_{5/2} \rightarrow {}^4I_{9/2}$ and $^4F_{3/2} \rightarrow {}^4I_{9/2}$ transitions. Both papers work

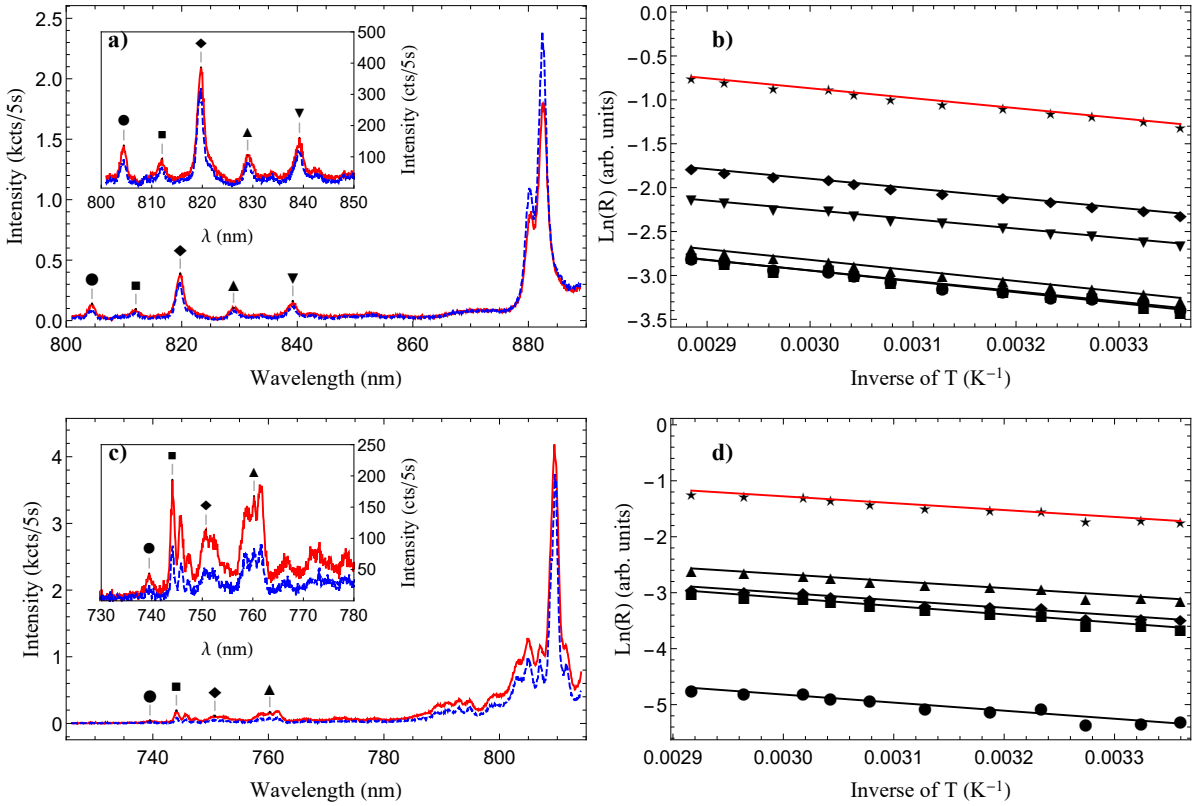

Figure 26 – FIR measurements in the DC (a,b) and UC (c,d) excitation schemes. The blue dashed (red solid) spectra were taken at 298 K (347 K). The inset in a)(c)) shows a closer view of the $^4F_{5/2}(^4F_{7/2})$ sublevels increasing in intensity as the temperature rises. On b)[d)], the ratio of the total counts for the transition $^4F_{5/2}(^4F_{7/2})$ is represented by a ★.

with Y_2O_3 nanopowders, albeit not in the single NP level. The highest value for S_R found in the literature is 1.59% between $^4F_{5/2}\rightarrow{}^4I_{9/2}$ and $^4F_{3/2}\rightarrow{}^4I_{9/2}$ transitions reported by [130]. Such high sensitivity implies a value for ΔE_{eff} (given by the FIR measurements) very close to or even higher than ΔE_{real} (given by the actual spectral separation between the energy levels), as is also the case for Yb^{3+}/Er^{3+} codoped yttria NPs [131–133]. Equation 5.21 also admits those solutions for certain values of q_i and $\hbar\omega$, so one possible explanation for higher sensitivities are different contributions for the lower energy phonons in the density of states. Further experiments with Yb^{3+}/Er^{3+} codoped yttria NPs can be performed in order to investigate such possibility.

Besides S_R, temperature accuracy δT is another parameter to characterize the optical thermometer. It gives the uncertainty of a temperature measurement as a result of the smallest area increment that can be measured by FIR. δT is given by [134]:

$$\delta T = \frac{\delta R}{S_R R}, \tag{5.5}$$

where $\frac{\delta R}{R}$ is the relative error of R, whose value is 0.14%. The value of $\delta FIR/FIR$ was determined by sampling the data at different rates and then comparing the integrals to estimate the error.

Therefore, $\delta T \approx 0.1$ K for both configurations, which is typical for Nd^{3+}-based sensors [77, 135]. The two FIR measurements show different behaviors in what concerns temperature changes. The DC shows an anticorrelation between the thermally coupled levels due to the thermal redistribution from the lower to the upper state. On the other hand, on the UC process, both thermally coupled transitions increase in counts, since they are both phonon populated from a lower energy level. However, since there is still thermal redistribution, the relative intensities allow a FIR measurement with good agreement with Boltzmann's distribution for that range of temperatures. The anticorrelation is not a prerequisite for a high sensitivity as the latter is more dependent on the effective energy gap between the coupled levels, as will be demonstrated in the modeling section, which consists of a rate equation analysis of the UC experiment, since it involves all the four relevant energy levels, including the ground state.

5.5 Rate equation analysis

We are interested in finding the population densities for two thermally coupled states of Nd^{3+} accessible by a ladder-level assisted thermal coupling process [136]. Henceforth, for the sake of simplicity, the population densities (n_i; i=0,1,2,3) are associated to the states $|0\rangle$ ($^4I_{9/2}$), $|1\rangle$ ($^4F_{3/2}$), $|2\rangle$ ($^4F_{5/2}$), $|3\rangle$ ($^4F_{7/2}$). A rate equation system for the population densities can be written as [137, 138]:

$$\frac{dn_0}{dt} = -\sigma_0 \Phi n_0 + \gamma_1(T)\, n_1 + \gamma_2(T)\, n_2 + \gamma_3(T)\, n_3 \tag{5.6}$$

$$\frac{dn_1}{dt} = \sigma_0 \Phi n_0 - \left[\Lambda_{12}(T) + \gamma_1(T)\right] n_1 \tag{5.7}$$

$$\frac{dn_2}{dt} = \Lambda_{12}(T)\, n_1 - \left[\Lambda_{23}(T) + \gamma_2(T)\right] n_2 \tag{5.8}$$

$$\frac{dn_3}{dt} = \Lambda_{23}(T)\, n_2 - \gamma_3(T)\, n_3 \tag{5.9}$$

where Φ is the photon flux and σ_0 is the absorption cross section corresponding to the $|0\rangle \rightarrow |1\rangle$ transition. The multiphonon excitation rates are given by $\Lambda_{ij} = C_{ij}^{ep} P_{ij}(T)$, where C_{ij}^{ep} is a parameter proportional to the electron–phonon coupling strength and $P_{ij}(T)$ are the phonon occupancy numbers given by [137, 139]:

$$P_{ij}(T) = \left[\exp\left(\frac{\hbar\omega}{kT}\right) - 1\right]^{-q_{ij}} \tag{5.10}$$

where q_{ij} is the number of effective phonons with energy $\hbar\omega$ involved in the multiphonon excitation from level i to level j, k is the Boltzmann's constant, and T is sample's absolute temperature. The population relaxation rates are given by [140]:

$$\gamma_i(T) = \gamma_i^{rad} + W_i^{NR}(T) \tag{5.11}$$

with $\left(\gamma_i^{rad}\right)^{-1}$ being the radiative decay time. $W_i^{NR}(T)$ is the nonradiative relaxation rate from level i due to multiphonon relaxation processes. Choosing a reference temperature T_0, $W_i^{NR}(T)$ can be written as [138, 141]:

$$W_i^{NR}(T) = W_i^{NR}(T_0)\left[\frac{1-\exp\left(-\frac{\hbar\omega}{kT}\right)}{1-\exp\left(-\frac{\hbar\omega}{kT_0}\right)}\right]^{-q_i}, \tag{5.12}$$

where q_i represents the number of effective phonons involved in the relaxation of level i to the closest low energy level. The steady-state populations for levels $i = 1, 2, 3$ are given by:

$$n_1(T) = \frac{\sigma_0 \Phi n_0}{\Lambda_{12}(T) + \gamma_1(T)} \tag{5.13}$$

$$n_2(T) = \frac{\Lambda_{12}(T)\,\sigma_0 \Phi n_0}{\left[\Lambda_{12}(T) + \gamma_1(T)\right]\left[\Lambda_{23}(T) + \gamma_2(T)\right]} \tag{5.14}$$

$$n_3(T) = \frac{\Lambda_{23}(T)\,\Lambda_{12}(T)\,\sigma_0 \Phi n_0}{\gamma_3(T)\left[\Lambda_{12}(T) + \gamma_1(T)\right]\left[\Lambda_{23}(T) + \gamma_2(T)\right]} \tag{5.15}$$

From either Equations 5.6–5.9 or 5.13–5.15, one gets:

$$\frac{n_3}{n_2} = \frac{C_{23}^{ep}\left[\exp\left(\frac{\hbar\omega}{kT}\right)-1\right]^{-q_{23}}}{\gamma_3^{rad} + W_3^{NR}(T_0)\left[\frac{1-\exp\left(-\frac{\hbar\omega}{kT}\right)}{1-\exp\left(-\frac{\hbar\omega}{kT_0}\right)}\right]^{-q_3}} \approx \frac{C_{23}^{ep}\left[\exp\left(\frac{\hbar\omega}{kT}\right)-1\right]^{-q_{23}}}{W_3^{NR}(T_0)\left[\frac{1-\exp\left(-\frac{\hbar\omega}{kT}\right)}{1-\exp\left(-\frac{\hbar\omega}{kT_0}\right)}\right]^{-q_3}}, \tag{5.16}$$

since the typical values for $W_i^{NR}(T_0)$ are about 10^3 larger than γ_i^{rad} for the relevant Nd^{3+} levels, determined through the energy-gap law [142, 143]. This offers a good approximation for a small temperature variation, which is the case of the present work. Similarly:

$$\begin{aligned}\frac{n_2}{n_1} &\approx \frac{C_{12}^{ep}\left[\exp\left(\frac{\hbar\omega}{kT}\right)-1\right]^{-q_{12}}}{C_{23}^{ep}\left[\exp\left(\frac{\hbar\omega}{kT}\right)-1\right]^{-q_{23}} + W_2^{NR}(T_0)\left[\frac{1-\exp\left(-\frac{\hbar\omega}{kT}\right)}{1-\exp\left(-\frac{\hbar\omega}{kT_0}\right)}\right]^{-q_2}} \\ &\approx \frac{C_{12}^{ep}\left[\exp\left(\frac{\hbar\omega}{kT}\right)-1\right]^{-q_{12}}}{W_2^{NR}(T_0)\left[\frac{1-\exp\left(-\frac{\hbar\omega}{kT}\right)}{1-\exp\left(-\frac{\hbar\omega}{kT_0}\right)}\right]^{-q_2}},\end{aligned} \tag{5.17}$$

since at a low pump power regime (below 500 µW), one could assume that the nonradiative emission rate contribution is much larger than the electron–phonon coupling strength to $|3\rangle$, which is reasonable for oxide hosts [144]. Taking a natural logarithm on both sides of Equations 5.16 and 5.17 and after a series expansion up to the first order around $T = T_0$, one gets:

$$\ln\left(\frac{I_j}{I_i}\right) \approx \beta - \frac{\Delta E_{eff}^{ij}}{kT}, \tag{5.18}$$

where:

$$\Delta E_{eff}^{ij} = \hbar\omega \left[\frac{\exp\left(\frac{\hbar\omega}{kT_0}\right) q_{ij} - q_i}{\exp\left(\frac{\hbar\omega}{kT_0}\right) - 1}\right] \tag{5.19}$$

ΔE_{eff}^{ij} represents the effective energy separation of the emission levels as a result of the multi-phonon processes [145]. Equation 5.19 relates ΔE_{eff}^{ij}, as given by the FIR measurements and three other relevant parameters: the effective phonon energy ($\hbar\omega$) and the number of phonons associated with excitation (q_{ij}) and relaxation for the lower energy level (q_i). Assuming that the real energy separation between $|i\rangle$ and $|j\rangle$ is given by:

$$\Delta E_{real}^{ij} = q_{ij}\hbar\omega \tag{5.20}$$

Equation 5.19 can be written as:

$$\Delta E_{eff}^{ij} = \left[\frac{\exp\left(\frac{\hbar\omega}{kT_0}\right) \Delta E_{real}^{ij} - q_i\hbar\omega}{\exp\left(\frac{\hbar\omega}{kT_0}\right) - 1}\right] \tag{5.21}$$

Taking into account the constraint that $\hbar\omega$ has the same value for both UC and DC excitation schemes, Equation 5.21 can be solved for both processes. The solution will be a set of (q_1, q_2) points associated with a number of phonons of energy $\hbar\omega$, as shown in Figure 27. Both processes can thus be used in conjunction to obtain the best fitting parameters, which consist of the first real solution of Equation 5.21. Also shown in Figure 27 is the fitting of the FIR measurements with the rate equation model. A good agreement between a least squares fit for the FIR and the solution of Equation 5.21 was found, particularly for the DC process. Following the same equation, it's expected that ΔE_{eff}^{ij} to be smaller than ΔE_{real}^{ij}, as it's often the case for FIR measurements. From the theoretical model, this is primarily a result of phonons involved in the relaxation rates, as given by Equation 5.12.

Table 6 – Fitting parameters for both phonon-assisted processes. Kets $|i\rangle$ and $|j\rangle$ are coupled energy levels for each MP process. ΔE_{eff}^{ij} was calculated from Equation 5.21 using the best fitting parameters.

Process	Pump λ (nm)	$\|i\rangle$,$\|j\rangle$	ΔE_{real}^{ij} (cm^{-1})	ΔE_{eff}^{ij} (cm^{-1})	q_{ij}	q_i	$\hbar\omega$ (cm^{-1})
DC	532	$^4F_{3/2}$, $^4F_{5/2}$	880	808	3	4	300
UC	880	$^4F_{5/2}$, $^4F_{7/2}$	1141	924	4	7	300

As shown in Table 6, the most energetic phonons available in the matrix do not dominate the multiphonon absorption processes, since $\hbar\omega$ was found to be smaller than the cut-off value

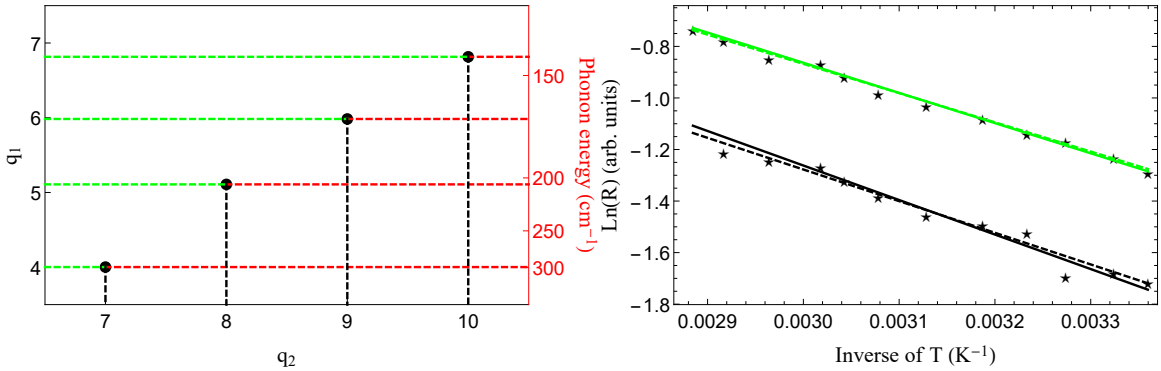

Figure 27 – Rate equation modeling for both DC and UC processes. On the left, the pairs of (q_1, q_2) points and their corresponding $\hbar\omega$ values. On the right, the green (black) curve shows the fitting for the DC (UC) process. The solid line is the the rate equation model while the dashed one is a least squares fit for the FIR.

(380 cm^{-1}). This corroborates results and discussions presented, for example, in [137, 138]. That can be understood as a result of cooperative effects of the multiple (q_1, q_2) solutions in the phonon density of states. For the UC process, a larger number of phonons q_{ij} is required to overcome the energy separation when compared to the DC process. Moreover, the former also shows a larger value for q_i than the latter. That can be a result of relaxations between the manifolds of the Stark components, effectively skewing the phonon distribution density of states. The rate equation analysis can also be applied to explain the sublinear power dependence shown in Figure 23 [109]. One possibility is to introduce a pump excited-state absorption term in the rate equations. Further analysis can be done to verify such mechanism so that the model can be corrected for a higher pump power regime.

In conclusion, a Nd^{3+}-based nanothermometer was characterized by FIR for both UC and DC configurations. A rate equation model was derived for the multiphonon assisted processes in good agreement with the experimental results for a low pump power (below 500 µW) and small temperature range (up to 347 K). Those limits are adequate for biological applications, specially considering the UC process, which operates entirely within the first biological window. To the best of our knowledge, this is the first report of such system in the single NP level to provide an extensive rate equation model for the multiphonon processes. One of the outputs of the model is the determination of yttria's effective phonon mode energy, 300 cm^{-1}. This kind of analysis can be transposed to other pumping wavelengths, thus allowing for other electronic transitions to be explored for nanothermometry.

Although the experiments were conducted under infrared and green laser pump, a direct excitation at the $^4F_{9/2}$ energy level is also possible, which translates to a laser pump of 689 nm [146]. Therefore, such approach is of special interest for WGMs spectroscopy to be performed in the setup described in the previous chapter. On the other hand, other pump configurations can also be explored, such as an Erbium & Ytterbium co-doped yttria matrix, which will be topic of the next chapter.

6 NANOTHERMOMETRY WITH Er^{3+},Yb^{3+}:Y_2O_3 NPs

In this chapter, Er^{3+}, Yb^{3+} codoped yttria NPs were characterized for the first time as a thermometric probe at the single nanocrystal level using the Fluorescence Intensity Ratio technique[1]. The nanothermometer characterization was performed by exciting the single nanoparticles with a low power, continuous-wave laser emitting at 980 nm, within one of the biological windows. The nanothermometer showed a relative sensitivity of 1.31% and an accuracy of 0.1 K at 300 K. The results were described by a rate equation analysis using a dual effective phonon model which reproduced the expected phonon energy of the host matrix.

6.1 Er^{3+},Yb^{3+} codoped nanoparticles for temperature sensing

As discussed in the previous chapter, UC is a light-matter interaction phenomenon in which a longer wavelength light (typically in the infrared part of the eletromagnetic spectrum) is converted into radiation with a shorter wavelength through some atomic, ionic or molecular interaction. Excitation in the infrared region is particularly advantageous for biological applications because radiation in this spectral range penetrates deeply in biological structures, induces weak autoluminescence background and avoids photodegradation [148]. Depending on the nature of the interaction behind the UC process, both the excitation and the collected signal can lie within one of the so-called biological windows, thus minimizing losses [149] and heating. FIR measurements can be made through UC processes [150], which are particularly efficient for RE ions inside a matrix with a low maximum phonon energy, such as yttria (dominant phonon energy: 380 cm^{-1}) [103–105, 151]. Moreover, Y_2O_3 has excellent chemical stability and high solubility for the RE ions [106]. A large number of synthesis methodologies of nano and microstructured Y_2O_3 particles have been reported, which show diverse parameters to control the particle's structure, size and morphology [108–110].

Among the dopant ions in RE-based thermometers, erbium ions (Er^{3+}) are a very convenient choice due to the possibility of optical excitation in the near infrared [152]. These ions present two green luminescence bands originating from two thermally coupled electronic energy levels, $^2H_{11/2}$ and $^4S_{3/2}$. That is, the relative intensity of the luminescence originating from these levels is temperature-dependent. This effect is due to the Boltzmann equilibrium in between the populations of the excited states and it allows the use of the FIR technique to produce primary thermometers [153]. Codoping the samples with sensitizer ions presenting a very high absorption cross section at the chosen excitation wavelength, as it is the case of ytterbium (Yb^{3+}), is an important strategy for increasing the performance of different luminescent materials [154]. The relatively high absorption cross-section of Yb^{3+} ions around 980 nm when compared with the

[1] Published in [147].

Er^{3+} ions allows for CW excitation, which present lower intensities as compared to the peak intensities of pulsed lasers [155].

Keeping in mind the potential applications for WGMs spectroscopy, the Er^{3+}/Yb^{3+}:Y_2O_3 system was also chosen due to the possibility of excitation under 980 nm, which matches one of the available TDL's wavelength. Therefore, the results can be compared with the previous system (based on Nd^{3+}) and the best configuration among the available ions and excitation schemes can be chosen. This chapter reports the results of individual cubic-phase Y_2O_3 NPs codoped with Er^{3+} and Yb^{3+} used as nanothermometers at the single particle level. The results are then modeled by a rate equation analysis which takes into account the multiphonon assisted processes behind the thermally coupled luminescent energy levels, shedding light into the properties of the host matrix vibrational normal modes.

6.2 Nanoparticles synthesis and characterization

As was the case for the NPs studied in Chapter 5, the synthesis was carried out at the Chemistry Department of São Paulo state University (Universidade de São Paulo) and is reproduced as follows. Undoped Y_2O_3 and Er^{3+}, Yb^{3+} codoped Y_2O_3 NPs were prepared via homogeneous precipitation synthesis followed by further thermal treatment [156]. Homogeneous and fully redispersable spherical hydroxycarbonate nanoparticles, [$Y(OH)CO_3.nH_2O$], were firstly obtained by urea thermolysis using urea (99-100% purity, Synth) and yttrium nitrate ($Y(NO_3)_3.6H_2O$ 99.8% purity, Sigma Aldrich). For the herein studied Er^{3+}/Yb^{3+} codoped samples, erbium and ytterbium nitrate solutions were used as dopant precursors and prepared from the respective oxides (99% purity, Sigma-Aldrich) by their dissolution in 0.10 $mol.L^{-1}$ nitric acid aqueous solution. Initially, urea was dissolved in a mixed Ln^{3+} (Ln^{3+}=Y^{3+}, Er^{3+}, Yb^{3+}) aqueous nitrate final solution making a total solution volume of 252 mL. The final concentrations of yttrium and urea were 0.01 and 5.00 $mol.L^{-1}$, respectively. The concentrations of Er^{3+} and Yb^{3+} ions were 0.5 and 1.5 mol% in relation to Y^{3+} ions, which is adequate to avoid concentration quenching accordingly to the literature [131].

The final solution was heated at 80 °C for 2 h in a closed flask. After a complete reaction, the final suspension was then cooled to ambient conditions and the colloidal particles were isolated by centrifugation. The wet product [$Y(OH)CO_3.nH_2O$] was washed five times with distilled water and dried at 70 °C for 6 h to yield a white powder. The 0.5% Er^{3+}/1.5% Yb^{3+}:Y_2O_3 (henceforth referred to as Er^{3+}/Yb^{3+}: Y_2O_3) nanoparticles were obtained after a calcination of [$Y(OH)CO_3.nH_2O$] under air during 2 h at 900 °C, which was reached using a heating rate of 5 °C min^{-1}. Homogeneous and well dispersed spherical Er^{3+}/Yb^{3+}:Y_2O_3 codoped NPs were successfully prepared by homogeneous precipitation method followed by post-thermal treatment [116, 157]. As described in a previous work [125], the adopted reactional and post-reactional conditions allow the formation of pure body-centered cubic structure of Y_2O_3, with Ia_3 space

group according to JCPDS card 01-074-0553. No additional peaks related to any impurities were observed, indicating a high phase purity and homogeneous dispersion of the RE ions into the Y_2O_3 crystal lattice. Micro-Raman spectrum was obtained using a Labramer Horiba Jobin Yvon Micro-Raman spectrometer with a He-Ne laser excitation (λ=632.8 nm), in the range of 50–1200 cm^{-1} with 0.3 cm^{-1} spectral resolution [125]. The size, dispersion and morphology of Er^{3+}/Yb^{3+}:Y_2O_3 NPs were evaluated by transmission electron microscopy (TEM) using a JEOL JEM-100CX II microscope at an accelerating voltage of 100 kV, as shown in Figure 28a. For these measurements, the NPs were dispersed into anhydrous ethanol, and a drop placed over a carbon coated microscope copper grid. The TEM image of a single Er^{3+}/Yb^{3+}:Y_2O_3 NP is presented in Figure 28b. The calcinated NPs showed spherical morphology, high dispersity and an average particle size around 110 nm [125].

For the experiments described in this chapter, the samples were prepared starting from a powder form. A diluted dispersion was prepared by suspending 0.01 g of Er^{3+}/Yb^{3+}:Y_2O_3 NPs in 1 mL of isopropyl alcohol. Sonication for 5 min was done right before spin-coating of 10 µL of the dispersion on a glass coverslip (Menzel-Gläser #1). Scanning electron microscopy (SEM) was performed to investigate the NPs' dispersion on the coverslip, as shown in Figure 28c,d. The SEM images indicate a full dispersion of the luminescent spherical NPs, distant micrometers away from each other in several areas on the coverslip. Additionally, the SEM images corroborate the morphological analysis from TEM micrographs, in which the nanoparticles are monodispersed, spherical and show an average diameter of 100 nm.

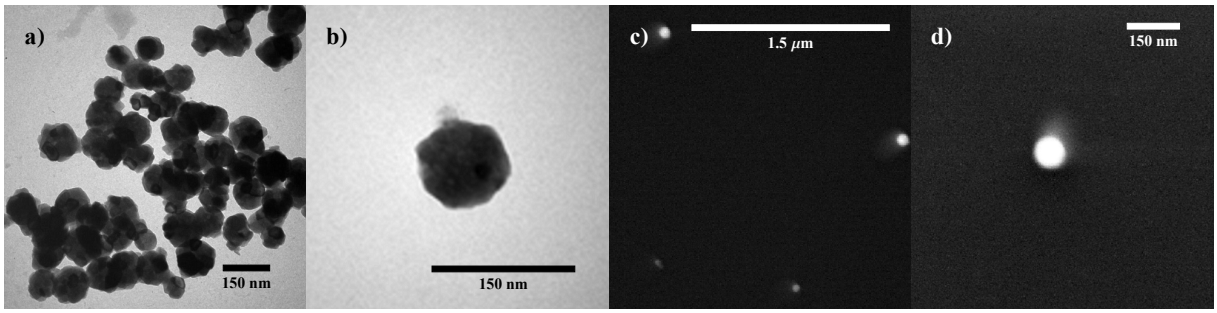

Figure 28 – a) TEM image of Er^{3+}/Yb^{3+}:Y_2O_3 NPs; b) TEM of a single NP; c) SEM after the spin coating deposition; d) SEM of a single NP deposited on a coverslip. The scale bars in a), b) and d) represent a length of 150 nm, while the one in c) represents a length of 1.5 µm. Images a) and b) were made at the Chemistry Department of São Paulo state University (Universidade de São Paulo) while images c) and d) were done at the Physics Department of the Federal University of Pernambuco (Universidade Federal de Pernambuco).

6.3 Experimental setup

With confidence that the sample preparation protocol leads very often to the occurrence of single NPs within an area larger than the detectable spot under tight focusing conditions, it's

possible to proceed with the optical spectroscopy characterization. The Er^{3+} luminescence is generated by an UC process and observed with the aid of a home-made inverted sample scanning optical microscope. A raster scan procedure was used to locate individual NPs while the focal spot of the excitation light is kept at a fixed position. The raster scan imaging process is able to discriminate single NPs from agglomerates containing more particles: due to the monodispersivity of the samples size distribution, a dimer will appear twice as bright as single NPs, which by the way occur far more frequently due to the employed sample preparation protocol. The sample's local temperature was set and controlled by a heating mantle embracing the microscope objective, ranging from 298 K to 347 K as measured at the sample's position using a carefully calibrated IR camera (FLIR Systems-i5). During the pump power dependency tests, the NPs temperature was set to 298 K, while for the FIR measurements a local temperature within the mentioned range was assigned to each fluorescence spectrum.

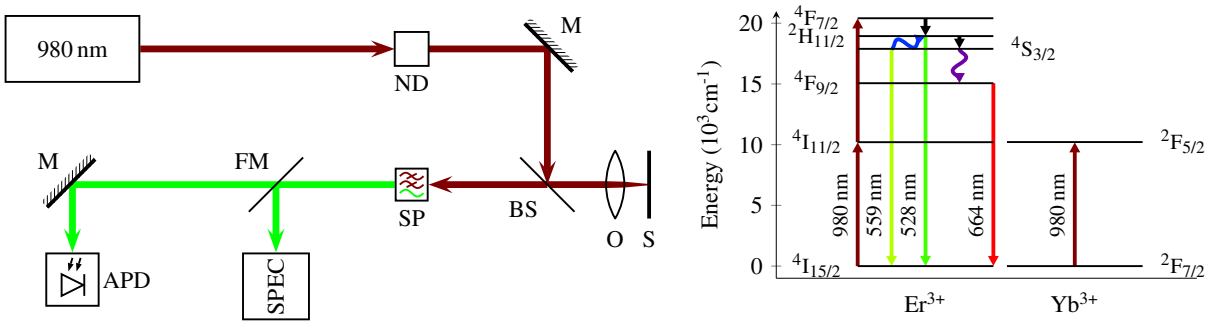

Figure 29 – Experimental setup for UC detection (left) and energy diagram for Er^{3+}/Yb^{3+}:Y_2O_3 (right). ND: variable combination of neutral density filters; M: mirror; BS: beamsplitter; O: objective; S: sample; SP: shortpass filter; FM: flip mirror; APD: avalanche photodiode. In the energy diagram, the curly blue (purple) arrow indicates the multiphonon process responsible for the $^2H_{11/2} \rightarrow {}^4I_{15/2}$ ($^4F_{9/2} \rightarrow {}^4I_{15/2}$) transition of the Er^{3+} ions. The black arrows represent nonradiative decays to lower energy levels.

For studying nanothermometry exploiting an UC excitation scheme, the experimental setup shown in Figure 29 was built. A tunable narrow-bandwidth diode laser (New Focus TLD 6900) tuned to 980 nm was sent to the inverted microscope. This laser was chosen due to its fine tuning capabilities, which allowed an optimal pump wavelength for the maximum UC signal, so that the integration time for each spectrum could be limited to 10 s. The laser is then directed to the microscope objective (100×, NA=1.25), which focuses the excitation light at a diffraction limited spot at the sample, so that when a single NP is placed right at the focal point by a 3-axis piezo stage; the emitted fluorescence can be collected by the same objective and directed to either a spectrometer or an avalanche photodiode using a flip mirror. Shortpass filters (Thorlabs FES0750 and Semrock FF01-842-sp-25) were used to block the pump laser light, letting the upconverted fluorescence pass through. The beamsplitter BS (Thorlabs BS1) could incorporate the shortpass function if replaced by a dichroic mirror, but that would make the apparatus less versatile in terms of pump laser wavelength as well as the collected signal. Therefore, in order to

find a good compromise between losses and versatility, a beamsplitter and a good shortpass is a suitable option.

Several well-established mechanisms have been proposed to describe the UC signal generated by Er^{3+}/Yb^{3+} codoped systems. Energy Transfer Upconversion (ETU), Excited-State Absorption (ESA), and Ground-State Absorption (GSA) can be responsible for generating the visible luminescence [158]. Among these excitation processes, the ETU mechanisms are the most expressive in systems like the one studied in the present work, since the absorption cross-section around 980 nm for Yb^{3+} ions is much greater than for Er^{3+} ions [159]. Different two-photon processes using light at 980 nm can take the Er^{3+} ions to the $^4F_{7/2}$ excited state, and then the thermally coupled levels $^4S_{3/2}$ and $^2H_{11/2}$ of Er^{3+} ions are populated via nonradiative decay processes [160]. The first possibility is a successive promotion from $^4H_{11/2}$ to $^4F_{7/2}$; the second one being through the presence of the $^4I_{11/2}$ metastable halfway $^4I_{15/2}$ and $^4F_{7/2}$, which enhances the probability of ETU processes due to the similar energy gap among them [161]. Nonradiative decays from higher-lying to $^4F_{7/2}$ level were also reported [162]. The result is the emission of light at a few bands in the visible, the strongest ones being in the green (around 525 nm and 550 nm) and in the red (around 664 nm).

Concerning the red emission, several pathways have been proposed in the literature involving different excitation mechanisms considering a two-photon process. [163–167]. In one of them, it is possible to occur nonradiative transitions from $^4I_{11/2}$ to $^4I_{13/2}$, then ETU and/or ESA to $^4F_{9/2}$, although the energy difference between $^4I_{13/2}$ and $^4F_{9/2}$ does not match the energy supplied by ETU/ESA. Nevertheless, it's yet another multiphonon-assisted non-resonant excitation, in which phonons are provided to the host matrix [167, 168]. In another pathway, the population of $^4F_{9/2}$ comes from a nonradiative decay from $^4S_{3/2}$.

As will be demonstrated in the Rate Equation Analysis section, for the system in question and under relatively low pump power excitation around 980 nm, the $^4F_{9/2}$ manifold provides an indirect depletion for the $^2H_{11/2}$ state. Such depopulation channel will be considered as the sole responsible for the red emission for our model. Therefore, the simplified energy diagram presented in Figure 29 shows only the relevant energy levels for the Er^{3+} ions under those assumptions. Given the advantages of the FIR method for defining a local temperature, this analysis will concentrate the discussion on the energy levels originating the green emission lines, which are thermally coupled. The red line around 664 nm will be used as a way to obtain the depletion channel for $^4S_{3/2}$ and thus the relevant fitting parameters. The luminescence spectra for the three transitions are shown in Figure 30 a), c), assigned with their barycenters. The spectra were collected for a single NP at the spectrometer branch shown in the experimental setup in Figure 29. In order to assess the appropriate pump power conditions as well as to characterize the luminescent lines as two-photon processes within a nonsaturated regime, a pump power dependency study was conducted as depicted in Figure 30 b), d), The photoluminescence intensity (I) was measured as a function of the excitation power (P) measured right after the microscope's objective. Due to the

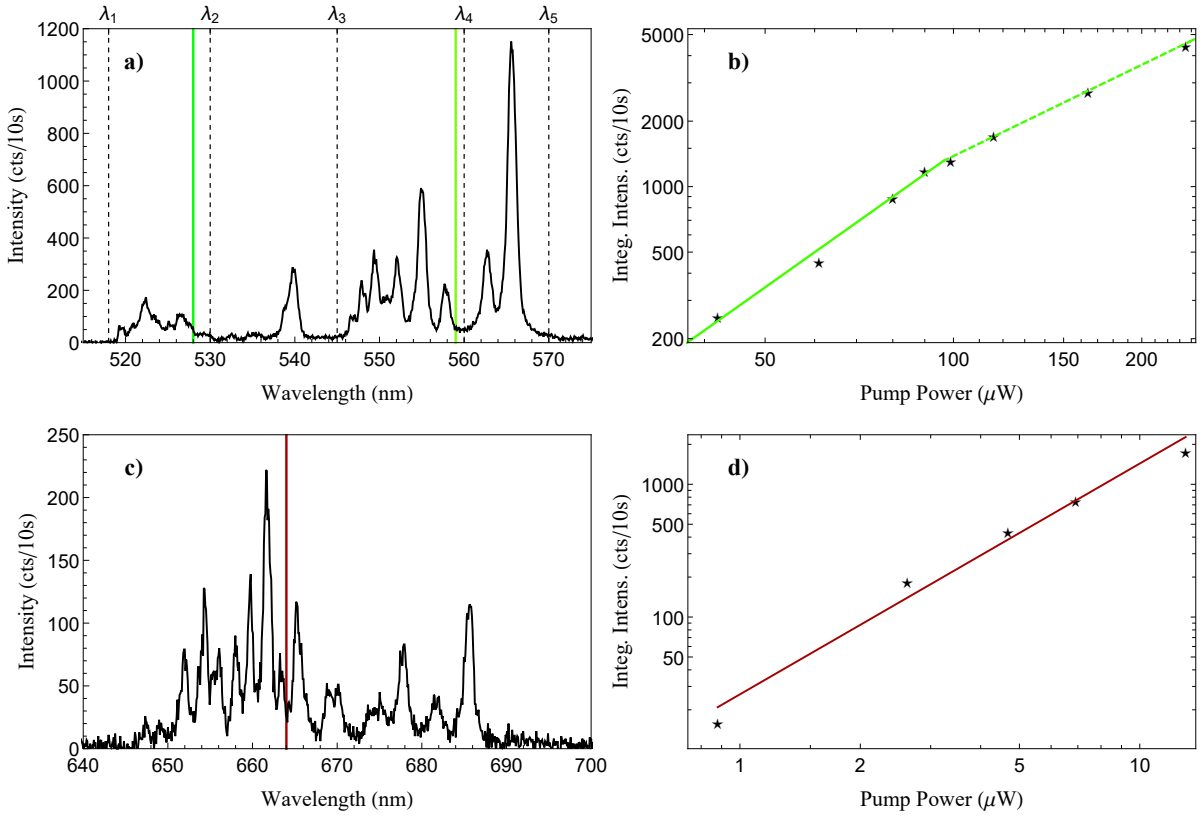

Figure 30 – Fluorescence spectra for a single Er^{3+}/Yb^{3+}:Y_2O_3 NP. On a), the wavelength intervals are given by: λ_1=518 nm, λ_2=530 nm, λ_3=545 nm, λ_4=560 nm and λ_5=570 nm. The green vertical lines are the barycenters of $^2H_{11/2}\rightarrow{}^4I_{15/2}$ (ranging from λ_1 to λ_3) and $^4S_{3/2}\rightarrow{}^4I_{15/2}$ (ranging from λ_3 to λ_5) transitions whose values are 528 nm and 559 nm respectively. On b) the dependency of the emission intensity of the two green lines combined on the pump power, presenting slopes ranging from 2.0 ± 0.1 to 1.4 ± 0.1 as the pump power increases (see text for discussion). On c), the luminescence spectrum of the $^4F_{9/2}\rightarrow{}^4I_{15/2}$ transition and the corresponding barycenter (664 nm). On d) the dependency of the emission intensity on the pump power for the red line, presenting a slope of 1.8 ± 0.1 (see text for discussion).

power dependence relationship $I \propto P^{\gamma}$, the slope of I versus P in a logarithmic scale represents the number of photons (γ) involved in the process.

At low power (below 100 μW), the green lines combined showed a value of γ of 2.0 ± 0.1. The reason why the power dependency was determined by combining the two green lines is the fact that the $^2H_{11/2}\rightarrow{}^4I_{15/2}$ transition is much less intense than the $^4S_{3/2}\rightarrow{}^4I_{15/2}$ at room temperature, so a power dependence for the former is difficult to be determined by itself at low pump powers. As the power increases to above 100 μW, saturation effects start to become significant and both green lines show a value of γ equal to 1.4 ± 0.1. Therefore, in order to avoid the saturation regimen, the pump power was limited to 100 μW. As will be demonstrated in the next section, the thermal effects measured by the FIR technique increase the relative intensity of the $^2H_{11/2}\rightarrow{}^4I_{15/2}$ transition, thus overcoming its low intensity at the low pump power limit as the temperature rises.

For the red line, which was used to determine the spectral position of the $^4F_{9/2}$ energy level, a value of 1.8 ± 0.1 was found for γ. From the spectral position of the three luminescent lines, it's possible to calculate the real energy separation between the green lines (ΔE_{real}) as $10^7 \left(\frac{1}{528} - \frac{1}{559}\right)$ or 1050 cm^{-1}. This information will be relevant for the next sections, which deal with the redistribution in the populations of the thermally coupled energy levels.

6.4 FIR nanothermometry

Following the same formalism derived in Chapter 4, the relative population between the two thermally coupled emitting levels, *R*, follows a Boltzmann-type population distribution given by [77]:

$$FIR = \frac{I_{20}}{I_{10}} = A \exp\left(\frac{-E_{21}}{kT}\right) \tag{6.1}$$

where k is Boltzmann's constant, E_{21} is the energy gap between these two excited levels and A is a constant that incorporates their spontaneous emission rates. As pointed out by Suta *et al.* [169], in order to define a proper ratiometric quantity as given by Equation 6.1, it is paramount that the Boltzmann behavior settles in just above room temperature. At high dopant concentrations, there are additional cross-relaxation pathways between neighboring rare earth ions, which competes with the non-radiative absorption rate and thus shifts the usable sensing range to higher temperatures. As will become clear in this section, such behavior was not observed and a Boltzmann-like thermometry was obtained.

As shown in Figure 31, four main regions can be identified in the green luminescence spectrum of the NPs. The matrix in question is known for being able to resolve the structure of Stark sublevels even at room temperature, thus allowing for the so-called single-band nanothermometry [129]. On the other hand, such closely separated Stark sublevels often generate a small thermal sensitivity [170]. That being said, since the second peak region in Figure 31 (labelled with a ■) lies in an intermediate position between the other three, one could mistakenly assume it is a result of the $^4S_{3/2} \rightarrow {}^4I_{15/2}$ transition. In order to solve such ambiguity, a correlation analysis was performed for the four regions. This analysis gives the Pearson correlation coefficient, which is the covariance of two variables divided by the product of their standard deviations, so that the result has a value between −1 and 1. The Pearson's correlation coefficient when applied to a sample is given by:

$$r = \frac{\sum_{i=1}^{n} (x_i - \bar{x})\,(y_i - \bar{y})}{\sqrt{\sum_{i=1}^{n} (x_i - \bar{x})^2}\sqrt{\sum_{i=1}^{n} (y_i - \bar{y})^2}} \tag{6.2}$$

where n is sample size, x_i, y_i are the individual sample points and $\bar{x} = \frac{1}{n}\sum_{i=1}^{n} x_i$ is the sample mean (analogously for $\bar{y}$). As shown in the inset of Figure 31, the first two peaks have a correlation

value of one, just like the last two. Therefore, they are linearly associated as the temperature rises and one can place the second peak into the $^2H_{11/2} \rightarrow {}^4I_{15/2}$ transition, as reported by [112]. This correlation analysis can be applied in single band nanothermometry in order to determine which pairs of Stark sublevels are the most promising for higher S_R, since it gives a quantitative measure of the degree of correlation between the transitions as the temperature changes.

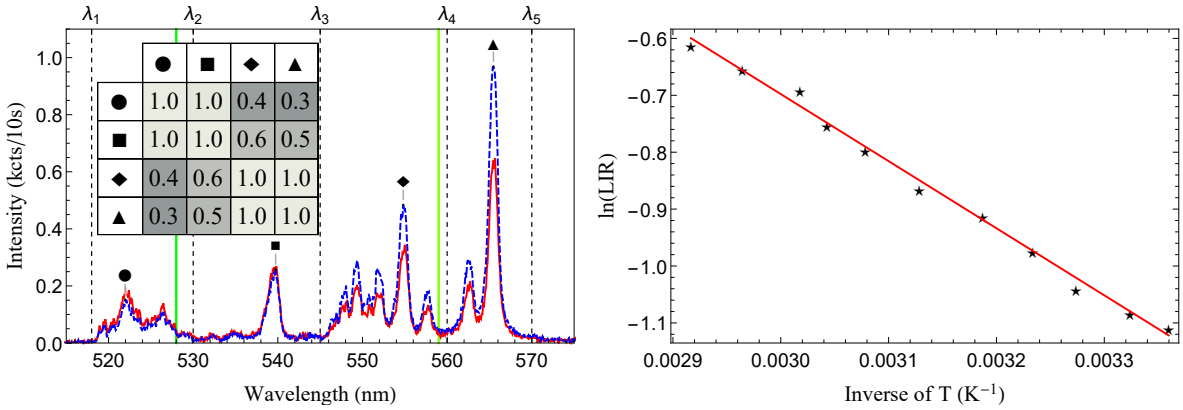

Figure 31 – FIR measurement for a single $Er^{3+}/Yb^{3+}:Y_2O_3$ NP. On the left graph, the assigned peaks lie within the wavelength intervals given by: λ_1=518 nm, λ_2=530 nm, λ_3=545 nm, λ_4=560 nm and λ_5=570 nm. The green vertical lines are the barycenters of $^2H_{11/2} \rightarrow {}^4I_{15/2}$ (ranging from λ_1 to λ_3) and $^4S_{3/2} \rightarrow {}^4I_{15/2}$ (ranging from λ_3 to λ_5) transitions. The inset shows the correlation values for the four regions. The blue dashed and red solid spectra were taken at 298 and 347 K, respectively. On the right graph, the corresponding FIR values as a function of the inverse of the temperature. The red solid line is a linear fit of the experimental data with the α and β parameters.

Because FIR is immune to pump power fluctuations, this technique is more accurate to study nanometric structures, which can be prone to spatial fluctuations while being illuminated. Following the FIR procedure described in Section 5.4, one finds $\beta = (2.84 \pm 0.10)$ and $\alpha = (1179 \pm 30)$ K, thus $S_R = (1.31 \pm 0.03)$ % at 300 K. Taking advantage of the attained spectral resolution, it would be possible to define a FIR between the first peak shown in Figure 31 (●) and the last one (▲), since they are the furthest apart. Following that procedure, one finds $S_R = (1.41 \pm 0.03)$ % at 300 K. Although the second case yields a higher sensitivity, for the sake of simplicity, the rate equation analysis will follow the first case, since it won't be necessary to consider inter-band phonon-assisted transitions. For the first case, there are only two thermally coupled energy levels ($^4S_{3/2}$ and $^2H_{11/2}$), which are represented by the two barycenters shown in Figure 31. In order to consider the interband transitions, a second pair of energy levels would be necessary, which leads to a more intrincate rate equation analysis so that the effective phonon energy would be more complicated to define.

As shown in Figure 32 the values of S_R are temperature dependent. When evaluating the potential of a system as a nanothermometer it is important to characterize and explicitly show the behavior of the relative sensitivity with T, since if the sensitivity for a given temperature reduces to a point where it impairs the nanothermometry, it effectively shortens the range of temperatures

for which the thermometer can be used, evidently one valuable information [171–175]. In this experiment, values from 1.33% to 0.98% were obtained, thus the S_R value was found to be > 1% for a temperature range of 45 K.

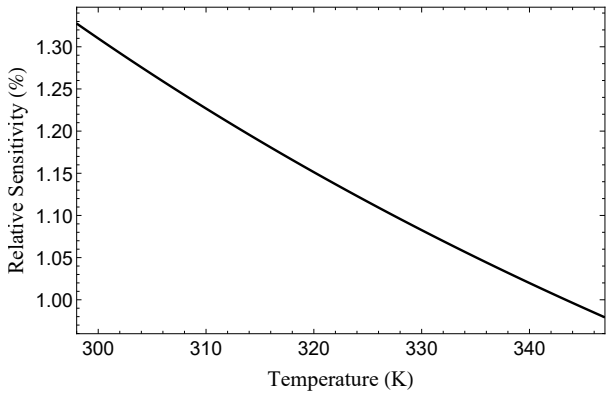

Figure 32 – S_R as a function of T for the range of temperatures investigated considered for the FIR measurements.

Besides S_R, the temperature accuracy δT is another parameter to characterize the optical thermometer. It gives the uncertainty of a temperature measurement as a result of the smallest integrated area increment in the emission spectrum that can be measured by FIR. δT is given by [134]:

$$\delta T = \frac{\delta(FIR)}{S_R(FIR)} \tag{6.3}$$

where $\delta(FIR)/FIR$ is the relative error of FIR, which value in the present case is 0.14%. Therefore, the δT value can be as low as 0.1 K at 300 K, which is typical for rare-earth-doped NPs temperature sensors [135, 176]. That measurement gives the smallest increment in temperature that can be determined around 300 K, within the range for biological applications. In order to obtain a temperature resolution closer to 0.01 K, one could improve upon the $\delta(FIR)/FIR$ which is limited by the detection apparatus efficiency and resolution.

The values for S_R and δT found in this experiment are very promising when comparing to the ones found in the literature. For instance, for the same yttria matrix, values respectively of 0.6% and 0.7 K at 273 K were reported [107]. A higher sensitivity of 1.52% at 300 K was also reported [177] as well as similar value of 1.32% [132], albeit none of these works deals with individual nanoparticles.

From the value of α one can calculate the apparent or effective energy separation between the coupled energy levels as 813 cm^{-1}. This value is approximately 23% smaller than the value of ΔE_{real} given by the luminescence spectra, as will be addressed in the next section. The phonon-assisted processes can now be modeled by a rate equation analysis of all the four relevant energy levels, including the ground state.

6.5 Rate equation analysis

Here, since the intensity of the emitted luminescence is proportional to the population of the upper energy level involved in the electronic transition, one is interested in finding the population densities for the two thermally coupled states of Er^{3+}, ($^4S_{3/2}$ and $^2H_{11/2}$). Henceforth, for the sake of simplicity, the population density of the i-th energy level (n_i; i=0,1,2,3,4,5,6,7) are associated to the states $|0\rangle$ ($^4I_{15/2}$), $|1\rangle$ ($^4I_{13/2}$), $|2\rangle$ ($^4I_{9/2}$), $|3\rangle$ ($^4F_{9/2}$), $|4\rangle$ ($^4S_{3/2}$), $|5\rangle$ ($^2H_{11/2}$), $|6\rangle$ ($^4F_{7/2}$) and $|7\rangle$ ($^2H_{9/2}$). Although several excitation mechanisms act to populate $|6\rangle$, due to the fact that the transient population dynamics is not of interest here (in fact, the thermal equilibrium populations are the important parameters for the present study), in the steady-state regime these processes can be congregated into an effective term. This single term takes into account ETU, ESA and possible cross-relaxation processes between Er^{3+}-Er^{3+}, although the latter case is less probable given the low ion concentration. In order to further simplify the analysis, the problem can be treated as if a single photon excites directly the $|4\rangle$ level. This approach generates an equivalent 4-level system from the original problem, thus reducing the amount of terms to be determined and allowing an analytical solution. It's worth mentioning that such simplification does not assume a resonant excitation on the $|4\rangle$ level, although it could be achieved with alternative laser sources. Therefore, a system of rate equations can be written as [137, 138]:

$$\frac{dn_0}{dt} = -\sigma_0 \Phi_{eff} n_0 + \gamma_4(T)\, n_4 + \gamma_5(T)\, n_5 \tag{6.4}$$

$$\frac{dn_4}{dt} = \sigma_0 \Phi_{eff} n_0 - \left[\Lambda_{45}(T) + \gamma_4(T)\right] n_4 \tag{6.5}$$

$$\frac{dn_5}{dt} = \Lambda_{45}(T)\, n_4 - \left[\Lambda_{56}(T) + \gamma_5(T)\right] n_5 \tag{6.6}$$

where Φ_{eff} is the effective photon flux and σ_0 is the effective absorption cross section corresponding to the $|0\rangle \rightarrow |4\rangle$ transition. The multiphonon excitation rates are given by $\Lambda_{ij} = C_{ij}^{ep} P_{ij}(T)$, where C_{ij}^{ep} is a parameter proportional to the electron–phonon coupling and $P_{ij}(T)$ are the phonon occupancy numbers given by [139]:

$$P_{ij}(T) = \left[\exp\left(\frac{\hbar\omega}{kT}\right) - 1\right]^{-q_{ij}} \tag{6.7}$$

where q_{ij} is the number of effective phonons with energy $\hbar\omega$ involved in the multiphonon excitation from level i to level j, k is the Boltzmann constant, and T is sample's absolute temperature. The population relaxation rates are given by:

$$\gamma_i(T) = \gamma_i^{rad} + W_i^{NR}(T) \tag{6.8}$$

with $\left(\gamma_i^{rad}\right)^{-1}$ being the radiative decay time. $W_i^{NR}(T)$ is the nonradiative relaxation rate from level i due to multiphonon relaxation processes. Choosing a reference temperature T_0, for which the nonradiative decay rate in the host matrix is known, $W_i^{NR}(T)$ can be written as [141]:

$$W_i^{NR}(T) = W_i^{NR}(T_0)\left[\frac{1-\exp\left(-\frac{\hbar\omega}{kT}\right)}{1-\exp\left(-\frac{\hbar\omega}{kT_0}\right)}\right]^{-q_i} \tag{6.9}$$

where q_i represents the number of effective phonons involved in the relaxation of level i to the closest low energy level. $W_i^{NR}(T_0)$ is the nonradiative relaxation rate at a set temperature, *e. g.*, room temperature or 300 K. The ratio between the populations in the coupled energy levels can be obtained from the steady state condition and setting the derivatives equal to zero, which gives:

$$\frac{n_4}{n_5} \approx \frac{C_{45}^{ep}\left[\exp\left(\frac{\hbar\omega}{kT}\right)-1\right]^{-q_{45}}}{W_5^{NR}(T_0)\left[\frac{1-\exp\left(-\frac{\hbar\omega}{kT}\right)}{1-\exp\left(-\frac{\hbar\omega}{kT_0}\right)}\right]^{-q_5}} \tag{6.10}$$

Given the populations ratio, one can calculate the FIR parameters applying Boltzmann's factor:

$$\ln\left(\frac{I_j}{I_i}\right) \approx \beta - \frac{\Delta E_{eff}^{ij}}{kT}, \tag{6.11}$$

where ΔE_{eff}^{ij} was derived for Nd^{3+}:Y_2O_3 NPs as [96]:

$$\Delta E_{eff}^{ij} = \left[\frac{\exp\left(\frac{\hbar\omega}{kT_0}\right)\Delta E_{real}^{ij} - q_i\hbar\omega}{\exp\left(\frac{\hbar\omega}{kT_0}\right)-1}\right] \tag{6.12}$$

Equation 6.12 can be solved for $\hbar\omega$ in units of kT_0:

$$\hbar\omega = \frac{\Delta E_{eff}^{ij}}{q_i} - \mathcal{W}\left[\frac{\left(\Delta E_{eff}^{ij} - \Delta E_{real}^{ij}\right)\exp\left(\frac{\Delta E_{eff}^{ij}}{q_i}\right)}{q_i}\right], \tag{6.13}$$

where $\mathcal{W}(x)$ is the Lambert W function [178]. It's defined as:

$$\mathcal{W}(x)\exp\left[\mathcal{W}(x)\right] = x \tag{6.14}$$

If x is real, then for $-1/e \leq x < 0$ there are two possible real values of $\mathcal{W}(x)$. The branch satisfying $-1 \leq \mathcal{W}(x)$ is denoted by $\mathcal{W}_0(x)$ and the branch satisfying $\mathcal{W}(x) \leq -1$ is $\mathcal{W}_{-1}(x)$. $\mathcal{W}_0(x)$ is referred to as the principal branch of the $\mathcal{W}$ function. Equation 6.13 admits solutions for three basic situations: i) $\Delta E_{eff}^{ij} > \Delta E_{real}^{ij}$; ii) $\Delta E_{eff}^{ij} = \Delta E_{real}^{ij}$ and iii) $\Delta E_{eff}^{ij} < \Delta E_{real}^{ij}$. For the first case, $x > 0$ in the argument of $\mathcal{W}$, thus only one solution is obtained for $(\hbar\omega, q_i)$. For the second case, one gets:

$$\hbar\omega = \frac{\Delta E_{eff}^{ij}}{q_i} - \mathcal{W}\left[0\right] = \frac{\Delta E_{eff}^{ij}}{q_i} = \frac{\Delta E_{real}^{ij}}{q_i} = \frac{\hbar\omega q_{ij}}{q_i} \tag{6.15}$$

Thus, $q_{ij} = q_i$ and the process follows a simple Boltzmann distribution and can be understood as if the same number of phonons is responsible for both the thermal redistribution and the depopulation of the lower energy level. For the third case, $x < 0$ in the argument of $\mathcal{W}$, however, the $\mathcal{W}_{-1}\left(x\right)$ branch can generate values for $\hbar\omega$ well above the typical phonon cut-off frequencies.

Let's now study the first case ($\Delta E_{eff}^{ij} > \Delta E_{real}^{ij}$), as it often happens with Er^{3+}/Yb^{3+}-codoped NPs, for which the measured relative sensitivity is larger than the predicted by the energy separation alone. As proposed by [148], this is a result of a nonradiative decay from $^4S_{3/2}$ to $^4F_{9/2}$. In order to demonstrate that hypothesis analytically, one can set q_i to zero. However, Equation 6.13 becomes indeterminate in such limit. The expression can be modified assuming that a depopulation of the lower energy level requires a different value for $\hbar\omega$:

$$\Delta E_{eff}^{ij} = \left[\frac{\exp\left(\frac{\hbar\omega^{ij}}{kT_0}\right)\Delta E_{real}^{ij}}{\exp\left(\frac{\hbar\omega^{ij}}{kT_0}\right) - 1}\right] - \left[\frac{q_i\hbar\omega^i}{\exp\left(\frac{\hbar\omega^i}{kT_0}\right) - 1}\right], \tag{6.16}$$

where $\hbar\omega^{ij}$ is the energy required for each phonon to overcome the energy separation while $\hbar\omega^i$ is the one associated with the nonradiative decay to a lower energy level ($^4F_{9/2}$). The occurrence of phonon modes with distinct energies is possible for a crystalline matrix, which often presents multiple clearly resolved phonon lines. The resonance in the electronic transitions can select specific phonon modes among the ones available in the matrix. Equation 6.13 is now given by (in units of kT_0):

$$\hbar\omega^{ij} = \ln\left\{\frac{\hbar\omega^i q_i + \Delta E_{eff}^{ij}\left[\exp\left(\hbar\omega^i\right) - 1\right]}{\hbar\omega^i q_i + \left(\Delta E_{eff}^{ij} - \Delta E_{real}^{ij}\right)\left[\exp\left(\hbar\omega^i\right) - 1\right]}\right\} \tag{6.17}$$

taking $q_i = 0$ in Equation 6.17, one gets:

$$\hbar\omega_0^{ij} = \ln\left(\frac{\Delta E_{eff}^{ij}}{\Delta E_{eff}^{ij} - \Delta E_{real}^{ij}}\right), \tag{6.18}$$

which gives a simple expression for the phonon energy in the absence of nonradiative decays for $\Delta E_{eff}^{ij} > \Delta E_{real}^{ij}$. In order to verify the appropriateness of Equation 6.18, one can apply it to another host matrix for which the thermometric parameters are known, such as $NaYF_4$. Using the results obtained from Gonçalves *et al.* [148], one finds 366 cm^{-1} for the phonon energy $\hbar\omega_0^{ij}$, which matches one of the dominant phonon modes (370 cm^{-1}) in $NaYF_4$ [160, 179]. As the nonradiative decay to lower energy levels is introduced, the effective phonon energy decreases as

given by Equation 6.17. By setting the $\hbar\omega^i q_i$ energy equal to the separation between $^4S_{3/2}$ and $^4F_{9/2}$ energy levels (ΔE_{NR}^{ij}), Equation 6.17 becomes:

$$\hbar\omega^{ij} = \ln\left\{\frac{\Delta E_{NR}^{ij} + \Delta E_{eff}^{ij}\left[\exp\left(\frac{\Delta E_{NR}^{ij}}{q_i}\right) - 1\right]}{\Delta E_{NR}^{ij} + \left(\Delta E_{eff}^{ij} - \Delta E_{real}^{ij}\right)\left[\exp\left(\frac{\Delta E_{NR}^{ij}}{q_i}\right) - 1\right]}\right\} \tag{6.19}$$

Table 7 – Multiphonon parameters for Er^{3+}/Yb^{3+}:Y_2O_3 single NPs

$\hbar\omega^{ij}$ (cm^{-1})	$\hbar\omega^{i}$ (cm^{-1})	ΔE_{eff}^{ij} (cm^{-1})	ΔE_{real}^{ij} (cm^{-1})	ΔE_{NR}^{ij} (cm^{-1})
355	404	813	1050	2829

Equation 6.19 can be solved in order to find the best combination (i. e., the one which fits the measured energy values with the least amount of whole phonon numbers) of $\left(\hbar\omega^{ij}, q_i\right)$ values, as shown in Table 7. For our experiments, it was found that $\Delta E_{eff}^{ij} < \Delta E_{real}^{ij}$, which corresponds to the Case iii) of Equation 6.13. That could be a result of a specific matching between the Y_2O_3 phonon lines and the value of ΔE_{real}^{ij}. In order to calculate the phonon energies involved in the process, Equation 6.19 was used rather than Equation 6.13. This choice was motivated by the debate around the definition of the mediating or effective frequency pointed out by Auzel [139]. When the highest phonon frequency arises from internal vibration of a molecular radical such as $(WO_4)^{-2}$ in calcium tungstate, (≈900 cm^{-1}), it's more difficult to define a single mediating mode. Englman and Jortner [180] proposed that the effective frequency should be the cut-off frequency in weak coupling (where the relative horizontal displacement of the two potential energy surfaces is small) and an average frequency for strong coupling (when there is substantial horizontal displacement of the potential energy surfaces of the electronic states). The FIR measurements performed in this chapter were repeated for three individual NPs and the valued of S_R fluctuated within the statistical error. That corroborates the effectiveness of the synthetic route into producing uniformly doped NPs. That being said, for one of the aforementioned NPs, the calculated parameters for Equation 6.19 are summarized in Table 7. The value of $\hbar\omega^i$ is calculated from Equation 6.17.

More recently, as previously pointed out by Eldridge [112], Kennedy [181] showed that a dual effective phonon model for multiphonon relaxation could account for a wide range of temperatures from high to low $\hbar\omega_{eff}$. The theoretical model developed in this chapter also introduces the effects of the more energetic phonons in the multiphonon relaxation process. Given the value for ΔE_{NR}^{ij} (2829 cm^{-1} between $^4S_{3/2}$ and $^4F_{9/2}$), phonons of energy beyond 377 cm^{-1} could be involved in the process, effectively skewing the phonon density of states. On the other hand, from the Raman spectrum shown in Figure 33c, it's expected that the calculated effective phonon frequencies should be close to the most dominant phonon line (◀), as confirmed by the experimental results from Chapter 5, since it deals with the same host matrix. As shown in Figure 33, three phonons of energy 355 cm^{-1} are responsible for populating the $^2H_{11/2}$ level,

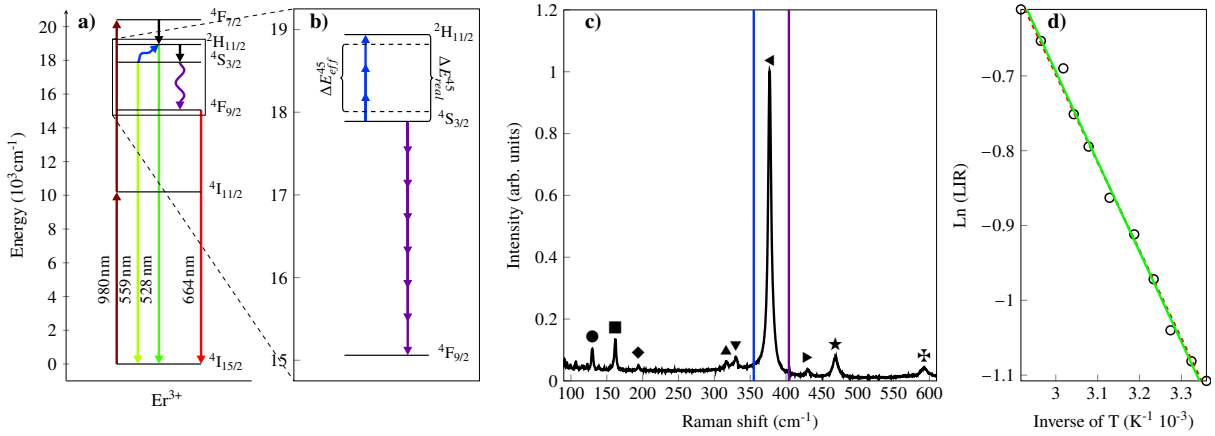

Figure 33 – Visual representation of the multiphonon assisted UC process. a): simplified version of the energy diagram for Er^{3+}; b): zoomed in section of the thermally coupled $^2H_{11/2}$ and $^4S_{3/2}$ energy levels as well as the $^4F_{9/2}$, which acts depleting the population of the latter. The number of phonons acting in each process is represented by three blue arrows of energy 355 cm^{-1} and seven of energy 404 cm^{-1}. c): calculated values of $\hbar\omega^{ij}$ (blue) and $\hbar\omega^{i}$ (purple) compared to the Raman spectrum; d): comparison between the predictions of the theoretical model and the FIR experimental data. The green solid line is the rate equation model while the red dashed one is a least squares fit for the FIR.

while seven phonons of energy 404 cm^{-1} are responsible for the nonradiative decay of $^4S_{3/2}$ to $^4F_{9/2}$. This process will make the $^4F_{9/2}\rightarrow{}^4I_{15/2}$ temperature dependent, so for this process alone, it's expected that the transition should increase its luminescence as the temperature rises. From the rate equation analysis, $\hbar\omega^{ij}$ was found to be smaller than the dominant phonon line (377 cm^{-1}). Moreover, the presence of higher energy phonons depleting the population of $|4\rangle$ acts in this case to shorten the energy separation between the coupled energy levels. One could define average values for $\hbar\omega$ as follows:

$$\overline{\hbar\omega} = \frac{\hbar\omega^{ij} + \hbar\omega^{i}}{2} \approx 380 \text{ cm}^{-1} \tag{6.20}$$

$$\langle\hbar\omega\rangle = \frac{q_{ij}\hbar\omega^{ij} + q_i\hbar\omega^{i}}{q_{ij} + q_i} \approx 390 \text{ cm}^{-1} \tag{6.21}$$

The average phonon energy ($\overline{\hbar\omega}$) is thus very close to the dominant Raman line shown in Figure 33c (◀). The $\langle\hbar\omega\rangle$ value on the other hand is slightly larger, thus indicating the influence of the higher energy phonons in the density of states. In Figure 33 d), a value of 2.92 was found for β, 3% bigger than the one obtained from direct FIR measurements. For α, which is the more critical parameter, the difference is 2%. The value for $\hbar\omega^{ij}$ is close to the one calculated for Nd^{3+}:Y_2O_3 NPs [96], thus confirming the appropriateness of the model in finding the best fitting parameters. From the calculated parameters for Equation 6.1, one can assign an uncertainty of about 20 cm^{-1} to the value of ΔE_{real}^{ij}, which corresponds to an uncertainty of 30 cm^{-1} to the value of $\hbar\omega^{ij}$. That is the main source of errors in the model, since the other parameters are limited by

the spectrometer's resolution, which is only 3 cm^{-1} around 532 nm. That being said, one finds the uncertainty of $\overline{\hbar\omega}$ and $\langle\hbar\omega\rangle$ as 15 cm^{-1} and 10 cm^{-1} respectively. Therefore, the values of $\overline{\hbar\omega}$ and $\langle\hbar\omega\rangle$ are equivalent within the statistical error and are well represented by the dominant Raman mode.

In conclusion, a Er^{3+}/Yb^3-based nanothermometer was characterized by FIR in an UC configuration, with NPs excitation being performed by a CW laser emitting at 980 nm, within one important biological window. The experimental results showed a sensitivity of 1.31% and an accuracy of 0.1 K at 300 K. A rate equation model was derived for the multiphonon assisted processes in good agreement with the experimental results for a low pump power (below 100 µW) and small temperature range (up to 347 K). To the best of our knowledge, this is the first report of such system in the single NP level to provide a rate equation model for the multiphonon processes. A dual effective phonon model was proposed in order the determine the yttria's effective phonon energy, whose average value met the most energetic Raman mode, 377 cm^{-1}. In this model, phonons of energy both smaller (355 cm^{-1}) and larger (404 cm^{-1}) than the commonly known cut-off frequency (380 cm^{-1}) are responsible for the thermal redistribution. The former act populating the upper coupled energy level while the latter act as an indirect depletion of the lower. This kind of analysis can be transposed to other pumping wavelengths, thus allowing for other electronic transitions to be explored for nanothermometry. Moreover, the behavior of NPs-based nanothermometers in different media of biological interest is also important for a more concrete evaluation of the usefulness of such systems.

To conclude this work, the results from both the Er^{3+}/Yb^3 and the Nd^{3+}:Y_2O_3 NPs will be compared so that the best system can be chosen for WGM spectroscopy applications. This analysis takes into account not only the relative sensitivity and accuracy values but also the excitation and emission wavelengths that can be achieved with the available tunable diode lasers and that can be easily detected with our setup. One of the key elements for efficient WGM coupling is keeping the cavity's temperature stable, since temperature fluctuations will shift and distort the resonances. Therefore, a nanometric probe can be designed to monitor the local temperature without significant distortions in the thermal equilibrium. The same laser can be used for both the WGM spectroscopy and for the nanothermometry measurements, thus simplifying the experimental setup.

7 CONCLUSIONS AND PERSPECTIVES

In this thesis, two systems were tested for nanothermometry measurements with individual yttria NPs: one doped with Nd^{3+} ions (Chapter 5) and another codoped with Er^{3+}, Yb^{3+} ions (Chapter 6). Additionally, in Chapter 3, the WGMs in silica microspheres were calculated around a pump wavelength of 685 nm, which is one of the available tunable diode lasers for WGM coupling. The other one being the 980 nm infrared laser used for the experiments in Section 6.3. Since the 685 nm pump wavelength lies in the visible range of the spectrum, it helps with the WGM coupling and overall alignment of the system. That being said, one can combine that pump wavelength with one of the two luminescent systems tested in previous chapters. The $^4I_{9/2} \rightarrow {}^4F_{9/2}$ absorption band of Nd^{3+} lies within the range of 680 nm to 690 nm and is thus a suitable candidate [182, 183]. In addition, Er^{3+}-doped yttria NPs could be characterized as a temperature sensor under 660 nm excitation [184], however such wavelength lies outside the tunable diode laser's range.

In order to test whether or not the Nd^{3+} emission could be achieved with the visible tunable diode laser's wavelength, a length of 1 m of a Nd^{3+}-doped single-mode silica optical fiber (INO Nd100) was pumped with the 685 nm laser in a configuration similar to the one shown in Section 5.3.2, so that the fluorescence spectra from the $^4F_{5/2} \rightarrow {}^4I_{9/2}$ transition as well as $^4F_{3/2} \rightarrow {}^4I_{9/2}$ could be observed. The fiber emission was collected using a Red Tide USB650 Fiber Optic Spectrometer. Figure 34 shows the emission spectrum for the $^4F_{3/2} \rightarrow {}^4I_{9/2}$ centered around 901 nm and a linear pump power dependency as expected for this single photon process. The $^4F_{5/2} \rightarrow {}^4I_{9/2}$ transition could not be observed due to its lower intensity, particularly at room temperature. The 685 nm tunable diode laser offers a smooth pump power control, which can reach up to 10 mW, which is adequate to excite WGMs in a silica microsphere.

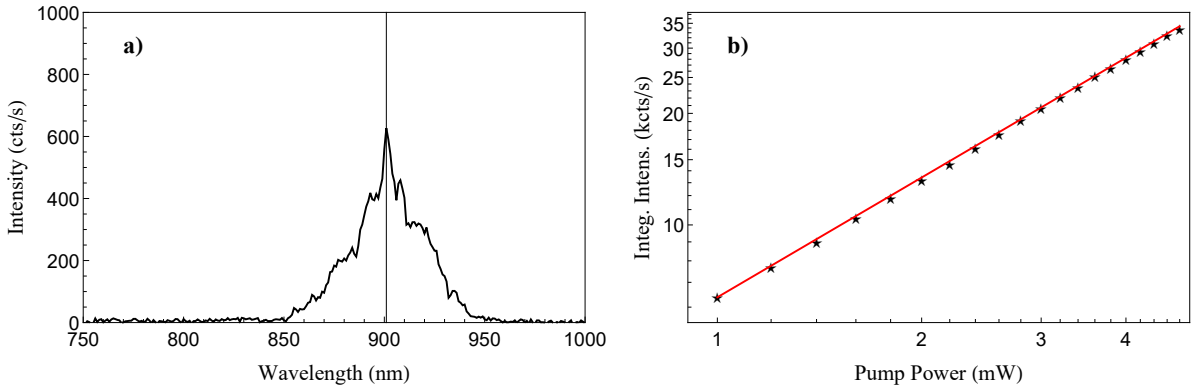

Figure 34 – a) Emission spectrum for the $^4F_{3/2} \rightarrow {}^4I_{9/2}$ transition under 685 nm excitation for a Nd^{3+} doped fiber. The vertical line is the barycenter around 901 nm. b) log-log plot of integrated total counts for the transition as a function of the incident pump power. The red line represents the best apparent linear fit with a slope of (1.0 ± 0.1)

Taking into account the results from Figure 34, the next stage would be to reproduce the results from Chapter 5 with the 685 nm pump laser. One could also make a doped Nd^{3+} microsphere and follow the methodology of Chapter 4 in order to achieve WGM coupling while the emission spectra is recorded at different temperatures. Finally, the last stage would be to combine a single Nd^{3+} doped Y_2O_3 NPs and an undoped silica microsphere in order to compare the silica and the yttria performances as a host matrix. Figure 35 represents the experimental setup for WGMs coupling in a Nd^{3+}-doped microsphere.

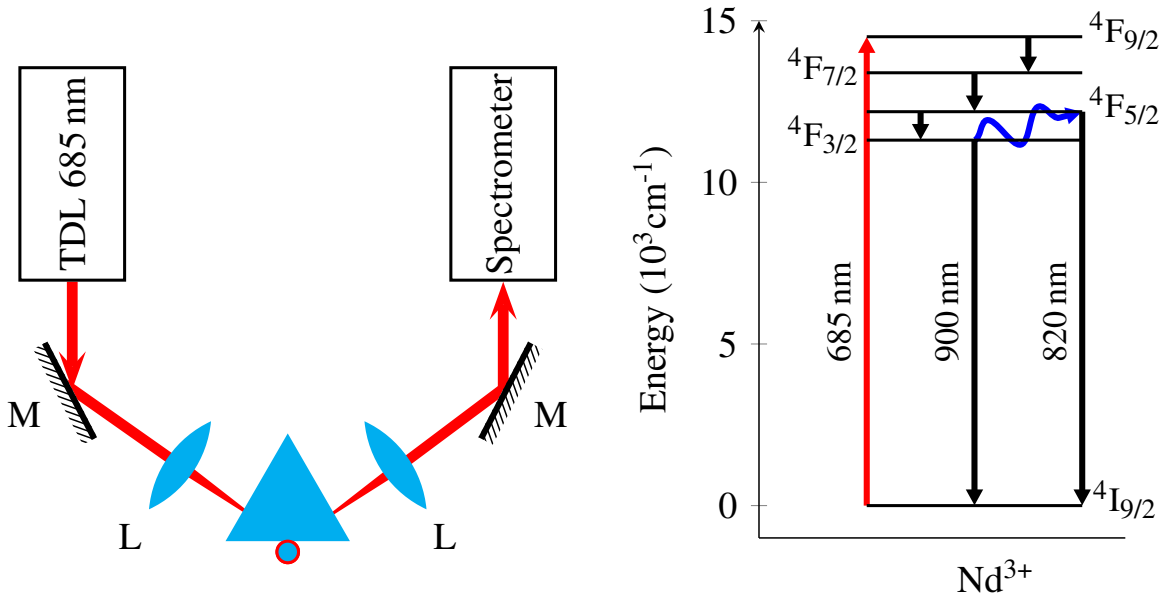

Figure 35 – Experimental setup diagram (left) and energy levels for a Nd^{3+} doped silica microsphere under 685 nm pump excitation. The blue arrow represents the multiphonon processes.

In this configuration, several temperature sensing parameters can be assessed at the same time, such as the resonance line shift, line width and luminescence intensity ratio with the advantage of a single pump wavelength being used. Those experiments were intended for the following chapters of this thesis. However, this research suffered greatly from the restrictions imposed by the coronavirus outbreak of 2020. Since this thesis relies heavily on the access of laboratory facilities, the extended period of time during which the University was closed had a negative impact on the experimental results. Moreover, in order to improve the effectiveness of the WGMs coupling, a five-axis micropositioner (MDE277 Elliot Scientific) was ordered to control the position of the coupling lens and this purchase was also delayed during that time frame.

That being said, this research had to be finished prematurely taking into account the program's time limit. The experiments regarding the Nd^{3+}-doped microspheres and the downconversion in single yttria NPs under 685 nm excitation will thus be treated in future works, since this particular configuration, to the best of our knowledge, was not yet considered for WGMs-based sensing applications.

BIBLIOGRAPHY

1 RAYLEIGH, L. CXII. The problem of the whispering gallery. *The London, Edinburgh, and Dublin Philosophical Magazine and Journal of Science*, v. 20, n. 120, p. 1001–1004, 1910.

2 MATSKO, A.; ILCHENKO, V. Optical resonators with whispering-gallery modes-part I: basics. *IEEE Journal of Selected Topics in Quantum Electronics*, v. 12, n. 1, p. 3–14, 2006.

3 SAVCHENKOV, A. A. et al. Whispering-gallery-mode resonators as frequency references. II. Stabilization. *J. Opt. Soc. Am. B*, OSA, v. 24, n. 12, p. 2988–2997, 2007.

4 HE, L. et al. Detecting single viruses and nanoparticles using whispering gallery microlasers. *Nature Nanotechnology*, v. 6, n. 7, p. 428–432, 2011.

5 VOLLMER, F.; ARNOLD, S.; KENG, D. Single virus detection from the reactive shift of a whispering-gallery mode. *Proceedings of the National Academy of Sciences*, v. 105, n. 52, p. 20701–20704, 2008.

6 TRICHET, A. A. P. et al. Nanoparticle Trapping and Characterization Using Open Microcavities. *Nano Letters*, American Chemical Society, v. 16, n. 10, p. 6172–6177, 2016.

7 LECIEUX, Y. et al. Whispering gallery modes for 3D strain measurement. *Optics & Laser Technology*, v. 149, p. 107862, 2022.

8 SCHUBERT, M. et al. Lasing within Live Cells Containing Intracellular Optical Microresonators for Barcode-Type Cell Tagging and Tracking. *Nano Letters*, American Chemical Society, v. 15, n. 8, p. 5647–5652, 2015.

9 HUMAR, M.; YUN, S. H. Intracellular microlasers. *Nature Photonics*, v. 9, n. 9, p. 572–576, 2015.

10 WU, X. et al. Nanowire lasers as intracellular probes. *Nanoscale*, v. 10, p. 9729–9735, 2018.

11 TOROPOV, N. et al. Review of biosensing with whispering-gallery mode lasers. *Light: Science & Applications*, v. 10, n. 1, p. 42, 2021.

12 SOLER-CARRACEDO, K. et al. Luminescent Nd^{3+}-Based Microresonators Working as Optical Vacuum Sensors. *Advanced Optical Materials*, v. 8, n. 19, p. 2000678, 2020.

13 JIANG, X.; YANG, L. Optothermal dynamics in whispering-gallery microresonators. *Light: Science & Applications*, v. 9, n. 1, p. 24, 2020.

14 GUAN, G.; ARNOLD, S.; OTUGEN, M. V. Temperature Measurements Using a Microoptical Sensor Based on Whispering Gallery Modes. *AIAA Journal*, v. 44, n. 10, p. 2385–2389, 2006.

15 NAM, S. H.; YIN, S. High-temperature sensing using whispering gallery mode resonance in bent optical fibers. *IEEE Photonics Technology Letters*, v. 17, n. 11, p. 2391–2393, 2005.

16 GUHA, B.; CARDENAS, J.; LIPSON, M. Athermal silicon microring resonators with titanium oxide cladding. *Opt. Express*, OSA, v. 21, n. 22, p. 26557–26563, 2013.

17 XU, L. et al. High-Q silk fibroin whispering gallery microresonator. *Opt. Express*, OSA, v. 24, n. 18, p. 20825–20830, 2016.

18 LIAO, J.; YANG, L. Optical whispering-gallery mode barcodes for high-precision and wide-range temperature measurements. *Light: Science & Applications*, v. 10, n. 1, p. 32, 2021.

19 WALO-MARTÍN, D. et al. Temperature Sensing with Nd^{3+} Doped YAS Laser Microresonators. *Applied Sciences*, v. 11, n. 3, 2021.

20 CAI, L. et al. Whispering Gallery Mode Optical Microresonators: Structures and Sensing Applications. *physica status solidi (a)*, v. 217, n. 6, p. 1900825, 2020.

21 WANG, P. et al. Packaged, high-Q, microsphere-resonator-based add–drop filter. *Opt. Lett.*, Optica Publishing Group, v. 39, n. 17, p. 5208–5211, 2014.

22 COLLOT, L. et al. Very High-Q Whispering-Gallery Mode Resonances Observed on Fused Silica Microspheres. *Europhysics Letters (EPL)*, IOP Publishing, v. 23, n. 5, p. 327–334, 1993.

23 CHILDS, P. R. N. Nanoscale Thermometry and Temperature Measurement. In: CARLOS, L. D.; PALACIO, F. (Ed.). *Thermometry at the Nanoscale: Techniques and Selected Applications*. London: The Royal Society of Chemistry, 2016. cap. 1, p. 1–22.

24 HARTMANN, M. J. Chapter 2 minimal length scales for the existence of local temperature. In: CARLOS, L. D.; PALACIO, F. (Ed.). *Thermometry at the Nanoscale: Techniques and Selected Applications*. [S.l.]: The Royal Society of Chemistry, 2016. p. 23–38.

25 KIM, P. et al. Thermal Transport Measurements of Individual Multiwalled Nanotubes. *Phys. Rev. Lett.*, American Physical Society, v. 87, p. 215502, 2001.

26 SCHMIDT, M. et al. Irregular variations in the melting point of size-selected atomic clusters. *Nature*, v. 393, n. 6682, p. 238–240, 1998.

27 HARTMANN, M. et al. Scaling behavior of interactions in a modular quantum system and the existence of local temperature. *Europhysics Letters (EPL)*, IOP Publishing, v. 65, n. 5, p. 613–619, 2004.

28 LEBOWITZ, J. L.; LIEB, E. H. Existence of Thermodynamics for Real Matter with Coulomb Forces. *Phys. Rev. Lett.*, American Physical Society, v. 22, p. 631–634, 1969.

29 SUZUKI, M.; PLAKHOTNIK, T. The challenge of intracellular temperature. *Biophysical Reviews*, v. 12, n. 2, p. 593–600, 2020.

30 OKABE, K. et al. Intracellular temperature mapping with a fluorescent polymeric thermometer and fluorescence lifetime imaging microscopy. *Nature Communications*, v. 3, n. 1, p. 705, 2012.

31 KIYONAKA, S. et al. Genetically encoded fluorescent thermosensors visualize subcellular thermoregulation in living cells. *Nature Methods*, v. 10, n. 12, p. 1232–1238, 2013.

32 HAYASHI, T. et al. A Cell-Permeable Fluorescent Polymeric Thermometer for Intracellular Temperature Mapping in Mammalian Cell Lines. *PLOS ONE*, Public Library of Science, v. 10, n. 2, p. 1–18, 2015.

33 UCHIYAMA, S. et al. A cationic fluorescent polymeric thermometer for the ratiometric sensing of intracellular temperature. *Analyst*, The Royal Society of Chemistry, v. 140, p. 4498–4506, 2015.

34 TANIMOTO, R. et al. Detection of Temperature Difference in Neuronal Cells. *Scientific Reports*, v. 6, n. 1, p. 22071, 2016.

35 NAKANO, M. et al. Genetically encoded ratiometric fluorescent thermometer with wide range and rapid response. *PLOS ONE*, Public Library of Science, v. 12, n. 2, p. 1–14, 2017.

36 UCHIYAMA, S. et al. A Cell-Targeted Non-Cytotoxic Fluorescent Nanogel Thermometer Created with an Imidazolium-Containing Cationic Radical Initiator. *Angewandte Chemie International Edition*, v. 57, n. 19, p. 5413–5417, 2018.

37 SATO, M. et al. Temperature Changes in Brown Adipocytes Detected with a Bimaterial Microcantilever. *Biophysical Journal*, Elsevier, v. 106, n. 11, p. 2458–2464, 2014.

38 YANG, F. et al. Measurement of local temperature increments induced by cultured HepG2 cells with micro-thermocouples in a thermally stabilized system. *Scientific Reports*, v. 7, n. 1, p. 1721, 2017.

39 RAJAGOPAL, M. C. et al. Transient heat release during induced mitochondrial proton uncoupling. *Communications Biology*, v. 2, n. 1, p. 279, 2019.

40 BAFFOU, G. et al. A critique of methods for temperature imaging in single cells. *Nature Methods*, v. 11, n. 9, p. 899–901, 2014.

41 KIYONAKA, S. et al. Validating subcellular thermal changes revealed by fluorescent thermosensors. *Nature Methods*, v. 12, n. 9, p. 801–802, 2015.

42 SUZUKI, M. et al. The 10^5 gap issue between calculation and measurement in single-cell thermometry. *Nature Methods*, Springer Science and Business Media LLC, v. 12, n. 9, p. 802–803, 2015.

43 BAFFOU, G. et al. Reply to: "Validating subcellular thermal changes revealed by fluorescent thermosensors" and "The 10^5 gap issue between calculation and measurement in single-cell thermometry". *Nature Methods*, Springer Science and Business Media LLC, v. 12, n. 9, p. 803–803, 2015.

44 UCHIYAMA, S. et al. Intracellular temperature measurements with fluorescent polymeric thermometers. *Chem. Commun.*, The Royal Society of Chemistry, v. 53, p. 10976–10992, 2017.

45 BRITES, C. D. S.; BALABHADRA, S.; CARLOS, L. D. Lanthanide-Based Thermometers: At the Cutting-Edge of Luminescence Thermometry. *Advanced Optical Materials*, v. 7, n. 5, p. 1801239, 2019.

46 MCCUMBER, D. E.; STURGE, M. D. Linewidth and Temperature Shift of the R Lines in Ruby. *Journal of Applied Physics*, v. 34, n. 6, p. 1682–1684, 1963.

47 YEN, W. M.; SCOTT, W. C.; SCHAWLOW, A. L. Phonon-Induced Relaxation in Excited Optical States of Trivalent Praseodymium in LaF_3. *Phys. Rev.*, American Physical Society, v. 136, p. A271–A283, 1964.

48 KUSHIDA, T. Linewidths and Thermal Shifts of Spectral Lines in Neodymium-Doped Yttrium Aluminum Garnet and Calcium Fluorophosphate. *Phys. Rev.*, American Physical Society, v. 185, p. 500–508, 1969.

49 BARTOLO, B. D. *Optical Interactions in Solids*. 2nd. ed. Toh Tuck Link, Singapore: World Scientific, 2010.

50 LUO, Z.; HUANG, Y. Phonon and spectral line. In: ____. *Physics of Solid-State Laser Materials*. Singapore: Springer Singapore, 2020. p. 161–202.

51 KITTEL, C. Phonons I. Crystal Vibrations. In: ____. *Introduction to Solid State Physics*. 8th. ed. USA: John Willey & Sons, 2005. p. 89–104.

52 CHEN, X.; Di Bartolo, B. Phonon effects on sharp luminescence lines of Nd^{3+} in $Gd_3Sc_2Ga_3O_{12}$ garnet (GSGG). *Journal of Luminescence*, v. 54, n. 5, p. 309–318, 1993.

53 BILIR, G. et al. Fabrication and spectral investigation of Y_2O_3:Nd^{3+} nanoparticles. *Applied Physics A*, v. 115, n. 1, p. 263–273, 2014.

54 POSENER, D. W. The Shape of Spectral Lines: Tables of the Voigt Profile. *Australian Journal of Physics*, v. 12, n. 2, p. 184–196, 1959.

55 PFISTNER, C. et al. Thermal dependence of fluorescence lines of Er^{3+} in $YAlO_3$. *Physics Letters A*, v. 137, n. 9, p. 457–462, 1989.

56 MONCORGE, R.; PACHECO, D.; BARTOLO, B. D. Thermal behavior of the shape and width of the 9145Å laser line of Nd^{3+} in $CaWO_4$. *physica status solidi (a)*, v. 43, n. 1, p. K45–K48, 1977.

57 DANKO, J.; PACHECO, D.; BARTOLO, B. D. Thermal behavior of the position and width of the 10488Å line of Nd^{3+} in $RbMnF_3$. *physica status solidi (a)*, v. 63, n. 1, p. K31–K34, 1981.

58 KOLESNIKOV, I. E. et al. Bifunctional heater-thermometer Nd^{3+}-doped nanoparticles with multiple temperature sensing parameters. *Nanotechnology*, IOP Publishing, v. 30, n. 14, p. 145501, 2019.

59 SARDAR, D. K.; YOW, R. M.; SALINAS, F. S. Stark components of lower-lying manifolds and phonon effects on sharp spectral lines for inter-Stark transitions of Nd^{3+} in LLGG crystal host. *Optical Materials*, v. 18, n. 3, p. 301–308, 2001.

60 SARDAR, D. K.; YOW, R. M. Optical characterization of inter-Stark energy levels and effects of temperature on sharp emission lines of Nd^{3+} in $CaZn_2Y_2Ge_3O_{12}$. *Optical Materials*, v. 10, n. 3, p. 191–199, 1998.

61 BALAC, S. WGMode : A Matlab toolbox for whispering gallery modes volume computation in spherical optical micro-resonators. *Computer Physics Communications*, v. 243, p. 121–134, 2019.

62 STRATTON, J. A. Boundary-value problems. In: ____. *Electromagnetic Theory*. [S.l.]: John Wiley & Sons, Ltd, 2015. cap. IX, p. 482–599.

63 OLVER, F. et al. *The NIST Handbook of Mathematical Functions*. New York, NY: Cambridge University Press, 2010.

64 ABRAMOWITZ, M.; STEGUN, I. *Handbook of Mathematical Functions, With Formulas, Graphs, and Mathematical Tables,*. 9th. ed. New York: Dover Publications, 1970.

65 ATKINSON, K.; HAN, W. *Spherical Harmonics and Approximations on the Unit Sphere: An Introduction*. [S.l.]: Springer, 2012. v. 2044. (Lecture Notes in Mathematics, v. 2044).

66 RIGHINI, G. C. et al. Whispering gallery mode microresonators: Fundamentals and applications. *La Rivista del Nuovo Cimento*, v. 34, n. 7, p. 435—488, 2011.

67 ORAEVSKY, A. N. Whispering-gallery waves. *Quantum Electronics*, v. 32, n. 5, p. 377–400, 2002.

68 GÖTZINGER, S. *Controlled Coupling of a Single Nanoparticle to a High-Q Microsphere Resonator*. 125 f. Tese (Doctor rerum naturalium) — Mathematisch–Naturwissenschaftlichen Fakultät I der Humboldt-Universität zu Berlin, Berlin, 2003.

69 ZERAOULIA, E.; SPROTT, J. C. *Frontiers in the Study of Chaotic Dynamical Systems with Open Problems*. Singapore: WORLD SCIENTIFIC, 2011.

70 MALITSON, I. H. Interspecimen comparison of the refractive index of fused silica. *J. Opt. Soc. Am.*, v. 55, n. 10, p. 1205–1209, 1965.

71 SCHILLER, S.; BYER, R. L. High-resolution spectroscopy of whispering gallery modes in large dielectric spheres. *Opt. Lett.*, v. 16, n. 15, p. 1138–1140, 1991.

72 GORODETSKY, M.; ILCHENKO, V. High-Q optical whispering-gallery microresonators: precession approach for spherical mode analysis and emission patterns with prism couplers. *Opt. Commun.*, v. 113, n. 1, p. 133–143, 1994.

73 BRAGINSKY, V.; GORODETSKY, M.; ILCHENKO, V. Quality-factor and nonlinear properties of optical whispering-gallery modes. *Physics Letters A*, v. 137, n. 7, p. 393–397, 1989.

74 GORODETSKY, M. L.; PRYAMIKOV, A. D.; ILCHENKO, V. S. Rayleigh scattering in high-q microspheres. *J. Opt. Soc. Am. B*, v. 17, n. 6, p. 1051–1057, 2000.

75 GORODETSKY, M. L.; SAVCHENKOV, A. A.; ILCHENKO, V. S. Ultimate q of optical microsphere resonators. *Opt. Lett.*, OSA, v. 21, n. 7, p. 453–455, 1996.

76 PAZ-BUCLATIN, F. et al. Fluorescence intensity ratio and whispering gallery mode techniques in optical temperature sensors: comparative study. *Opt. Mater. Express*, v. 9, n. 10, p. 4126–4137, 2019.

77 MARTÍN, L. L. et al. Whispering gallery modes in a glass microsphere as a function of temperature. *Opt. Express*, v. 19, n. 25, p. 25792–25798, 2011.

78 MICHAELIS, J. et al. Optical microscopy using a single-molecule light source. *Nature*, v. 405, n. 6784, p. 325–328, May 2000.

79 KALKBRENNER, T. et al. A single gold particle as a probe for apertureless scanning near-field optical microscopy. *Journal of Microscopy*, v. 202, n. 1, p. 72–76, 2001.

80 GÖTZINGER, S.; BENSON, O.; SANDOGHDAR, V. Influence of a sharp fiber tip on high-q modes of a microsphere resonator. *Opt. Lett.*, OSA, v. 27, n. 2, p. 80–82, 2002.

81 COX, A. J.; DEWEERD, A. J.; LINDEN, J. An experiment to measure mie and rayleigh total scattering cross sections. *American Journal of Physics*, v. 70, n. 6, p. 620–625, 2002.

82 BURGHARDT, T. P.; THOMPSON, N. L. Evanescent Intensity Of A Focused Gaussian Light Beam Undergoing Total Internal Reflection In A Prism. *Optical Engineering*, v. 23, n. 1, p. 62–67, 1984.

83 PATIMISCO, P. et al. Analysis of the electro-elastic properties of custom quartz tuning forks for optoacoustic gas sensing. *Sensors and Actuators B: Chemical*, v. 227, p. 539–546, 2016.

84 SARID, D. Mechanical properties of levers. In: ____. *Scanning Force Microscopy With Applications to Electric, Magnetic and Atomic Forces*. Revised edition. New York: Oxford University Press, 1994. cap. 1, p. 1–17.

85 CHRISTEN, M. Air and gas damping of quartz tuning forks. *Sensors and Actuators*, v. 4, p. 555–564, 1983.

86 PATIMISCO, P. et al. A quartz enhanced photo-acoustic gas sensor based on a custom tuning fork and a terahertz quantum cascade laser. *Analyst*, The Royal Society of Chemistry, v. 139, p. 2079–2087, 2014.

87 KIM, J. et al. Effective stiffness of qplus sensor and quartz tuning fork. *Ultramicroscopy*, v. 141, p. 56–62, 2014.

88 CTISTIS, G. et al. Controlling the quality factor of a tuning-fork resonance between 9 and 300K for scanning-probe microscopy. *Journal of Physics D: Applied Physics*, v. 44, n. 37, p. 375502, 2011.

89 ZHANG, X.; GAO, F.; LI, X. Sensing Performance Analysis on Quartz Tuning Fork-Probe at the High Order Vibration Mode for Multi-Frequency Scanning Probe Microscopy. *Sensors (Basel)*, v. 18, n. 2, p. 336, 2018.

90 ORIA, R. et al. Finite Element Analysis of Electrically Excited Quartz Tuning Fork Devices. *Sensors*, v. 13, n. 6, p. 7156–7169, 2013.

91 EBERLY, D. *Least Squares Fitting of Data by Linear or Quadratic Structures*. 2018. Disponível em: <https://www.geometrictools.com/Documentation/LeastSquaresFitting.pdf>. Acesso em: 7 out. 2019.

92 HERCHER, M. The spherical mirror fabry-perot interferometer. *Appl. Opt.*, OSA, v. 7, n. 5, p. 951–966, May 1968.

93 HERCHER, M. Errata: The spherical mirror fabry-perot interferometer. *Appl. Opt.*, OSA, v. 7, n. 7, p. 1336, Jul 1968.

94 JOHNSON, J. R. A high resolution scanning confocal interferometer. *Appl. Opt.*, OSA, v. 7, n. 6, p. 1061–1072, Jun 1968.

95 ZHI, Y.; VALENTA, J.; MELDRUM, A. Structure of whispering gallery mode spectrum of microspheres coated with fluorescent silicon quantum dots. *J. Opt. Soc. Am. B*, v. 30, n. 11, p. 3079–3085, Nov 2013.

96 GALVÃO, R. et al. Fluorescence Intensity Ratio-based temperature sensor with single Nd^{3+}:Y_2O_3 nanoparticles: Experiment and theoretical modeling. *Nano Select*, v. 2, n. 2, p. 346–356, 2021.

97 GOMES, M. A. et al. Temperature-sensitive luminescence of Y_2O_3:Nd^{3+} nanocrystals produced by an eco-friendly route. *Opt. Mater.*, v. 89, p. 536–542, 2019.

98 KOLESNIKOV, I. et al. Nd^{3+}-doped YVO_4 nanoparticles for luminescence nanothermometry in the first and second biological windows. *Sens. Actuators, B*, v. 235, p. 287–293, 2016.

99 BENAYAS, A. et al. Nd:YAG Near-Infrared Luminescent Nanothermometers. *Adv. Opt. Mater.*, v. 3, n. 5, p. 687–694, 2015.

100 ROCHA, U. et al. Subtissue Thermal Sensing Based on Neodymium-Doped LaF_3 Nanoparticles. *ACS Nano*, American Chemical Society, v. 7, n. 2, p. 1188–1199, 2013.

101 WAWRZYNCZYK, D. et al. Neodymium(iii) doped fluoride nanoparticles as non-contact optical temperature sensors. *Nanoscale*, The Royal Society of Chemistry, v. 4, p. 6959–6961, 2012.

102 SUTA, M. et al. Making Nd^{3+} a Sensitive Luminescent Thermometer for Physiological Temperatures—An Account of Pitfalls in Boltzmann Thermometry. *Nanomaterials*, v. 10, n. 3, 2020.

103 CESARIA, M. et al. Incandescent Lamp-Like White-Light Emission from Doped and Undoped Oxide Nanopowders. In: BARTOLO, B. D.; COLLINS, J.; SILVESTRI, L. (Ed.). *Nano-Structures for Optics and Photonics*. Dordrecht: Springer Netherlands, 2015. p. 273–284.

104 SUKUL, P. P.; KUMAR, K. Near-infrared (808 and 980 nm) excited photoluminescence study in Nd-doped Y_2O_3 phosphor for bio-imaging. *Methods Appl. Fluoresc.*, IOP Publishing, v. 4, n. 4, p. 044005, 2016.

105 HOU, X. et al. Effect of Nd concentration on structural and optical properties of Nd:Y_2O_3 transparent ceramic. *J. Lumin.*, v. 131, n. 9, p. 1953–1958, 2011.

106 MAYRINCK, C. de et al. Spherical–shaped Y_2O_3:Eu^{3+} nanoparticles with intense photoluminescence emission. *Ceram. Int.*, v. 41, n. 1, Part B, p. 1189–1195, 2015.

107 GEITENBEEK, R. G. et al. Chemically and thermally stable lanthanide-doped Y_2O_3 nanoparticles for remote temperature sensing in catalytic environments. *Chem. Eng. Sci.*, v. 198, p. 235–240, 2019.

108 ABE, S. et al. Photophysical Properties and Biocompatibility of Photoluminescent Y_2O_3:Eu Nanoparticles in Polymethylmetacrylate Matrix. *J. Nanosci. Nanotechnol.*, v. 14, n. 4, p. 2891–2894, 2014.

109 POLLNAU, M. et al. Power dependence of upconversion luminescence in lanthanide and transition-metal-ion systems. *Phys. Rev. B*, v. 61, p. 3337–3346, 2000.

110 AUZEL, F. Upconversion and Anti-Stokes Processes with f and d Ions in Solids. *Chem. Rev.*, v. 104, n. 1, p. 139–174, 2004.

111 JAQUE, D.; VETRONE, F. Luminescence nanothermometry. *Nanoscale*, The Royal Society of Chemistry, v. 4, p. 4301–4326, 2012.

112 ELDRIDGE, J. I. Luminescence decay-based Y_2O_3:Er phosphor thermometry: Temperature sensitivity governed by multiphonon emission with an effective phonon energy transition. *J. Lumin.*, v. 214, p. 116535, 2019.

113 PÉREZ-RODRÍGUEZ, C. et al. Relevance of radiative transfer processes on Nd^{3+} doped phosphate glasses for temperature sensing by means of the fluorescence intensity ratio technique. *Sens. Actuators, B*, v. 195, p. 324–331, 05 2014.

114 MENEZES, L. de S.; ARAÚJO, C. B. de. Optically Detected Thermal Effects in Rare-Earth Doped Materials for Host Characterization, Thermometric Devices, Nanothermometry and Biothermometry. *J. Braz. Chem. Soc.*, v. 26, p. 2405–2417, 12 2015.

115 SOHN, S. et al. Synthesis and characterization of near-monodisperse yttria particles by homogeneous precipitation method. *Powder Technol.*, v. 142, n. 2, p. 136–153, 2004.

116 LIMA, K. de O. et al. Influence of defects on sub-Å optical linewidths in Eu^{3+}:Y_2O_3 particles. *J. Lumin.*, v. 168, p. 276–282, 2015.

117 KOLESNIKOV, I. et al. Synthesis and characterization of Y_2O_3:Nd^{3+} nanocrystalline powders and ceramics. *Opt. Mater.*, v. 75, p. 680–685, 2018.

118 OSIPOV, V. V. et al. Raman scattering and luminescence of yttria nanopowders and ceramics. *Opt. Spectrosc.*, v. 116, n. 6, p. 946–955, 2014.

119 SKANDAN, G. et al. Phase characterization and stabilization due to grain size effects of nanostructured Y_2O_3. *Nanostruct. Mater.*, v. 1, n. 4, p. 313–322, 1992.

120 LAVERSENNE, L. et al. Optimization of spectroscopic properties of Yb^{3+}-doped refractory sesquioxides: cubic Y_2O_3,Lu_2O_3 and monoclinic Gd_2O_3. *Opt. Mater.*, v. 16, n. 4, p. 475–483, 2001.

121 MENEZES, L. de S. et al. Frequency upconversion in Nd^{3+}–doped fluoroindate glass. *J. Non-Cryst. Solids*, v. 213–214, p. 256–260, 1997.

122 MENEZES, L. de S. et al. Continuous wave ultraviolet frequency upconversion due to triads of Nd^{3+} ions in fluoroindate glass. *Appl. Phys. Lett.*, v. 70, p. 683–685, 1997.

123 GOMES, A. S. L. et al. Rare-earth doped fluoroindate glasses: glass formation, energy transfer properties and frequency upconversion. *Trends in Chemical Physics*, v. 4, p. 59–74, 1996.

124 ARAÚJO, C. B. de et al. Frequency upconversion in rare-earth doped fluoroindate glasses. *C. R. Chim.*, v. 5, n. 12, p. 885–898, 2002.

125 CAMARGO, K. C. et al. Continuous wave near-infrared phonon-assisted upconversion in single Nd^{3+}–doped yttria nanoparticles. *J. Lumin.*, v. 192, p. 963–68, 2017.

126 SARDAR, D.; STUBBLEFIELD, S. Temperature dependencies of linewidths, positions, and line shifts of spectral transitions of trivalent neodymium ions in barium magnesium yttrium germanate laser host. *J. Appl. Phys*, v. 83, p. 1195–1199, 02 1998.

127 CHANG, N. C. et al. Optical spectra, energy levels, and crystal-field analysis of tripositive rare earth ions in Y_2O_3. I. Kramers ions in C_2 sites. *J. Chem. Phys*, v. 76, n. 8, p. 3877–3889, 1982.

128 QUINTANILLA, M. et al. Luminescent Nanothermometry with Lanthanide–doped Nanoparticles. In: CARLOS, L. D.; PALACIO, F. (Ed.). *Thermometry at the Nanoscale: Techniques and Selected Applications*. London: The Royal Society of Chemistry, 2016. cap. 5, p. 124–166.

129 SKRIPKA, A. et al. Advancing neodymium single-band nanothermometry. *Nanoscale*, The Royal Society of Chemistry, v. 11, p. 11322–11330, 2019.

130 KOLESNIKOV, I. et al. Y_2O_3:Nd^{3+} nanocrystals as ratiometric luminescence thermal sensors operating in the optical windows of biological tissues. *J. Lumin.*, v. 204, p. 506–512, 2018.

131 YANG, X. et al. Flame-made Y_2O_3:Yb^{3+}/Er^{3+} upconversion nanoparticles: Mass production synthesis, multicolor tuning and thermal sensing studies. *J. Alloys Compd.*, v. 854, p. 157078, 2021.

132 LOJPUR, V.; NIKOLIĆ, G.; DRAMIĆANIN, M. D. Luminescence thermometry below room temperature via up-conversion emission of Y_2O_3:Yb^{3+},Er^{3+} nanophosphors. *J. Appl. Phys*, v. 115, n. 20, p. 203106, 2014.

133 CHEN, G. et al. Optical temperature sensing behavior of Er^{3+}/Yb^{3+}/Tm^{3+}:Y_2O_3 nanoparticles based on thermally and non-thermally coupled levels. *Opt. Commun.*, v. 407, p. 57–62, 2018.

134 LI, P. et al. Investigation on the Fluorescence Intensity Ratio Sensing Thermometry Based on Nonthermally Coupled Levels. *ACS Appl. Bio Mater.*, v. 2, n. 4, p. 1732–1739, 2019.

135 KOLESNIKOV, I. E. et al. YVO_4:Nd^{3+} nanophosphors as NIR-to-NIR thermal sensors in wide temperature range. *Sci. Rep.*, v. 7, n. 1, p. 18002, 2017.

136 TIAN, X. et al. Temperature sensor based on ladder-level assisted thermal coupling and thermal-enhanced luminescence in $NaYF_4$: Nd^{3+}. *Opt. Express*, OSA, v. 22, n. 24, p. 30333–30345, 2014.

137 MENEZES, L. de S. et al. Thermally enhanced frequency upconversion in Nd^{3+}-doped fluoroindate glass. *J. Appl. Phys*, v. 90, n. 9, p. 4498–4501, 2001.

138 MARQUES, M. S. et al. Giant enhancement of phonon-assisted one-photon excited frequency upconversion in a Nd^{3+}-doped tellurite glass. *J. Appl. Phys*, v. 113, n. 5, p. 053102, 2013.

139 AUZEL, F. Multiphonon Interaction of Excited Luminescent Centers in the Weak Coupling Limit: Non Radiative Decay and Multiphonon Side Bands. In: ____. *Luminescence of Inorganic Solids*. Boston, MA: Springer US, 1978. p. 67–113.

140 MENEZES, L. de S. et al. Phonon-assisted cooperative energy transfer and frequency upconversion in a Yb^{3+}/Tb^{3+} codoped fluoroindate glass. *J. Appl. Phys*, v. 94, n. 2, p. 863–866, 2003.

141 AUZEL, F. Multiphonon-assisted anti-Stokes and Stokes fluorescence of triply ionized rare-earth ions. *Phys. Rev. B*, v. 13, p. 2809–2817, 1976.

142 WEBER, M. J. Probabilities for Radiative and Nonradiative Decay of Er^{3+} in LaF_3. *Phys. Rev.*, v. 157, p. 262–272, 1967.

143 WEBER, M. J. Multiphonon Relaxation of Rare-Earth Ions in Yttrium Orthoaluminate. *Phys. Rev. B*, v. 8, p. 54–64, 1973.

144 REISFELD, R. Multiphonon relaxation in glasses. In: ____. *Radiationless Processes*. Boston, MA: Springer US, 1980. p. 489–498.

145 XIONG, J. et al. Real–time micro–scale temperature imaging at low cost based on fluorescent intensity ratio. *Sci. Rep.*, v. 7, n. 1, p. 41311, 2017.

146 MOURA, A. L. et al. Tunable ultraviolet and blue light generation from nd:yab random laser bolstered by second-order nonlinear processes. *Sci. Rep.*, v. 6, n. 1, p. 27107, 2016.

147 GALVÃO, R. et al. Single Er^{3+}/Yb^{3+}-Codoped Yttria Nanocrystals for Temperature Sensing: Experimental Characterization and Theoretical Modeling. *The Journal of Physical Chemistry C*, v. 125, n. 27, p. 14807–14817, 2021.

148 GONÇALVES, I. et al. Phonon-assisted NIR-to-visible upconversion in single β-$NaYF_4$ microcrystals codoped with Er^{3+} and Yb^{3+} for microthermometry applications: Experiment and theory. *J. Lumin.*, v. 231, p. 117801, 2021.

149 HEMMER, E. et al. Exploiting the biological windows: current perspectives on fluorescent bioprobes emitting above 1000 nm. *Nanoscale Horiz.*, v. 1, n. 3, p. 168–184, 2016.

150 ARAÚJO, C. B. de et al. Frequency upconversion in rare-earth doped fluoroindate glasses. *C. R. Chimie*, v. 5, n. 12, p. 885–898, 2002.

151 JIA, M. et al. NIR-II/III Luminescence Ratiometric Nanothermometry with Phonon-Tuned Sensitivity. *Adv. Opt. Mater.*, v. 8, n. 6, p. 1901173, 2020.

152 ARAÚJO, C. B. de et al. Infrared-to-visible CW frequency upconversion in Er^{3+}-doped fluoroindate glasses. *Appl. Phys. Lett.*, v. 68, n. 5, p. 602–604, 1996.

153 MACIEL, G. S. et al. Temperature sensor based on frequency upconversion in Er^{3+}-doped fluoroindate glass. *IEEE Photon. Technol. Lett.*, v. 7, n. 12, p. 1474–1476, 1995.

154 GÓMEZ, L. A. et al. Upconversion luminescence in er^{3+} doped and er^{3+}/yb^{3+} codoped zirconia and hafnia nanocrystals excited at 980 nm. *J. Appl. Phys.*, v. 107, n. 11, p. 113508, 2010.

155 NIGOGHOSSIAN, K. et al. UV and Temperature-Sensing Based on $NaGdF_4$:Yb:Er^{3+}@SiO_2–$Eu(tta)_3$. *ACS Omega*, v. 2, n. 5, p. 2065–2071, 2017.

156 AIKEN, B.; MATIJEVIĆ, E. Preparation and properties of uniform coated inorganic colloidal particles. iv. yttrium basic carbonate and yttrium oxide on hematite. *J. Colloid Interface Sci.*, v. 126, n. 2, p. 645–649, 1988.

157 RAY, S. et al. Optical properties of nanocrystalline Y_2O_3:Eu^{3+}. *J. Appl. Phys.*, v. 97, n. 9, p. 094312, 2005.

158 TEITELBOIM, A. et al. Energy Transfer Networks within Upconverting Nanoparticles Are Complex Systems with Collective, Robust, and History-Dependent Dynamics. *J. Phys. Chem. C*, v. 123, n. 4, p. 2678–2689, 2019.

159 HONG-WEI, S. et al. Upconversion Luminescence Dynamics in Er^{3+}/Yb^{3+} Codoped Nanocrystalline Yttria. *Chin. Phys. Lett.*, v. 23, n. 2, p. 474–477, 2006.

160 RENERO-LECUNA, C. et al. Origin of the High Upconversion Green Luminescence Efficiency in β-$NaYF_4$:2%Er^{3+},20%Yb^{3+}. *Chem. Mater.*, v. 23, n. 15, p. 3442–3448, 2011.

161 ZHANG, F. Upconversion nanoparticles for thermal sensing. In: *Photon Upconversion Nanomaterials*. [S.l.]: Springer Berlin Heidelberg, 2014. p. 343–374.

162 AARTS, L.; ENDE, B. M. van der; MEIJERINK, A. Downconversion for solar cells in $NaYF_4$:Er,Yb. *J. Appl. Phys*, v. 106, n. 2, p. 023522, 2009.

163 YU, W. et al. Temperature-dependent upconversion luminescence and dynamics of $NaYF_4$:Yb^{3+}/Er^{3+} nanocrystals: influence of particle size and crystalline phase. *Dalton Trans.*, v. 43, p. 6139–6147, 2014.

164 GOUVEIA, E. A.; ARAUJO, M. T. d.; GOUVEIA-NETO, A. S. Thermal effects on light emission in Yb^{3+}-sensitized rare-earth doped optical glasses. *Braz. J. Phys.*, v. 31, p. 89–101, 2001.

165 MIANDASHTI, A. R.; KORDESCH, M. E.; RICHARDSON, H. H. Effect of Temperature and Gold Nanoparticle Interaction on the Lifetime and Luminescence of $NaYF_4$:Yb^{3+}:Er^{3+} Upconverting Nanoparticles. *ACS Photonics*, v. 4, n. 7, p. 1864–1869, 2017.

166 ZHAO, J. et al. Upconversion luminescence with tunable lifetime in $NaYF_4$:Yb,Er nanocrystals: role of nanocrystal size. *Nanoscale*, v. 5, p. 944–952, 2013.

167 JIE, G. et al. Energy transfer and frequency upconversion in Er^{3+}-Yb^{3+} codoped oxy-fluoro-tungstosilicate glasses. *J. Rare Earths*, v. 30, n. 5, p. 422–425, 2012.

168 FREJ, M. L. et al. Stokes and anti-Stokes luminescence of Er^{3+} doped $Ga_{10}Ge_{25}S_{65}$ glass excited at 980 and 532 nm. *J. Appl. Phys.*, v. 108, n. 9, p. 093514, 2010.

169 SUTA, M. et al. Making Nd^{3+} a Sensitive Luminescent Thermometer for Physiological Temperatures–An Account of Pitfalls in Boltzmann Thermometry. *Nanomaterials*, MDPI AG, v. 10, n. 3, p. 543, 2020.

170 LI, L. et al. Highly sensitive optical ratiometric thermal sensing based on the three-photon upconversion luminescence of Y_2O_3:Yb^{3+},Er^{3+} nano-thermometers. *J. Mater. Chem. C*, v. 7, p. 7378–7385, 2019.

171 GAVRILOVIĆ, T. V. et al. Multifunctional Eu^{3+}- and Er^{3+}/Yb^{3+}-doped $GdVO_4$ nanoparticles synthesized by reverse micelle method. *Sci. Rep.*, v. 4, n. 1, p. 4209, Feb 2014.

172 ŠEVIĆ, D. et al. Effects of temperature on luminescent properties of Gd_2O_3:Er, Yb nanophosphor. *Opt. Quantum Electron.*, v. 52, n. 5, p. 232, 2020.

173 GETZ, M. N.; NILSEN, O.; HANSEN, P.-A. Sensors for optical thermometry based on luminescence from layered YVO4: Ln^{3+} (Ln = Nd, Sm, Eu, Dy, Ho, Er, Tm, Yb) thin films made by atomic layer deposition. *Sci. Rep.*, v. 9, n. 1, p. 10247, 2019.

174 RAN, W. et al. Infrared excited Er^{3+}/Yb^{3+} codoped $NaLaMgWO_6$ phosphors with intense green up-conversion luminescence and excellent temperature sensing performance. *Dalton Trans.*, v. 48, p. 11382–11390, 2019.

175 MIAO, J. et al. Effect of Yb^{3+} concentration on upconversion luminescence and optical thermometry sensitivity of La_2MoO_6: Yb^{3+}, Er^{3+} phosphors. *Appl. Opt.*, OSA, v. 60, n. 6, p. 1508–1514, 2021.

176 JIA, M. et al. An ultrasensitive luminescent nanothermometer in the first biological window based on phonon-assisted thermal enhancing and thermal quenching. *J. Mater. Chem. C*, v. 8, p. 15603–15608, 2020.

177 LIU, J. et al. Facile synthesis of accordion-like Y_2O_3:Er^{3+} nanothermometers for ratiometric temperature sensing applications. *J. Lumin.*, v. 223, p. 117207, 2020.

178 CORLESS, R. M. et al. On the Lambert W function. *Adv Comput Math*, v. 5, n. 1, p. 329–359, 1996.

179 SUYVER, J. et al. Upconversion spectroscopy and properties of $NaYF_4$ doped with Er^{3+}, Tm^{3+} and/or Yb^{3+}. *J. Lumin.*, v. 117, n. 1, p. 1–12, 2006.

180 ENGLMAN, R.; JORTNER, J. The energy gap law for radiationless transitions in large molecules. *Mol. Phys.*, v. 18, n. 2, p. 145–164, 1970.

181 KENNEDY, J. L. *Investigations of fiber optic temperature sensors based on Yb:$Y_3Al_5O_{12}$*. Tese (Doutorado) — University of South Florida, 2006.

182 RAKOV, N.; MACIEL, G. S. Blue shift of Tm^{3+} upconversion owing to Nd^{3+} in yttrium oxide powders pumped by pulsed red laser. *Chemical Physics Letters*, v. 503, n. 1, p. 124–128, 2011.

183 MOURA, A. L. et al. Nonlinear effects and photonic phase transitions in Nd^{3+}-doped nanocrystal-based random lasers. *Appl. Opt.*, OSA, v. 59, n. 13, p. D155–D162, 2020.

184 LAIA, A. S. et al. Temperature Sensing with Er^{3+} Doped Y_2O_3 Nanoparticles Operating within the 1st and 2nd Biological Window: The Influence of Particle Size on the Relative Sensitivity of Thermally Decoupled Levels. *Available at SSRN 4101142*.

185 HARTMANN, M. *On the Microscopic Limit for the Existence of Local Temperature*. 144 f. Tese (Doctor rerum naturalium) — Universit'at Stuttgart, Stuttgart, 2005.

186 HARTMANN, M.; MAHLER, G.; HESS, O. Gaussian Quantum Fluctuations in Interacting Many Particle Systems. *Letters in Mathematical Physics*, v. 68, n. 2, p. 103–112, 2004.

187 HARTMANN, M.; MAHLER, G.; HESS, O. Spectral Densities and Partition Functions of Modular Quantum systems as Derived from a Central Limit Theorem. *Journal of Statistical Physics*, v. 119, n. 5, p. 1139–1151, 2005.

188 KITTEL, C. Phonons II. Thermal Properties. In: ____. *Introduction to Solid State Physics*. 8th. ed. USA: John Willey & Sons, 2005. p. 105–130.

189 HARTMANN, M.; MAHLER, G.; HESS, O. Local versus global thermal states: Correlations and the existence of local temperatures. *Phys. Rev. E*, American Physical Society, v. 70, p. 066148, 2004.

190 HARTMANN, M.; MAHLER, G.; HESS, O. Existence of Temperature on the Nanoscale. *Phys. Rev. Lett.*, American Physical Society, v. 93, p. 080402, 2004.

191 YANG, L. et al. Synthesis of Eu^{3+} doped Y_2O_3 nanotube arrays through an electric field-assisted deposition method. *Materials Chemistry and Physics*, v. 101, n. 1, p. 195–198, 2007.

192 BAO, H.; RUAN, X. L.; KAVIANY, M. Theory of the broadening of vibrational spectra induced by lowered symmetry in yttria nanostructures. *Phys. Rev. B*, American Physical Society, v. 78, p. 125417, 2008.

193 BARAD, C. et al. Lattice variation of cubic Y_2O_3 in three dimensions: Temperature, pressure and crystal size. *Journal of Alloys and Compounds*, v. 885, p. 161199, 2021.

194 HANIC, F. et al. Real structure of undoped Y_2O_3 single crystals. *Acta Crystallographica Section B*, v. 40, n. 2, p. 76–82, 1984.

APPENDIX A – SIZE LIMITS FOR THE EXISTENCE OF LOCAL TEMPERATURE

To determine on which length scales it's possible to define a local temperature, one can investigate how small the considered parts can be while still allowing for a description with local thermalized states. Since modular structures such as a crystal lattice are typical in the description of solid-state systems, one can consider a system composed of elementary units with short range interactions. Considering a homogeneous chain of elementary quantum subsystems with nearest neighbor interactions, the Hamiltonian can be written as [185]:

$$H = \sum_i H_i + I_{i,i+1} \tag{A.1}$$

where i labels the elementary subsystems. H_i is the i-th subsystem's Hamiltonian and $I_{i,i+1}$ the interaction between the i-th and $(i+1)$-th subsystems. Periodic boundary conditions were assumed. It's possible to form N_G groups of n subsystems each and split the Hamiltonian into two terms:

$$H = H_0 + I \tag{A.2}$$

where H_0 is the sum of the Hamiltonians of the isolated groups through of the operation:

$$(\text{ index } i \to (\mu-1)n + j;\ \mu = 1, \dots, N_G; j = 1, \dots, n) \tag{A.3}$$

Thus:

$$\begin{aligned} H_0 &= \sum_{\mu=1}^{N_G} \mathcal{H}_\mu \quad \text{with} \\ \mathcal{H}_\mu &= \sum_{j=1}^{n} H_{n(\mu-1)+j} + I_{n(\mu-1)+j,n(\mu-1)+j+1} \end{aligned} \tag{A.4}$$

and I contains the interaction terms of each group with its neighbor group:

$$I = \sum_{\mu=1}^{N_G} I_{\mu n, \mu n+1} \tag{A.5}$$

The eigenstates of H_0, $H_0|a\rangle = E_a|a\rangle$, are given by the direct product of the individual group eigenstates:

$$|a\rangle = \prod_{\mu=1}^{N_G} \otimes \left|a_\mu\right\rangle \quad \text{with} \quad \left(\mathcal{H}_\mu - I_{\mu n, \mu n+1}\right)\left|a_\mu\right\rangle = E_\mu \left|a_\mu\right\rangle \tag{A.6}$$

where E_μ is the energy a single subgroup and $E_a = \sum_{\mu=1}^{N_G} E_\mu$. The system can be considered in thermal equilibrium with the density matrix:

$$\hat{\rho} = \frac{e^{-\beta H}}{Z} \tag{A.7}$$

where Z is the partition sum and $\beta = (k_\mathrm{B} T)^{-1}$ is the inverse temperature with Boltzmann's constant k_B and temperature T. Therefore, to verify if a part H_{μ_0} is in a thermal state, one needs to calculate the reduced density matrix and compare it to a local canonical state. In order to perform the necessary trace over all the other parts ($\mu \neq \mu_0$), one needs to represent the global equilibrium state in the basis of the product states $|a\rangle$. Its diagonal elements are:

$$\langle a|\hat{\rho}|a\rangle = \left\langle a \left| \frac{\mathrm{e}^{-\beta H}}{Z} \right| a \right\rangle = \int_{E_0}^{E_1} w_a(E) \frac{\mathrm{e}^{-\beta E}}{Z} dE \tag{A.8}$$

where E_0 is the energy of the ground state and E_1 the upper limit. $w_a(E)$ is the probability of obtaining an energy value between E and $E + \Delta E$ for the total energy of a system in the $|a\rangle$ state, which can be shown to be a Gaussian [186, 187]:

$$\lim_{N_G \to \infty} w_a(E) = \frac{1}{\sqrt{2\pi}\Delta_a} \exp\left(-\frac{\left(E - \bar{E}_a\right)^2}{2\Delta_a^2} \right) \tag{A.9}$$

where $\bar{E}_a$ is the expectation value of H in the $|a\rangle$ state and Δ_a^2 its variance:

$$\begin{aligned} \bar{E}_a &= \langle a|H|a\rangle \quad \text{and} \\ \Delta_a^2 &= \left\langle a \left| H^2 \right| a \right\rangle - \langle a|H|a\rangle^2 \end{aligned} \tag{A.10}$$

Since $\bar{E}_a$ is the sum of the energy eigenvalue of the isolated groups E_a and a term that contains the interactions:

$$\bar{E}_a = E_a + \varepsilon_a \tag{A.11}$$

ε_a and Δ_a^2 can be expressed in terms of the interaction:

$$\begin{aligned} \varepsilon_a &= \langle a|I|a\rangle \quad \text{and} \\ \Delta_a^2 &= \left\langle a \left| I^2 \right| a \right\rangle - \langle a|I|a\rangle^2 \end{aligned} \tag{A.12}$$

Therefore ε_a is the expectation value and Δ_a^2 the squared width of the interactions in the state $|a\rangle$. Using Equation A.9 to calculate the integral in Equation A.8, one gets:

$$\begin{aligned} \langle a|\rho|a\rangle =& \frac{1}{Z} \exp\left(-\beta \left(E_a + \varepsilon_a\right) + \frac{\beta^2 \Delta_a^2}{2} \right) \\ & \times \frac{1}{2} \left[\operatorname{erfc}\left(\frac{E_0 - E_a - \varepsilon_a - \beta\Delta_a^2}{\sqrt{2}\Delta_a} \right) - \operatorname{erfc}\left(\frac{E_1 - E_a - \varepsilon_a + \beta\Delta_a^2}{\sqrt{2}\Delta_a} \right) \right] \end{aligned} \tag{A.13}$$

where $\mathrm{erfc}(x)$ is the Gaussian error function:

$$\mathrm{erfc}(x) = \frac{2}{\sqrt{\pi}} \int_x^\infty \mathrm{e}^{-s^2} ds \tag{A.14}$$

the second error function appears only if the energy has an upper limit. Since that the arguments of the error function grow as $\sqrt{N_\mathrm{G}}$ or faster, an asymptotic expansion [64] can be used for $N_\mathrm{G} \gg 1$:

$$\mathrm{erfc}(x) \approx \begin{cases} \frac{\exp(-x^2)}{\sqrt{\pi}x} & \text{for} \quad x \to \infty \\ 2 + \frac{\exp(-x^2)}{\sqrt{\pi}x} & \text{for} \quad x \to -\infty \end{cases} \tag{A.15}$$

Inserting this approximation into Equation A.13, it follows that the second conjugate error function, which contains the upper bound of the energy spectrum, can be neglected when compared to the first one, which contains the ground state. For the same reason, the normalization constant in Equation A.9 is valid even if the energy range doesn't extend over the entire real values.

Equation A.13 thus reads:

$$\langle a|\hat{\rho}|a\rangle = \begin{cases} \frac{1}{Z} \exp\left[-\beta\left(E_a + \varepsilon_a - \frac{\beta\Delta_a^2}{2}\right)\right] & \text{for} \quad \frac{E_0 - E_a - \varepsilon_a + \beta\Delta_a^2}{\sqrt{2N_G}\Delta_a} < 0 \\ \frac{\exp\left(-\beta E_0 - \frac{(E_a + \varepsilon_a - E_0)^2}{2\Delta_a^2}\right)}{\sqrt{2\pi} Z \frac{E_0 - E_a - \varepsilon_a + \beta\Delta_a^2}{\Delta_a}} & \text{for} \quad \frac{E_0 - E_a - \varepsilon_a + \beta\Delta_a^2}{\sqrt{2N_G}\Delta_a} > 0 \end{cases} \tag{A.16}$$

The off-diagonal elements $\langle a|\hat{\rho}|b\rangle$ vanish for $|E_a - E_b| > \Delta_a + \Delta_b$ because the overlap of the two Gaussian distributions is negligible. For $|E_a - E_b| < \Delta_a + \Delta_b$, the transformation involves an integral over frequencies and thus these terms are also negligible when compared to the diagonal ones. It's now necessary to test under what conditions the density matrix $\hat{\rho}$ can be approximated by a product of canonical density matrices with temperature β_loc for each subgroup. One needs to verify whether the logarithm of Equation A.16 is a linear function of the energy:

$$\ln(\langle a|\hat{\rho}|a\rangle) \approx -\beta_\mathrm{loc} E_a + c \tag{A.17}$$

where β_loc and c are constants. It's worth commenting that Equation A.17 does not imply that the occupation probability of an eigenstate $|\varphi\rangle$ with energy E_φ and a product state $|a\rangle$ with the same energy $E_a \approx E_\varphi$ are equal. For $(\beta_\mathrm{loc} > 0)$, Equation A.17 is only valid for:

$$\frac{E_a + \varepsilon_a - E_0}{\sqrt{N_G}\Delta_a} > \beta \frac{\Delta_a^2}{\sqrt{N_G}\Delta_a} \tag{A.18}$$

and:

$$-\varepsilon_a + \frac{\beta}{2}\Delta_a^2 \approx c_1 E_a + c_2 \tag{A.19}$$

where c_1 and c_2 are constants. Temperature thus becomes intensive if the constant c_1 becomes negligible. Otherwise, temperature would not be intensive, although it might exist locally. To

ensure that the density matrix of each subgroup is approximately canonical, Equation A.19 must be valid for each subgroup:

$$-\frac{\varepsilon_{\mu-1}+\varepsilon_{\mu}}{2}+\frac{\beta}{4}\left(\Delta_{\mu-1}^{2}+\Delta_{\mu}^{2}\right)+\frac{\beta}{6}\tilde{\Delta}_{\mu}^{2}\approx c_{1}E_{\mu}+c_{2} \tag{A.20}$$

where $\varepsilon_{\mu}=\left\langle a\left|I_{\mu n,\mu n+1}\right|a\right\rangle$ with $\varepsilon_{a}=\sum_{\mu=1}^{N_G}\varepsilon_{\mu}$ and:

$$\begin{aligned}\Delta_{\mu}^{2}&=\left\langle a\left|\mathcal{H}_{\mu}^{2}\right|a\right\rangle-\left\langle a\left|\mathcal{H}_{\mu}\right|a\right\rangle^{2}\ \text{and}\\ \tilde{\Delta}_{\mu}^{2}&=\sum_{\nu=\mu-1}^{\mu+1}\left\langle a\left|\mathcal{H}_{\nu-1}\mathcal{H}_{\nu}+\mathcal{H}_{\nu}\mathcal{H}_{\nu-1}\right|a\right\rangle-2\left\langle a\left|\mathcal{H}_{\nu-1}\right|a\right\rangle\left\langle a\left|\mathcal{H}_{\nu}\right|a\right\rangle\end{aligned} \tag{A.21}$$

It is thus sufficient to satisfy Equations A.18 and A.20 for an energy range $E_{\min}\leq E_{\mu}\leq E_{\max}$. The density of states for a large many body system is typically a rapidly growing function of the energy. On the other hand, if the system is in thermal equilibrium, the occupation probabilities decay exponentially with the energy. The product of these two functions thus gives a peak at the expectation value of the energy ($\bar{E}$). Therefore, a suitable energy range should be centered at this peak and large enough to sufficiently cover it. On the other hand it must not be larger than the range of values E_{μ} can take on. A suitable choice for $E_{\min}$ and $E_{\max}$ is thus:

$$\begin{aligned}E_{\min}&=\max\left(\left[E_{\mu}\right]_{\min},\frac{1}{\alpha}\frac{\bar{E}}{N_G}+\frac{E_0}{N_G}\right)\\ E_{\max}&=\min\left(\left[E_{\mu}\right]_{\max},\alpha\frac{\bar{E}}{N_G}+\frac{E_0}{N_G}\right)\end{aligned} \tag{A.22}$$

where $\alpha\gg 1$ is a scaling parameter for the energy range and $\bar{E}$ will depend on the global temperature. $\left[E_{\mu}\right]_{\min}$ and $\left[E_{\mu}\right]_{\max}$ are the minimal and maximal values E_{μ} can take on.

Now that the basic requirements for the existence of a local temperature were outlined, it's possible to apply this theory to simple systems, such as a harmonic chain. For a chain of $N_G\cdot n$ particles of mass m and spring constant $\sqrt{m}\omega_0$, the Hamiltonian in Equation A.1 reads:

$$\begin{aligned}H_i&=\frac{m}{2}p_i^2+\frac{m}{2}\omega_0^2q_i^2\\ I_{i,i+1}&=-m\omega_0^2q_iq_{i+1}\end{aligned} \tag{A.23}$$

where p_i is the momentum of the particle at site i and q_i the displacement from its equilibrium position $i\cdot a_0$ with a_0 being the distance between neighboring particles at equilibrium.

The Hamiltonian of each group can be diagonalized by a Fourier transform:

$$E_a=\sum_{\mu=1}^{N_{\mathrm{G}}}E_{\mu}\quad\text{with}\quad E_{\mu}=\sum_{k}\omega_k\left(n_k^a(\mu)+\frac{1}{2}\right) \tag{A.24}$$

where $k=\pi l/\left(a_0(n+1)\right)$ $(l=1,2,\ldots,n)$ and the frequencies ω_k are given by:

$$\omega_k^2 = 4\omega_0^2 \sin^2\left(\frac{ka_0}{2}\right) \tag{A.25}$$

$n_k^a(\mu)$ is the occupation number of mode k of group μ in the state $|a\rangle$. Units of $\hbar = 1$ were chosen for simplicity.

The expectation values of the group interactions are null ($\varepsilon_\mu = 0$), while the widths Δ_μ^2 depend on the occupation numbers n_k and on the energies E_μ. In order to apply Equations A.18 and A.20, it's possible to use the Debye approximation [188]. The approximation requires that $n \gg 1$, $a_0 \ll l$, where $l = na_0$ and the length of the chain to be finite. Following this approximation, one gets $\omega_k = vk$ with the velocity of sound $v = \omega_0 a_0$ and $\cos(ka_0/2) \approx 1$. The width of the group interaction is thus:

$$\Delta_\mu^2 = \frac{4}{n^2} E_\mu E_{\mu+1} \tag{A.26}$$

where the approximation $n + 1 \approx n$ was used. The relevant energy scale arises from the thermal expectation value of the entire chain:

$$\bar{E} = N_G n k_B \Theta \left(\frac{T}{\Theta}\right)^2 \int_0^{\Theta/T} \frac{x}{e^x - 1} dx \tag{A.27}$$

and the ground state energy is given by:

$$E_0 = N_G n k_B \Theta \left(\frac{T}{\Theta}\right)^2 \int_0^{\Theta/T} \frac{x}{2} dx = \frac{N_G n k_B \Theta}{4} \tag{A.28}$$

and Θ is the Debye temperature [188]. For the first criterion, Equation A.18, for a given $E_a = \sum_\mu E_\mu$, Δ_μ^2 is largest if $\tilde{E} \equiv E_\mu \forall \mu$. Therefore, Equation A.18 becomes:

$$\tilde{E} - \frac{E_0}{N_G} - \frac{4\beta}{n^2}\tilde{E}^2 > 0 \tag{A.29}$$

which sets a lower limit on n. For temperatures where $\bar{E} < E_0$, this bound is strongest for low energies $\tilde{E}$ and for $\bar{E} > E_0$, it is strongest for high energies $\tilde{E}$. Since Equation A.20 gives a more strict criterion than Equation A.18 for $\bar{E} > E_0$, only Equation A.29 is considered for $\bar{E} < E_0$. In this range, Equation A.29 is hardest to satisfy for low energies ($\tilde{E} = \left(\bar{E}/\alpha N_G\right) + (E_0/N_G)$). Therefore, the lower limit for n is given by:

$$n > \frac{\Theta}{T}\frac{\alpha}{4\bar{e}}\left(\frac{4\bar{e}}{\alpha} + 1\right)^2 \tag{A.30}$$

where $\bar{e} = \bar{E}/\left(nN_G k_B \Theta\right)$. To test the condition of Equation A.20, taking the derivative with respect to E_μ on both sides, one gets:

$$\frac{\beta}{n^2}\left(E_{\mu-1} + E_{\mu+1} - 2\frac{E_0}{N_G}\right) + \frac{2\beta}{n^2}\frac{E_0}{N_G} \approx c_1 \tag{A.31}$$

Since the energy dependent term must be much smaller than one:

$$\frac{\beta}{n^2}\left(E_{\mu-1}+E_{\mu+1}-2\frac{E_0}{N_G}\right)\leq\delta\ll 1 \tag{A.32}$$

which is hardest to fulfill for high energies $E_{\mu-1}$ and $E_{\mu+1}$. Thus, taking $E_{\mu-1}$ and $E_{\mu+1}$ equal to the upper bound of the range in Equation A.22:

$$n>\frac{2\alpha}{\delta}\frac{\Theta}{T}\bar{e} \tag{A.33}$$

where the accuracy parameter $\delta\ll 1$ quantifies the value of the energy dependent part. Since the constant part in the left hand-side of Equation A.32 satisfies:

$$\frac{2\beta}{n^2}\frac{E_0}{N_G}<\frac{\sqrt{\delta}}{\alpha}\left(\frac{1}{\sqrt{2}}-\frac{\sqrt{\delta}}{\alpha}\right)\ll 1 \tag{A.34}$$

and from Equation A.19, the temperature becomes intensive if the constant c_1 vanishes:

$$|c_1|\ll 1 \quad\Rightarrow\quad \beta_{\mathrm{loc}}=\beta \tag{A.35}$$

the temperature is thus intensive. Inserting Equation A.27 into Equation A.30 and Equation A.33, one can now calculate the minimal n for a given δ, α, Θ and T. Typical values for the accuracy parameters α and δ are 10 and $1/100$ respectively [189, 190]. Since $n_{\mathrm{min}}\propto\alpha$, the larger one chooses the energy range, the larger has to be the number of particles per group. Moreover, for high temperatures only, $n_{\mathrm{min}}\propto\delta^{-1}$, which means that one needs more particles per group to obtain a canonical state with greater accuracy. Finally, the minimal length scale on which intensive temperatures exist in solids is thus given by:

$$l_{\mathrm{min}}=n_{\mathrm{min}}a_0 \tag{A.36}$$

where a_0 is the lattice constant.

Since n_{min} was calculated for a one dimensional model, the results should be valid for one dimensional or at least quasi one dimensional structures of the respective materials. For yttria, a lattice constant of 1.059 nm was reported for nanotubes [191] and similar values were reported for other geometries [192–194]. Moreover, its Debye temperature is about 435 K, as will be discussed in Chapter 2. Equations A.30 and A.33 can thus be solved for such parameters.

From Figure 36, one gets for l_{min} a value of 1.5 µm, which is about 10 times larger than the average sizes for the NPs used in this thesis. This value comes from the large lattice parameter, which requires a larger number of particles per group in order to reach a thermal state. On the other hand, the nanothermometry measurements performed in Chapters 5 and 6 showed that those systems were capable of reaching a thermal equilibrium for NPs as small as 110 nm in

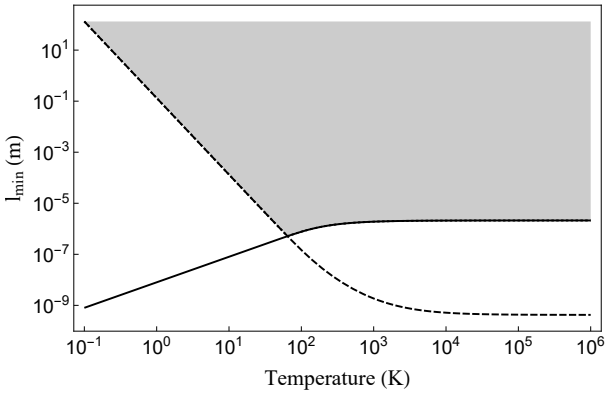

Figure 36 – Log-log-plot of l_{min} from Equation A.30 (dashed line) and from Equation A.33 (solid line) for α=10 and δ=0.01 for Y_2O_3 as a function of the temperature. Local temperature exists in the shaded area.

diameter. Therefore, the larger $l_{\min}$ result can be understood as an overestimation given by the limitations of the simple harmonic chain model.